Design, Growth, Fabrication and Characterisation of High Power Single Mode InGaAsP/InP Lasers

Mykhaylo Veniaminovych Lysevych

A thesis submitted for the degree of

Doctor of Philosophy

of

The Australian National University

December 2013

This thesis contains no material which has been accepted for the award of any other degree or diploma in any university. To the best of the author's knowledge and belief, it contains no material previously published or written by another person, except where due reference is made in the text.

……………………..

Mykhaylo Veniaminovych Lysevych

December, 2013

Acknowledgements

I would like to express my gratitude to those people, who have helped and supported me during my work on this project.

First, I would like to thank Prof. Chennupati Jagadish for his guidance, support and encouragement, and for always finding a spare minute to discuss my problems even if he was incredibly busy.

I would also like to thank Prof. Hoe Tan for his help with various techniques and equipment, very useful discussions and for reading through a few drafts of this thesis. His knowledge of the MOCVD growth was immensely beneficial for the successful completion of this work.

I am very grateful to Dr. Fouad Karouta, from whom I have learned a great about semiconductor fabrication, for his always helpful advices and encouragement.

My gratitude to Dr. Fu Lan for introducing me to device processing.

Many thanks Mr. Michael Aggett for the equipment maintenance.

Also I would like to thank everyone in the department of the EME for making my time at the department much more interesting.

I would like to acknowledge the Australian National University for financial support (in the form of the PhD Scholarship).

Abstract

The concept of optical signal amplification in telecommunication networks has resulted in considerable reduction of the bandwidth cost, due to significantly increased distance between the regenerators or in some cases complete elimination from the links. However further cost reduction requires more efficient, reliable and powerful components. For instance the increase of the optical link length or number of channels in the link requires increased pump laser power used for signal amplification. Hence there is a great demand from the telecommunication industry for the development of high power single spatial mode lasers. Single mode InP-based lasers are required for pumping of erbium-doped fiber amplifiers (EDFA), erbium-doped fluoride fiber amplifiers (EDFFA), and Raman amplifiers, while the same structure with antireflection coatings can be used as semiconductor optical amplifiers (SOA).

The two main mechanisms limiting the output power in InP-based lasers are gain saturation and two-photon absorption. In this work the avenues to overcome those limitations and increase the output power of single mode InP-based lasers are studied.

Broad-waveguide lasers have attracted a lot of attention lately. Increased waveguide thickness results in reduced interaction of the optical field with the highly absorbing heavily doped cladding regions and reduced active region optical confinement factor, thereby allowing longer devices capable of producing high output power to be fabricated. Broad-waveguide structures with optimised p-doping studied in this work have very low internal optical losses of 2.3 cm^{-1}. However, as shown in this work efficient carrier injection (hole injection in particular) through thick undoped waveguide region is a major issue.

The method proposed in this work of improving hole injection in broad-waveguide lasers by placing the active region close to the p-doped cladding show less roll-over and as a result the improvement of laser output power of more than 25% is obtained. The effects of reduced active region optical confinement factor and improved hole injection on laser performance are decoupled in the study, clearly indicating that the improvement is due to improved hole injection.

Merged beam laser (MBL) is a more complex method of increasing the output power of a single mode laser proposed in this work. Splitting the optical field into two with Y-coupler reduces gain saturation hence increasing the net gain of the mode, while maintaining single spatial mode. MBL was successfully fabricated and compared with the standard ridge waveguide laser and it shows 30% higher output power for the same injection current. The MBL shows virtually no roll-over and at 3000 mA (limited by current source) produced 229 mW of power. Additionally due to its distinctive design its spectral characteristic is strongly dominated by a single mode.

The study of the methods of increasing the laser output powers proposed in this work suggests that they can be successfully implemented in InP-based laser.

TABLE OF CONTENTS

Chapter 1

Introduction

1.1 Introduction

In this chapter the motivation for the development of high power single spatial mode InP-based lasers will be discussed and an overview of the different available approaches of achieving this goal will be provided. The justification for broad-waveguide laser design will be presented and its advantages and disadvantages will be discussed. The merged beam laser (MBL) concept will be presented together with the background of its development. Finally, the structure of the thesis is explained by a brief description of each chapter.

1.2 Motivation

As the cost of communication network bandwidth decreases, more consumers use more bandwidth. This creates a positive feedback loop, which creates the requirement for more network growth. InP-based edge emitting lasers have seen tremendous development lately, driven by the growth of optical communication networks. The main applications such as pumping of erbium-doped fiber amplifiers (EDFA), erbium-doped fluoride fiber amplifiers (EDFFA), Raman amplifiers and semiconductor optical amplifiers (SOA), require high power single spatial mode operation [1].

Usually single spatial mode operation is obtained by the formation of narrow (3 – 4 μm) ridge waveguide able to support only one mode. This allows good coupling to a single mode fiber, despite strong divergence in the transverse direction. Even though they are relatively simple to fabricate, the narrow ridge waveguide lasers are limited in terms of power output to less than 500 mW [2].

The output power of the laser can be increased by increasing the ridge width. Hence high power output has been obtained by widening the ridge waveguide of a laser up to 200 μm. This approach relies only on laser diode fabrication processes identical to the one of narrow ridge waveguide laser. Even though these lasers are capable of very high ~ 20 W [3] output power, the use of wide ridge waveguide results in multimode operation of the device, making coupling to single mode fiber very inefficient.

Hence to obtain high output power and yet maintain single spatial mode, the development of new types of laser diode design and a thorough study of the physical effects limiting the laser output power are required. Output power in single mode laser is limited by gain-saturation, thermionic current leakage, two-photon absorption, and in case of GaAs-based lasers, catastrophic optical degradation (COD).

Tapered laser merges the advantages of both narrow and wide ridge waveguide lasers. It consists of a wide "gain" section, which gradually tapers down into the narrow "mode selection" section. In the gain section the optical field spreads and thereby reduces gain saturation by lowering the field intensity, while in the mode selection section higher order modes encounter excessive losses resulting in their suppression. These lasers are capable of producing high output power ~ 11.4 W [4], however they suffer from beam instabilities (beam filamentation). In addition their fabrication process is much more complicated. Due to the high gain in the tapered section, higher order modes can withstand the losses they encounter in the narrow ridge section. To overcome this problem and increase high order mode losses the area around the mode selection section is implanted or trenches are formed by etching. Another disadvantage of tapered lasers is the need for very complicated optics required for coupling to single mode fibers.

More unusual methods of obtaining high power laser beam with single lobe are evanescently coupled arrays [5] and leaky-wave coupled arrays [6]. However the evanescently coupled arrays provide only partial coupling, resulting in significant distribution of power outside of the main peak and as a result low coupling efficiency with single mode fiber. On the other hand, leaky-wave coupled arrays are extremely sensitive to intra-element optical distance, resulting in unstable single lobe output caused by device heating.

Lasers with broad-waveguide structures [7-14] have attracted a lot of attention lately. By increasing the thickness of the waveguide layer the interaction of the optical field with the highly doped cladding regions is reduced. Free carrier absorption in highly doped layers is one of the main contributors of optical losses in semiconductor lasers [7,8,15]. This design also increases the mode size in transverse direction, hence reduces optical power density at the facets, which is very beneficial for GaAs-based lasers which suffer from COD. This leads to the reduction of optical losses and optical confinement factor, which allows the fabrication of very long devices that improve heat removal from the active region. However, the onset of higher order mode is the limiting factor for the thickness of the waveguide layer. This type of lasers is capable of increasing output power while operating in a single mode regime. Another advantage of this type of lasers is their simple fabrication process. However, as shown in this work, thick undoped waveguide region could be an issue for efficient carrier injection.

Carrier transport can significantly influence the laser performance. Usually lasers are designed using ambipolar transport approximation, which utilises a single averaged mobility value for electrons and holes. This approximation is appropriate for designing devices with thin undoped waveguide, however it was shown in relation to modulation characteristics that ambipolar approximation should not be used for structures with thick undoped waveguides [16-18], due to very significant difference in electron and hole transport times. Despite of this report no study has been reported on the dependence of laser output power on carrier injection. Hence this work makes an effort to study this issue.

Recently developed slab-coupled optical waveguide laser (SCOWL) is the improvement of the broad-waveguide laser. It increases the waveguide layer thickness beyond the cut-off condition for single mode operation. The SCOWL design is based on Marcatili's coupled-mode analysis [19], which predicts that higher order modes in a large multimode waveguide can be coupled into the slab leaving only the fundamental mode in the waveguide. This approach allows the fabrication of even larger cavities than those of broad-waveguide lasers and yet maintains fundamental mode operation. Additionally the wider ridge than standard single mode waveguide of the SCOWL results in higher modal gain as a result of increased effective volume of the optical mode. In addition, SCOWL can be designed in such a way that the mode can be nearly circular, allowing very efficient coupling to single mode optical fibers. So far the highest power output (~ 3 W) in InP-based lasers operating in a single mode operation has been produced by the SCOWL [20]. However the main disadvantage of the SCOWL design, is the bare active region exposed during the deep etching step of the ridge waveguide which requires passivation. Furthermore, two-photon absorption occurring in the waveguide layer also limits the output power in InP-based SCOWLs [21]. Two-photon absorption is a nonlinear process of simultaneous absorption of two photons by carriers with the excitation energy equals the sum of the energies of the absorbed photons. Due to two-photon absorption generated radiation gets absorbed in the waveguide layer normally transparent for the generated photons due to larger bandgap energy.

Gain saturation is another intensity dependent process which affects all gain media and therefore limits the output power of lasers. Two-photon absorption and gain saturation are the two main mechanisms limiting the output power in InP-based lasers. Both of these processes are proportional to the photon concentration in the laser cavity. Hence the method to increase laser power output proposed in this thesis is based on reducing the photon density in the laser cavity. Merged beam laser (MBL) reduces the gain saturation in the device by splitting the optical field into two waveguides using

Y-couplers. There have been attempts previously with limited success to use Y-couplers to improve mode coupling in laser arrays [22]. Also due to its ability of dividing/merging optical mode, Y-coupling has been used to obtain tunable single frequency lasers [23]. However no attempts have been reported prior to this work of using Y-coupling to reduce gain saturation and increase laser output power.

This work focuses on studying the broad-waveguide laser concept, its advantages, disadvantages and the methods of improving its power output.

1.3 Thesis Structure

Chapter 2 describes the experimental techniques and the equipment used in this work. In chapter 3 detailed description of the laser fabrication process developed for this work will be presented. Broad-waveguide lasers will be compared with conventional thin-waveguide lasers in simulation and real devices with the results presented in chapter 4. Hole injection efficiency, the main drawback of the broad-waveguide lasers, will be dealt with in chapter 5. Designing of the merged beam laser (MBL) will be presented and the performance of fabricated devices will be compared with standard ridge waveguide lasers in chapter 6. Finally the summary of the work and the avenues to further increase the laser output power will be provided in chapter 7.

References

[1] "**Optical networks: a practical perspective**", *R. Ramaswami, K. N. Sivarajan, G. H. Sasaki, (Morgan Kaufmann Publishers, USA, 2010).*

[2] **"High power InGaAsP/InP broad-waveguide single-mode ridge-waveguide lasers",** *M. Maiorov, R. Menna, A. Komissarov, D. Garbuzov, and J. Connolly, Proceedings of the Optical Fiber Communication Conference and Exhibit 3 (2001), WC2-1 – WC2-3.*

[3] **"20 W continuous wave reliable operation of 980nm broad-area single emitter diode lasers with an aperture of 96 µm",** *P. Crump, G. Blume, K. Paschke, R. Staske, A. Pietrzak, U. Zeimer, S. Einfeldt, A. Ginolas, F. Bugge, K. Häusler, P. Ressel, H. Wenzel, and G. Erbert, Proc. of SPIE 7198, 719814-(1-9) (2009).*

[4] **"12W high-brightness single-frequency DBR tapered diode laser",** *C. Fiebig, G. Blume, C. Kaspari, D. Feise, J. Fricke, M. Matalla, W. John, H. Wenzel, K. Paschke, G. Erbert, Electronics Letters 44, 1253-1255 (2008).*

[5] "**High-power, 8 W cw, single-quantum-well laser diode array**", *D. F. Welch, B. Chan, W. Streifer, and D. R. Scifres, Electron. Lett. 24(2), 113-115 (1988).*

[6] "**Resonant leaky-wave coupling in linear arrays of antiguides**", *D. Botez, L. J. Mawst, and G. Peterson, Electron. Lett. 24, 1328-1330 (1988).*

[7] "**1.5 µm wavelength, SCH-MQW InGaAsP/InP broadened-waveguide laser diodes with low internal loss and high output power**", D. *Garbuzov, L. Xu, S. R. Forrest, R. Menna, R. Martinelli, and J. C. Connolly, Electron*. *Lett*. 32 *(1996), 1717-1719.*

[8] "**High-power high-efficiency 0.98-µm wavelength InGaAs-(In)GaAs(P)-InGaP broadened waveguide lasers grown by gas-source molecular beam epitaxy**", *M. R. Gokhale, J. C. Dries, P. V. Studenkov, S. R. Forrest, D. Z. Garbuzov, IEEE J. Quantum Electron. 33 (1997), 2266-2276.*

[9] "**Effects of broad-waveguide structure in 0.8 µm high-power InGaAsP/InGaP/AlGaAs lasers**", *T. Hayakawa, M. Wada, F. Yamanaka, H.*

Asano, T. Kuniyasu, T. Ohgoh, and T. Fukunaga, Appl. Phys. Lett. 75 (1999), 1839-1841.

[10] "**High-power (>10 W) continuous-wave operation from 100-µm-aperture 0.97-µm-emitting Al-free diode lasers"**, *A. Al-Muhanna, L. J. Mawst, D. Botez, D. Z. Garbuzov, R. U. Martinelli, and J. C. Connolly, Appl. Phys. Lett. 73 (1998), 1182-1184.*

[11] "**14.3 W quasicontinuous wave front-facet power from broad-waveguide Al-free 970 nm diode lasers"**, *A. Al-Muhanna, L. J. Mawst, D. Botez, D. Z. Garbuzov, R. U. Martinelli, and J. C. Connolly, Appl. Phys. Lett. 71 (1997), 1142-1144.*

[12] "**2.3-2.7-µm room temperature CW operation of InGaAsSb-AlGaAsSb broad waveguide SCH-QW diode lasers"**, *D. Z. Garbuzov, H. Lee, V. Khalfin, R. Martinelli, J. C. Connolly, and G. L. Belenky, IEEE Photon. Technol. Lett. 11 (1999), 794-796.*

[13] "**8 W continuous wave front-facet power from broad-waveguide Al-free 980 nm diode lasers"**, *L. J. Mawst, A. Bhattacharya, J. Lopez, D. Botez, D. Z. Garbuzov, L. DeMarco, J. C. Connolly, M. Jansen, F. Fang, and R. F. Nabiev, Appl. Phys. Lett. 69 (1996), 1532-1534.*

[14] "**High power InGaAsP/InP broad-waveguide single-mode ridge-waveguide lasers"**, *M. Maiorov, R. Menna, A. Komissarov, D. Z. Garbuzov, and J. Connolly, OFC 4 (2001), WC2 1-3.*

[15] "**Low loss, thin p-clad 980-nm InGaAs semiconductor laser diodes with an asymmetric structure design"**, *M. Buda, J. Hay, H. H. Tan, J. Wong-Leung, and C. Jagadish, IEEE J. Quantum Electron. 39 (2003), 625-633.*

[16] "**Carrier transport effects in quantum well lasers: an overview**", *R. Nagarajan, Opt. Quant. Electron*. 26 *(1994), S647-S666.*

[17] "**A time-domain model for high-speed quantum-well lasers including carrier transport effects"**, *L. V. T. Nguyen, A. J. Lowery, P. C. R. Gurney, and D. Novak, IEEE J. Sel. Top. Quant. Electron. 1 (1995), 494-504.*

[18] "**High speed quantum-well lasers and carrier transport effects**", *R. Nagarajan, M. Ishikawa, T. Fukushima, R. S. Geels, and J. E. Bowers, IEEE J. Quantum Electron. 28 (1992), 1990-2008.*

[19] "**Slab-coupled waveguides**", *E. A. J. Marcatili,* *http://www.alcatel-lucent.com/bstj/vol53-1974/articles/bstj53-4-645.pdf*

[20] "**1.5-µm InGaAsP-InP slab-coupled optical waveguide lasers**", *J. J. Plant, P. W. Juodawlkis, R. K. Huang, J. P. Donnelly, L. J. Missaggia, and K. G. Ray, Photon. Techn. Lett. 17(4), 735-737 (2005).*

[21] "**Continuous-wave two-photon absorption in a Watt-class semiconductor optical amplifier**", *P. W. Juodawlkis, J. J. Plant, J. P. Donnelly, A. Motamedi, and E. P. Ippen, Opt. Express, 16, 12387-12396 (2008).*

[22] "**Single-lobe symmetric coupled laser arrays**", *K. L. Chen, S. Wang, Electron. Lett. 21 (1985), 347-349.*

[23] "**Multifunctional photonic switching operation of 1500 nm Y-coupled cavity laser (YCCL) with 28 nm tuning capability**", *M. Schilling, W. Idler, D. Baums, G. Laube, K. Wunstel, and O. Hildebrand, Photon. Technol. Lett. 3, 1054-1057 (1991).*

Chapter 2

Experimental Techniques

2.1 Introduction

In this chapter a short description of the experimental techniques used in this work will be provided. The purpose of this chapter is to present only the basic understanding of the techniques and equipment used as is applicable to this thesis. For more detailed description references have been provided at the end of the chapter.

The techniques discussed in this chapter relate to:

- Materials growth (metalorganic chemical vapour deposition)
- Materials characterisation techniques (photoluminescence, x-ray diffractometry, secondary ion mass spectrometry, electrochemical capacitance-voltage profiling)
- Device fabrication (photolithography, wet chemical etching, reactive ion etching, plasma enhanced chemical vapour deposition, rapid thermal processing, electron beam evaporation, cleaving)
- Device testing (light-current, near field and far field measurements, spectral measurements)

2.2 Materials Growth

2.2.1 Metalorganic Chemical Vapour Deposition

Metalorganic chemical vapour deposition (MOCVD) is an epitaxial technique widely used for the growth of semiconductor materials. It was primarily developed for epitaxial growth of III-V and II-VI compound semiconductor materials.

The principle behind this technique is the pyrolysis of compound gaseous precursors, one for each atomic group, with the subsequent growth of the layer with the required material composition on a substrate. Material growth is carried out at temperatures much lower than the melting point of the material, resulting in atomically smooth surfaces and abrupt interfaces.

For III-V compound semiconductors the quality of the grown structure strongly depends on the growth temperature, V/III ratio and growth rate. The V/III ratio represents the proportion of the amount of group V precursors to the amount of group III precursors supplied into the reactor. Normally, the growth is done at the mass transport regime (600 ^{o}C – 750 ^{o}C), and excess group V precursor is provided to avoid group III metal segregation and ensure that the growth rate is controlled by the amount of the group III precursors supplied into the reactor, therefore the value of the V/III ratio is >>1.

Since MOCVD sources are toxic and pyrophoric a sophisticated monitoring system and complex disposal procedure of hazardous wastes are required. Nevertheless, the non-requirement of high vacuum system, high growth rate, scalability of the process and wide range of materials make MOCVD very attractive for the industry.

All the structures used in this work were grown at the Australian National University by MOCVD. The MOCVD reactor used in this work is an AIXTRON AIX 200/4 horizontal flow reactor with wafer rotation. Rotation of the susceptor during the growth is aimed to improve uniformity of the layers. Deposition takes place at a reduced pressure of 180 mbar. The reactor is set up with: trimethylgallium (TMGa), trimethylindium (TMIn) and trimethylaluminium (TMAl) as the group III precursors, and arsine (AsH_3) and phosphine (PH_3) as the group V precursors. AsH_3 and PH_3 are gases, but TMGa and

TMAl are liquids while TMIn is solid at room temperature. Ultra high purity hydrogen is used as a carrier gas for the metalorganic precursors. Hydrogen is purified by passing it through a palladium-silver alloy membrane. Diethylzinc (DEZn), carbon tetrachloride (CCl_4) are used as p-type and silane (SiH_4) as n-type dopant precursors. Gas flow is precisely regulated by electronic mass flow controllers. Separate lines for group III and group V precursors are used, such that they do not mix and react until they get into the reactor. To minimise the transient effects during switching on/off of the gases, two set of lines are employed. One set called "Run" lines, another "Vent" lines. The "Run" lines feed into the reactor, while the "Vent" lines bypass the reactor and connected directly to the pump. The "Run/Vent" manifolds allow rapid switching between "Run" and "Vent" lines and hence a sharp interface between layers. A schematic of the MOCVD system is shown in Figure 2.1.

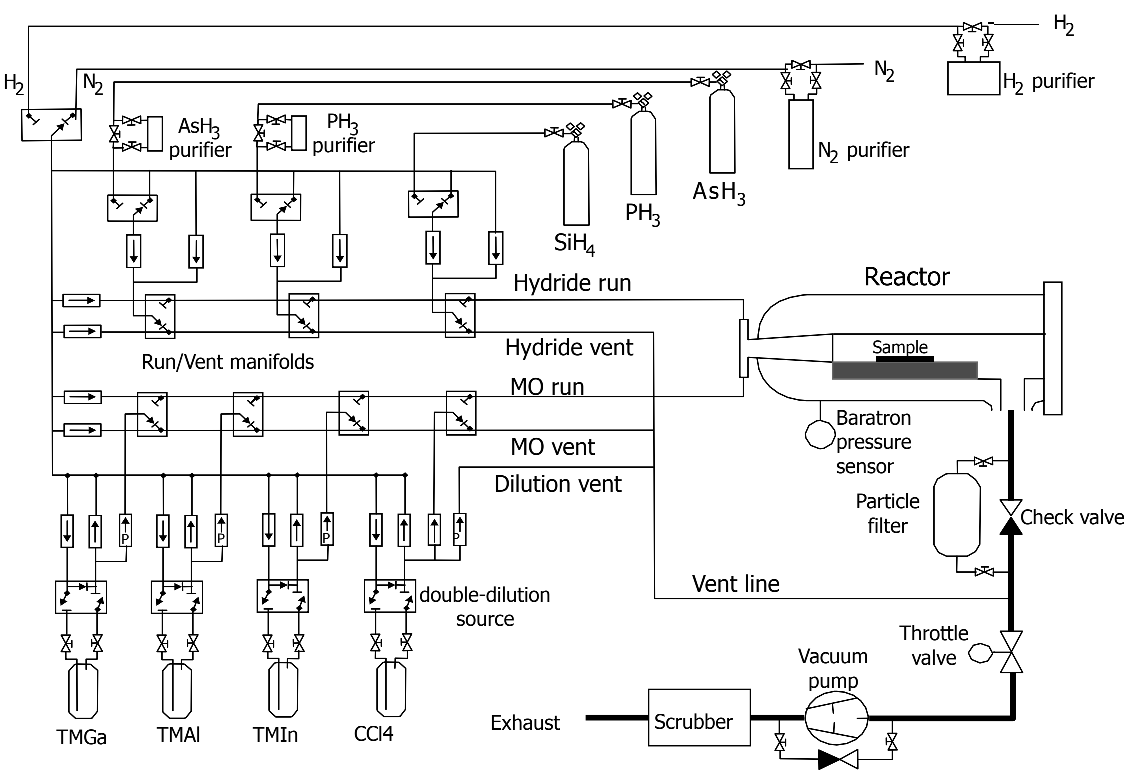

Figure 2.1 Schematic of the MOCVD (AIXTRON) system.

During growth the substrate is heated up to the growth temperature by infra-red lamps. The high temperature causes pyrolysis of the precursors, the resultant radicals are chemically very active species. They then diffuse towards the substrate, react and form a layer of the material on the substrate. This process also forms byproducts.

The general reactions, for some common III-V compounds, that take place during the growth are:

$$In(CH_3)_3+PH_3 = \mathbf{InP}+3CH_4 \tag{2.1}$$

$$xIn(CH_3)_3+(1-x)Ga(CH_3)_3+AsH_3 = \mathbf{In_xGa_{(1-x)}As}+3CH_4 \tag{2.2}$$

$$xIn(CH_3)_3+(1-x)Ga(CH_3)_3+yAsH_3+(1-y)PH_3 = \mathbf{In_xGa_{(1-x)}As_yP_{(1-y)}}+3CH_4 \tag{2.3}$$

$$xAl(CH_3)_3+yIn(CH_3)_3+(1-x-y)Ga(CH_3)_3+AsH_3 = \mathbf{Al_xIn_yGa_{(1-x-y)}As}+3CH_4 \tag{2.4}$$

The byproducts and unreacted gases from the reactor and “Vent” lines pass through a toxic gas filter and a dry activated charcoal scrubber.

More information on this topic can be found elsewhere [1-4].

2.3 Materials Characterisation Techniques

2.3.1 Photoluminescence

Photoluminescence (PL) is a fundamental technique for characterisation of a semiconductor material. It is a simple non-destructive technique employed to determine the bandgap of the material, as well as its quality and dominating recombination mechanisms through spectral measurement of re-emitted radiation.

The sample is illuminated with a monochromatic light with photons of energy higher than the bandgap of the sample. Photons are being absorbed by the material leading to the creation of electron-hole pairs. The electrons and holes then rapidly thermalise into the lowest possible states of the conduction band for electrons, and valence band for holes, and recombine, generating photons with energy equal to the recombination energy. The light is collected and measured after passing through a monochromator.

Proper interpretation of the PL spectra is very important. For typical III-V semiconductors the main peak of the PL spectrum at room temperature corresponds to the bandgap energy, while any additional peaks indicate the presence of impurities. The full width at half maximum (FWHM) reflects the degree of alloy fluctuation. As for QWs the FWHM reflects the abruptness and the smoothness of the QW layer interfaces as well as the degree of alloy fluctuation. The intensity of the PL is related to the quality of the layer.

In this work the excitation was done using a frequency-doubled diode-pumped Nd:YAG laser (λ=532 nm). To reduce noise, the laser light was chopped at around 300 Hz and the photoluminescence signal was synchronised with the laser light through a lock-in amplifier. The photoluminescence was focused on the slit of a Spectra Pro 2500 0.5 m imaging triple grating monochromator, and detected by a liquid nitrogen cooled InGaAs photodiode. A schematic of the photoluminescence set-up is shown in Figure 2.2.

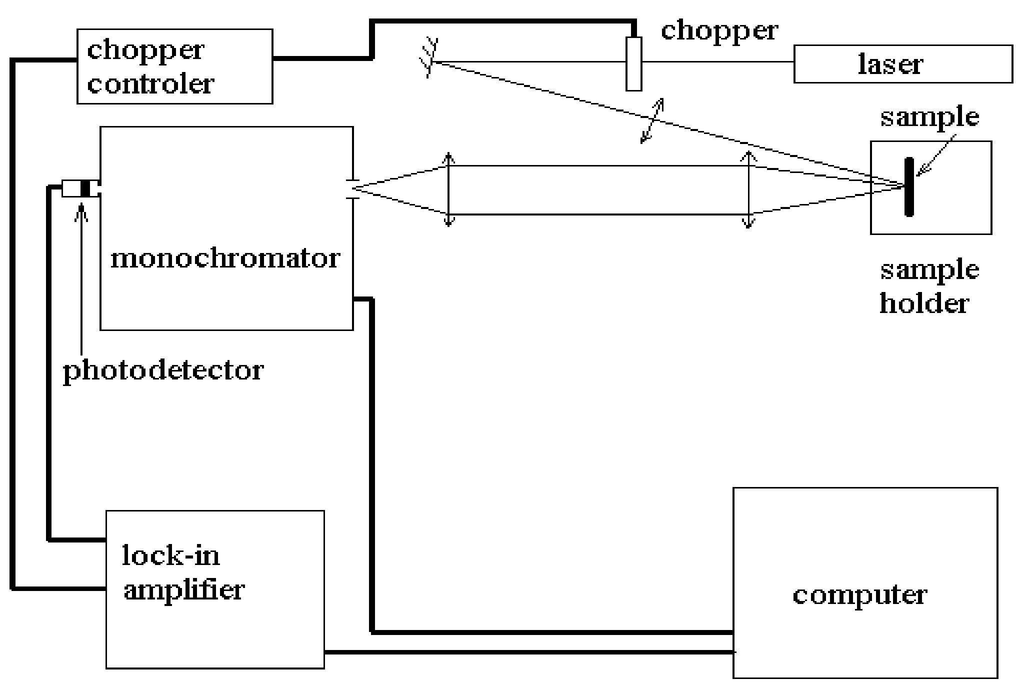

Figure 2.2 Schematic of the photoluminescence set-up.

More information on this topic can be found in ref. [5, 6].

2.3.2 X-Ray Diffractometry

X-ray diffractometry (XRD) is a very useful technique for epilayer analysis. XRD provides information about the crystal structure and chemical composition of the grown epilayer from which the quality of the epilayer can be determined.

This technique is based on Bragg diffraction. According to Bragg's Law, for electromagnetic wave with a certain wavelength, λ**,** incident on a periodic structure with period d, there is a certain angle θ at which constructive interference will occur.

$$2d\sin\theta = n\lambda, \quad n = 0,1,2... \tag{2.5}$$

Semiconductor materials are crystalline structures with related lattice constant a, hence Bragg's Law can be applied to these materials. Considering a semiconductor as a periodic structure with the period d equal to the lattice constant a and knowing the wavelength λ of the X-ray incident onto the sample, the period can be calculated by measuring the angle of diffraction θ.

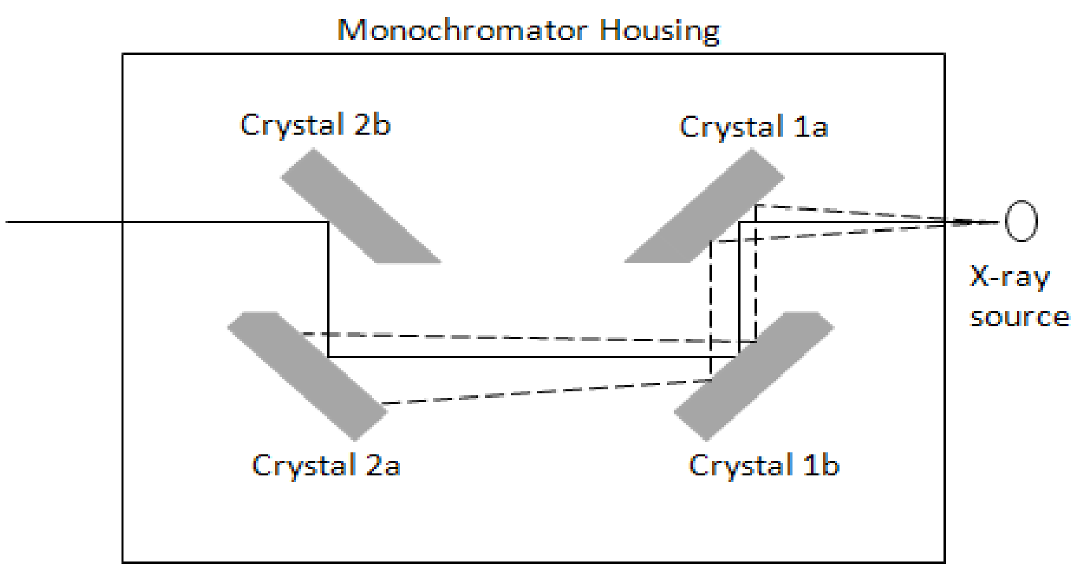

Figure 2.3 Schematic of Bartels Monochromator.

Standard X-ray source does not provide adequate resolution for structural analysis of epitaxially grown structures. Due to a very small difference in lattice constants of the substrate and epitaxially grown layer it would be impossible to separate the peaks. To collimate the X-ray beam and to narrow its spectrum a reference crystal or system of crystals like Bartels monochromator can be employed. Bartels monochromator is schematically illustrated by Figure 2.3. In general it consists of two U-shaped blocks of very high quality crystalline germanium.

For quantitative analysis, XRD system employs equation derived from Bragg Law.

$$\frac{\Delta d}{d} = -\Delta\theta \cot\theta \tag{2.6}$$

Using this formula the difference between spacing of the crystallographic planes of the substrate and epilayer (*Δd*) can be determined. But if the epilayer is under strain its lattice can be deformed, in either a compressive or a tensile manner, to match the lattice constant of the substrate in the direction parallel to the growth plane. However due to the Poisson effect the epilayer is also deformed in the growth direction. Therefore, to obtain the real or "relaxed" value of the lattice constant difference (*Δa*) between the substrate and epilayer, the strain tensor has to be included into this equation:

$$\frac{\Delta a}{a} = \frac{\in_{II}}{\in_{II} - \in_{\perp}} \frac{\Delta d}{d} \tag{2.7}$$

where $\epsilon_{\parallel}$ and $\epsilon_{\perp}$ are the strains of the lattice parallel and perpendicular to growth direction.

Figure 2.4 illustrates the measured XRD coupled scan spectrum of the broad-waveguide laser structure grown on an InP substrate in this work. The main sharp peak represents InP, and the small "shoulder" on the left from the main peak represents the thick InGaAsP waveguide layer. Absence of a gap between the main InP peak and the InGaAsP peak indicates very good lattice matching.

For measurements of the samples grown in this work an X'Pert PRO diffractometer was used with a beam of Cu Kα1 X-rays.

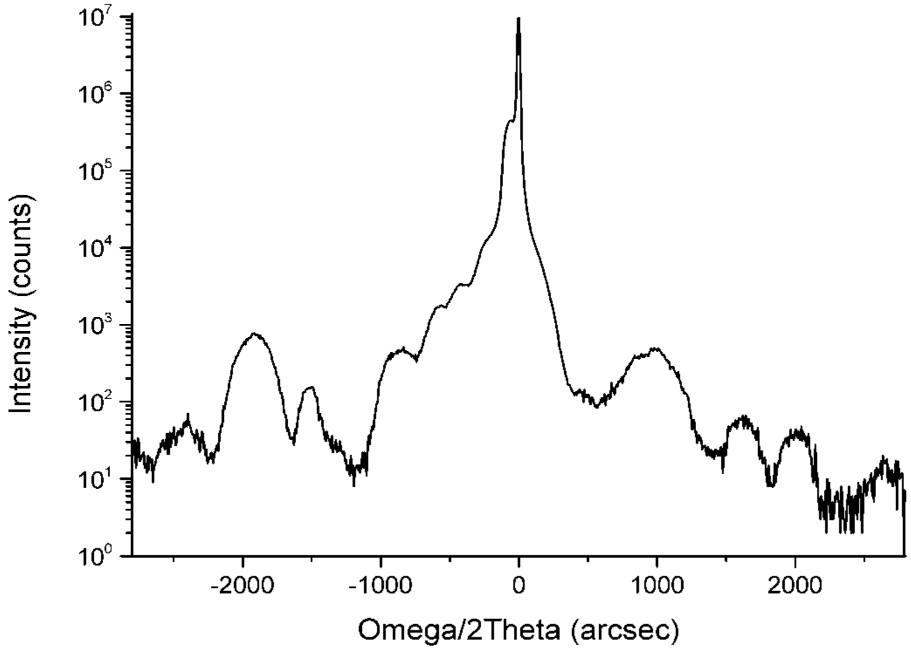

Figure 2.4 Measured XRD coupled scan spectrum of the developed broad-waveguide laser structure grown on InP in this work.

For more information about XRD refer to [7-9].

2.3.3 Secondary Ion Mass Spectrometry

Secondary Ion Mass Spectrometry (SIMS) is a widely used technique for material composition analysis.

It employs an ion beam to bombard the sample surface and sputter out the sample material in form of neutral atoms and ions. Secondary ions mass-to-charge ratio is analyzed by a mass spectrometer to perform qualitative and quantitative analyses of the present species. Figure 2.5 depicts the basic principle of Secondary Ion Mass Spectrometry.

The most commonly used primary ion sources are Ar^+, O_2^+, Cs^+ or Ga^+, these are accelerated and focused onto the sample surface. Sputtered secondary ions enter mass

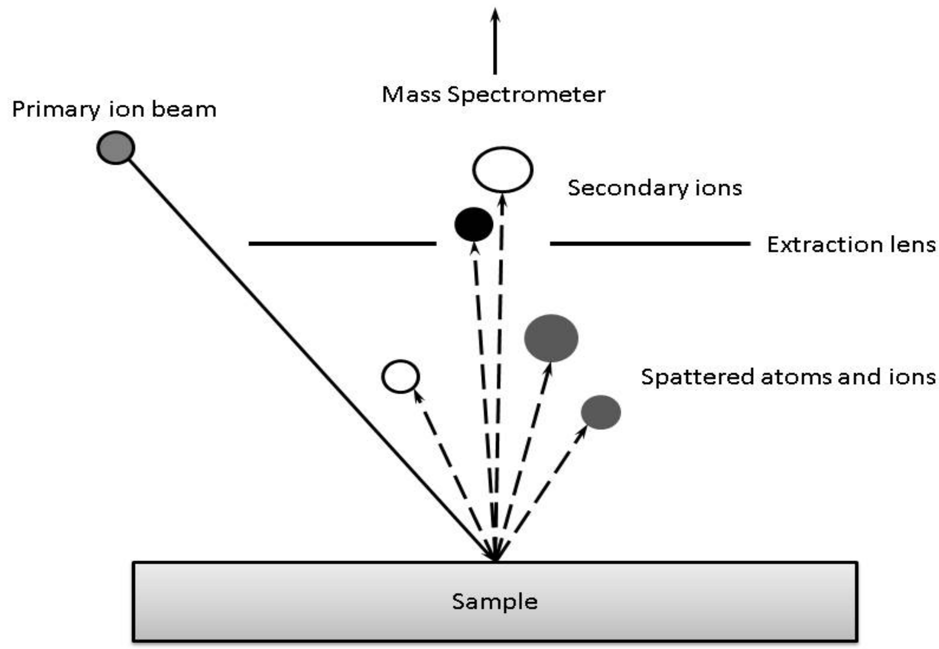

Figure 2.5 The Basic principle of Secondary Ion Mass Spectrometry.

spectrometer and in the magnetic field their trajectories are determined by:

$$r = Mv/qB \tag{2.8}$$

where M is the mass of the ion, q is the charge of the ion, v is the velocity of the ion, B is the magnetic field, r is the ion trajectory radius.

The main advantage of SIMS is its sensitivity, with a detectivity limit of $10^{16} - 10^{12}$ cm^{-3} it is perfectly suited for determining impurities and dopant profiles in semiconductor layers.

More information on this technique can be found in ref. [10, 11].

2.3.4 Electrochemical Capacitance-Voltage Profiling

The performance of all semiconductor devices depends on the purity of the material and the precise distribution of dopants throughout the structure.

Electrochemical capacitance-voltage (ECV) profiling is a form of capacitance-voltage (CV) profiling. In standard CV measurements [12] the charged impurity concentration is derived from the capacitance-voltage relationship of a reverse biased Schottky barrier. It utilizes Schottky barrier to create depletion region in semiconductor. The width of the depletion region can be controlled by varying the voltage applied to it. This dependence of depletion region width on applied voltage can provide both spatial and concentration information about electrically active impurities in the semiconductor, like doping profile.

The main disadvantage of standard CV method is the depth of the profile, which is limited by the reverse breakdown voltage of the Schottky barrier. Electrochemical capacitance-voltage profiling overcomes this limitation by successively removing a certain amount of material from the measured area of the sample prior to each measurement. As a result the sample can be profiled to any depth while the voltage can be kept constant.

ECV uses electrochemical dissolution reaction to remove the material. The etching process depends on the presence of holes, so the process is different for p-type and n-type material. For p-type materials etching takes place under forward bias. N-type materials do not have enough holes, so etching is triggered by illumination of the sample, which provides the extra holes. Therefore etching of n-type materials takes place at reverse bias with illumination.

ECV employs an electrolyte for etching the sample as well as creating a Schottky contact. After the sample has been etched to a certain depth, and a Schottky contact is formed, a reverse bias is applied to the semiconductor-electrolyte system. Because the electrolyte is fairly concentrated, there is no penetration of the field into the electrolyte, and the semiconductor-electrolyte system behaves as a Schottky junction. Therefore, according to the depletion approximation, the capacitance of the depletion layer under fixed reverse bias can be described as:

$$C = \frac{\varepsilon A}{x} \tag{2.9}$$

where x is the depletion depth, C is the capacitance, A is the effective contact area and ε is the dielectric constant.

The local doping density at certain distance, x is given by:

$$N(x) = -\frac{C^3}{\varepsilon e A^2}\left(\frac{dC}{dV}\right)^{-1} \tag{2.10}$$

where A is the effective contact of etch area, C is the capacitance, ε is the dielectric constant, $N(x)$ is the carrier concentration, e is the electron charge, V is the applied voltage and x is the depletion depth.

In this work the Accent PN4300PC Electrochemical CV Profiler was used.

More information on this technique can be found in ref. [12, 13].

2.4 Device Fabrication Techniques

2.4.1 Photolithography

Photolithography is the most cost effective and as a result the most widely used technique in wafer patterning.

In this technique, photoresist is spun onto the wafer to create a uniformly thick layer. Photoresist is a photosensitive organic compound consisting of resin, photosensitizer and solvent. After thermal treatment to remove solvent the wafer is aligned in the required direction and exposed to UV light to transfer desired pattern from a photomask to the photoresist layer. UV light causes chemical reaction in photoresist film. After exposure and depending on the type of photoresist (positive or negative) exposed parts of the film become soluble or insoluble in a specific photoresist developer, resulting in the required pattern formation. After the development, depending on the following steps (for instance etching), the photoresist pattern can be heat treated to harden it by promoting cross-linking of the polymer.

AZ 5214 E image reversal photoresist in positive photoresist mode and AZ 726 MIF developer were used for photolithography in this work. A Karl Suss MA6/BA6 mask aligner was used in this work to align the samples to the mask.

For more information about photolithography refer to [14].

2.4.2 Wet Chemical Etching

Fabrication of photonic devices requires complex lateral patterning of the structure. Therefore, etching is one of the critical steps in photonic device fabrication process. Wet chemical etching is the least complex etching technique.

During wet chemical etching the sample is immersed into etching solution for a certain time. For a certain combination of sample material and etchant, the etch rate depends on temperature. Hence, etching is usually done in a temperature controlled environment. In some cases the etchant has to be constantly agitated to achieve good quality etching.

It is very important to select an appropriate etchant, which would result in fast, controllable and reproducible etching with the resulting surface satisfying the required roughness condition.

The main advantages of wet chemical etching are very fast etching rate, simple and scalable process. Additionally, the material below the surface is not affected by the etching process. Hence, wet etching is often used to remove surface damage created by other fabrication processes. Unfortunately wet etching is mostly isotropic, which limits the resolution of wet etching.

More information about wet chemical etching could be found elsewhere [15-17].

2.4.3 Dry Etching

Dry etching is an indispensible tool for high aspect ratio etching in photonic device fabrication which cannot be accomplished by wet etching due to it isotropic nature. Good depth control uniformity, selectivity, directionality and high anisotropy are the main advantages of dry etching.

Dry or plasma etching is a process of material removal from samples immersed in plasma by physical sputtering and/or chemical etching. Plasma is generated by exposing the supplied gas to an RF electric field at a reduced pressure environment. The electric field accelerates free electrons in the gas. The electrons collide with the gas molecules, and if the electric field is high enough, the electrons can reach energies sufficient to ionise the gas molecules. This process creates more free electrons, which in turn create more ionised gas, leading to avalanche ionisation and glow discharge. Some molecules undergo impact dissociation creating ions, radicals, molecules and atoms in both ground and excited states.

The process of dry etching can be described as follows:

1. Generation of reactive species: ions and radicals.
2. Drift and diffusion of the reactive species towards the sample surface.
3. Interaction of the reactive species with the sample surface (ion bombardment or radical adsorption).
4. Surface diffusion of the reactive species.
5. Chemical reaction between the reactive species and the etched material (assisted by energy transfer from ion bombardment).
6. Desorption of the volatile reaction products.
7. Removal of the etching products and unreacted species.

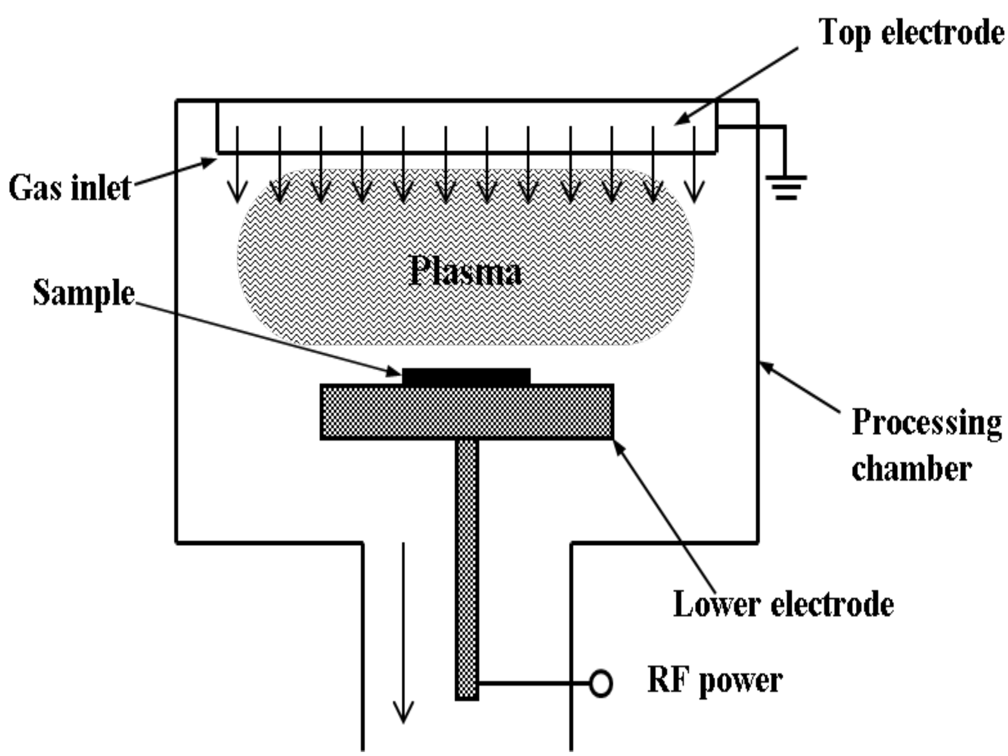

Figure 2.5 Schematic of the Oxford Plasmalab 80 Plus RIE system.

RF (radio frequency) driven parallel plate reactive ion etching (RIE) systems are the most commonly used dry etching systems owing to their lower cost, simple and robust design. Schematic of an RF driven parallel plate RIE system is shown in Fig. 2.5. The system used in this work is an Oxford Plasmalab 80 Plus RIE system. The reactor consists of two circular parallel plate-electrodes. The sample is loaded onto the lower plate, which is connected to a 13.56 MHz RF generator while the top electrode is grounded and the gas is supplied into the chamber through inlets in the top electrode. Plasma is created between the electrodes at a reduced pressure environment. Due to the electrode size difference and the presence of a coupling capacitor the system is self-biased [18]. Unreacted gases together with the etching by-products are removed from the chamber by a vacuum pump.

For more information regarding RIE refer to [18-20].

2.4.4 Plasma Enhanced Chemical Vapour Deposition

Plasma enhanced chemical vapour deposition (PECVD) is a thin film deposition technique that utilises plasma to initiate chemical reaction between the precursors. The use of plasma allows deposition at much lower temperature compared to thermal CVD techniques.

Plasma is generated by exposing the supplied gas to an RF electric field at a reduced pressure environment. The electric field accelerates free electrons in the gas. The electrons collide with the gas molecules and if the electric field is high enough, the electrons can reach energies sufficient to ionise gas molecules. This process creates more free electrons, which in turn create more ionised gas, leading to avalanche ionisation and glow discharge. Some molecules undergo impact dissociation creating ions, radicals, molecules and atoms in ground and excited states. These species are much more reactive compared to their source species, resulting in chemical reactions that are otherwise not possible between the precursor gases at low temperature. This allows deposition of various materials on temperature sensitive substrates.

The process of PECVD deposition can be described as follows:

1. Generation of reactive species: ions and radicals.
2. Drift and diffusion of the reactive species towards the sample surface.
3. Adsorption of the reactive species to the sample surface.
4. Surface migration.
5. Chemical reaction between the reactive species.
6. Film formation.
7. Removal of the unreacted species.

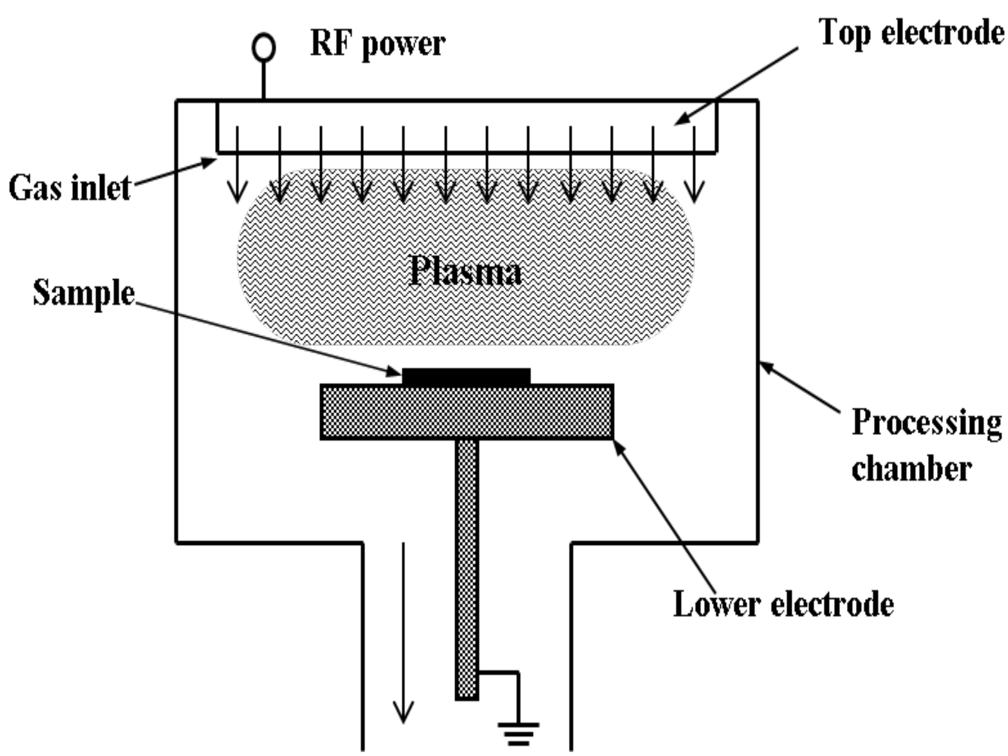

Figure 2.6 Schematic of the Oxford Plasmalab 80 Plus PECVD system.

Similar to RIE systems, RF driven parallel plate PECVD reactors gained their popularity due to low cost, simple and robust design. Figure 2.6 shows a schematic of such PECVD system. The system used in this work is an Oxford Plasmalab 80 Plus PECVD system.

Plasma is created between two parallel circular electrodes. The top electrode is connected to a 13.56 MHz RF generator, while the lower electrode is grounded. The samples are placed on the lower electrode. The reactant gases are fed in through the gas inlet in the top electrode. Due to the electrodes size difference and the presence of a coupling capacitor the system is self-biased [18]. Unreacted gases and reaction by-products are removed from the chamber by a vacuum pump.

For more information regarding PECVD refer to [18-20].

2.4.5 Rapid Thermal Processing

Rapid thermal annealing (RTA) is a sub-class of thermal processing and uses quartz-halogen lamps or hot plate to rapidly heat the sample to high temperatures in a specific ambient. Usually the sample is heated up quickly to the required temperature, kept at the temperature for a short time and cooled down at a required rate.

RTA can be used to achieve a number of sample modifications for instance: dopant activation, promotion of contact formation, impurities outdiffusion and/or passivation, dopant diffusion, material damage repair, etc. Depending on the tasks to be performed different temperature profiles and ambient gas can be used.

In this work RTA was utilized for dopant activation and contact formation. All the annealings were performed in an AET Thermal Inc. RX rapid thermal annealer under Ar atmosphere.

More information about RTA can be found in ref. [21].

2.4.6 Electron Beam Evaporation

Electron beam (e-beam) evaporation is a thin film deposition technique, which utilises a focused beam of electrons to heat and evaporate the source material. Electrons are generated by thermionic or field emission. The electrons are then accelerated and directed by a magnetic field onto the material to be evaporated. Most of the kinetic energy of the electrons is converted into thermal energy of the target material, melting and evaporating it. The evaporated material then deposits on all the surfaces of the chamber, including the samples. The deposition rate can be monitored by a quartz crystal. By changing the electron beam current the deposition rate can be adjusted. To improve the quality of the deposited layer deposition is performed in vacuum (~10^{-6} Torr). Figure 2.7 depicts a schematic of an electron beam deposition system.

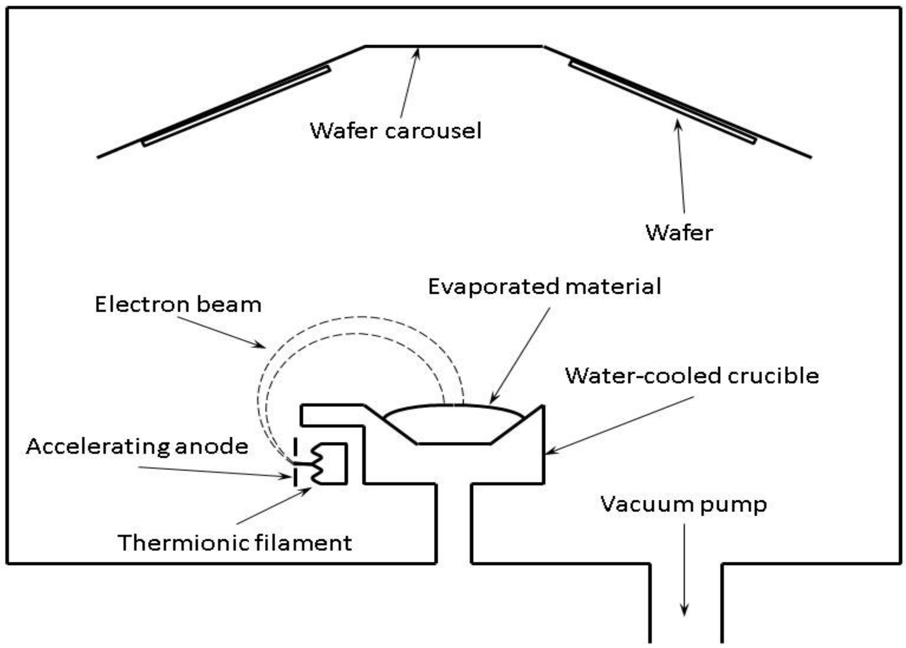

Figure 2.7 Schematic of an electron beam deposition system.

All e-beam depositions in this work were done with a Temescal's BJD-2000 deposition system.

More information about e-beam evaporation can be found in ref. [22].

2.4.7 Cleaving

Optical resonator is one of the three fundamental components of a laser. It provides optical feedback which is essential for laser generation. In general an optical resonator is a set of two mirrors with a certain reflectivity and curvature facing each other. The simplest form of optical resonator is a pair of parallel flat mirrors (Fabry-Perot resonator).

Optical resonators of edge emitting semiconductor lasers are formed by cleaved facets of the semiconductor crystal.

Wafers of compound semiconductors with zinc blende crystal structure have two preferential cleaving directions $[1,1,0]$ and $[\overline{1},1,0]$ (growth direction is [001]). During fabrication the optical axis of the laser is aligned with one of those directions, which allows the formation of cleaved facets perpendicular to the optical axis. With a proper cleaving procedure perfect atomically flat cleaved facets can be achieved.

In semiconductor laser fabrication cleaving is used in two ways:

1. Formation of the optical resonator – very critical task.
2. Separation of the devices – less critical task.

In this work the samples were cleaved using a Loomis LSD-100 Scribe Dicing Machine.

More information about crystallography and crystal cleaving can be found in [23].

2.5 Device Testing

2.5.1 Light-Current Characterisation

The quality of the laser diodes can be assessed based on a certain set of parameters. The majority of these parameters can be extracted from light-current (commonly referred to as L-I) measurement. Undoubtedly it is the most important characteristic of a semiconductor laser. The light power emitted by the laser is measured as a function of the injected current. Figure 2.9 demonstrates a typical light-current curve of a laser.

A variety of the parameters can be extracted from L-I measurements and these include:

1. *Maximum output power*.
2. *External differential quantum efficiency* – proportional to L-I slope efficiency, which is usually determined as a first derivative of the L-I curve. Figure 2.10 illustrates an example of the slope efficiency curve. This method allows not only accurate determination of the maximum value of external differential quantum efficiency, but its development with increasing injection and presence of subtle "kinks" in the L-I curve.

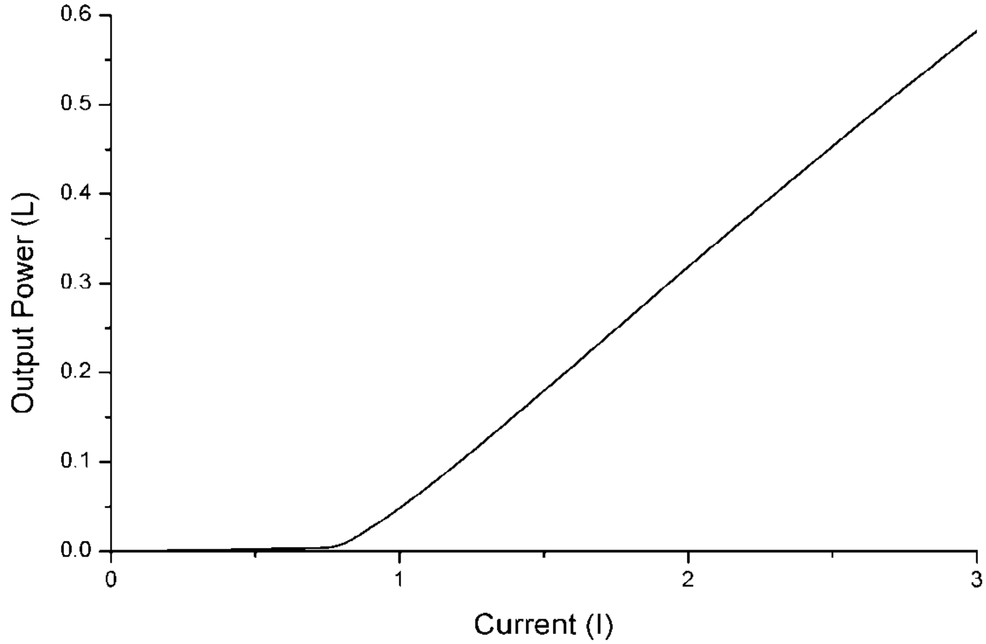

Figure 2.9 An example of a light-current curve.

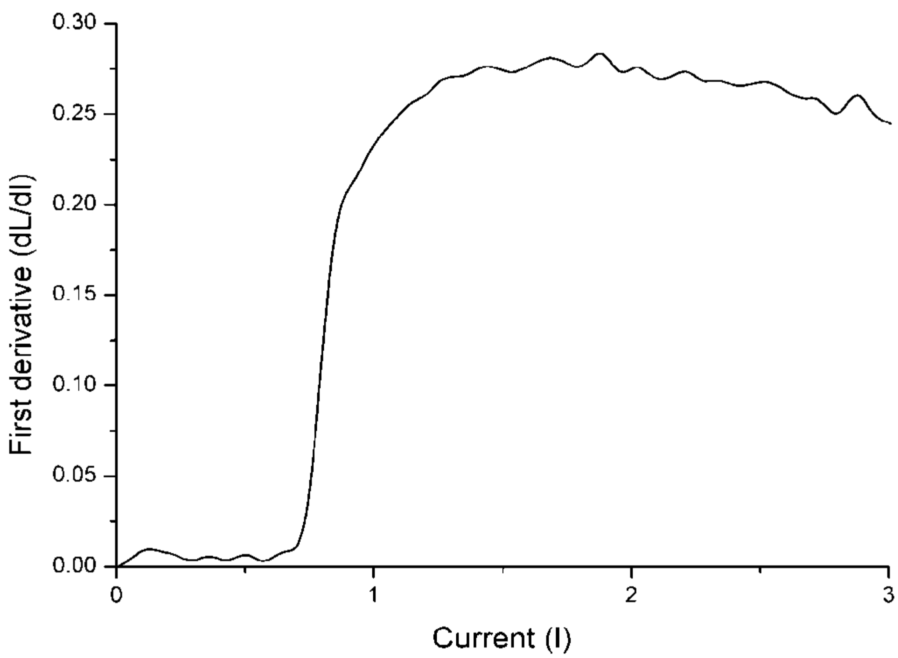

Figure 2.10 An example of first derivative (dL / dI) of the L-I curve.

The efficiency of the laser diode can be estimated by its external differential quantum efficiency. This parameter shows how well the laser diode transfers the energy of the injected current into the output light emission and is determined by:

$$\eta_d = 2\frac{dL}{dI}\left[\frac{q\lambda}{hc}\right] \tag{2.11}$$

where: η_d is the external differential quantum efficiency, q is the electron charge, h is Planck constant, c is the speed of light, and λ is the wavelength of the laser emission. It has to be mentioned that a laser diode with facets as-cleaved emits light from both facets, but the light emitted from only one facet is measured, therefore the value of (dL/dI) has to be doubled.

3. The *internal quantum efficiency* provides some information about the quality of the laser active region and the recombination mechanism. It represents the fraction of injected electron-hole pairs that recombine radiatively. The external differential quantum efficiency is related to the internal quantum efficiency through the relationship:

$$\frac{1}{\eta_d} = \frac{1}{\eta_i}\left[1 + \frac{\alpha_i}{\ln\left(\frac{1}{R}\right)} l\right] \tag{2.12}$$

where η_d is the external differential quantum efficiency, α_i is the internal loss, l is the laser cavity length, η_i is the internal quantum efficiency, and R is the reflectivity of the mirror-facet of the laser. Thus the internal quantum efficiency, as well as the internal loss can be determined by plotting the graph of the inverse external differential quantum efficiency as a function of the cavity length of the lasers. An example of such a graph is illustrated in Figure 2.11.

Although this method is fairly simple it has some drawbacks. It assumes that the total losses are constant, which is inaccurate for short cavity devices where mirror losses of a laser become significantly higher than the internal optical losses. This is represented by a significant increase in the value of inverse external differential quantum efficiency for short cavity devices (illustrated in Fig. 2.11). Hence for accurate determination of the internal quantum efficiency longer devices should be used.

The data fit is drawn through the lowest points of the data set (as shown in Fig. 2.11) to determine the internal quantum efficiency and internal loss. The lowest data points reflect the internal characteristics of laser structure, while all the data dispersion is due to fabrication imperfections. The y-intercept of the data fit represents the inverse of the internal quantum efficiency, while the internal loss is proportional to its slope.

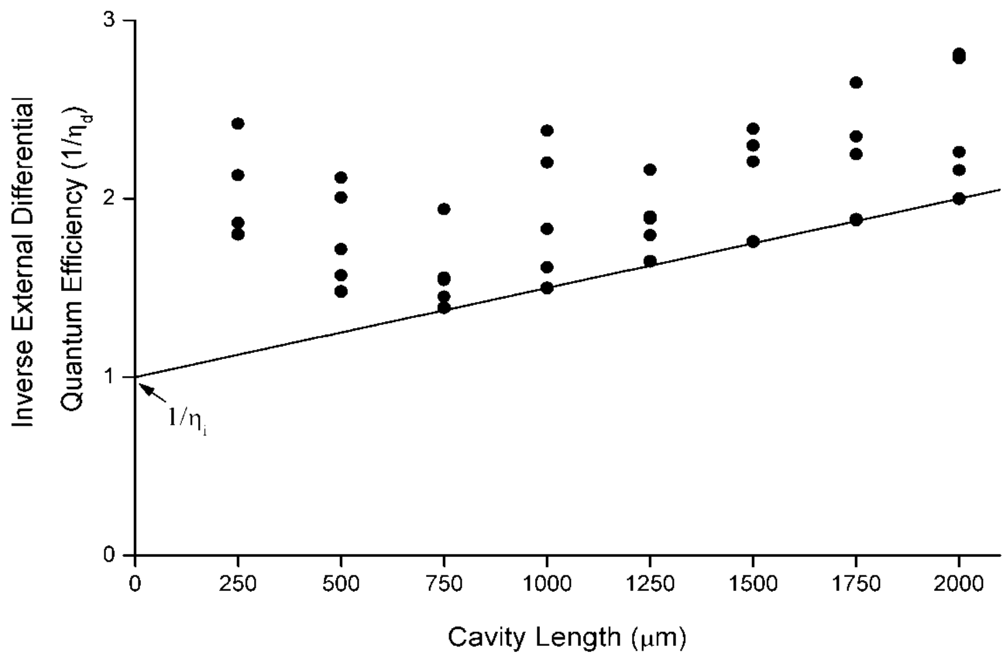

Figure 2.11 An example of the graph of the inverse external differential quantum efficiency as a function of the cavity length. The dots are the values of the inverse external differential quantum efficiency, and the line is a data fit. The y-intercept represents the inverse of the internal quantum efficiency. Internal loss is proportional to the slope of the data fit.

4. Not all the generated light contributes to the output emission and part of it is lost due to the *internal losses*. Free carrier absorption, defect absorption, impurities and the losses introduced by non-ideal fabrication process make up the internal losses.

5. *Threshold current* of a laser is the current at which lasing commences. The most widely used method to determine the threshold current is the second derivative

(d^2L/dI^2) of the L-I curve. Figure 2.12 illustrates an example of the second derivative (d^2L/dI^2) of the L-I curve.

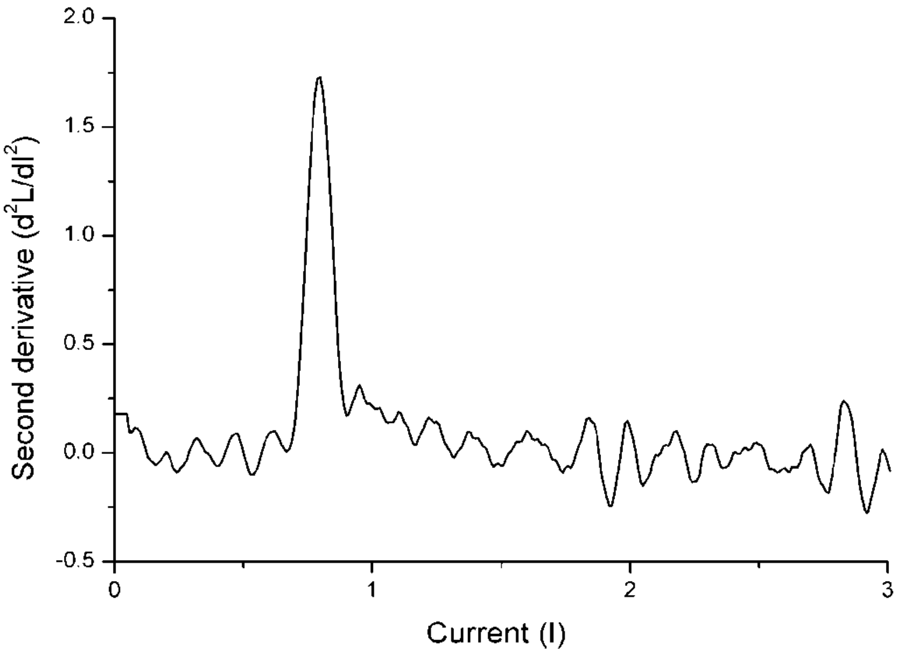

Figure 2.12 An example of second derivative (d^2L/dI^2) of the L-I curve. The main peak indicates the threshold current.

6. *Threshold current density*. Since the threshold current depends on the dimensions of the laser diode, it is more appropriate to use the threshold current density to compare devices with different dimensions. The threshold current density is determined by:

$$J_{th} = \frac{I_{th}}{Wl} \tag{2.10}$$

where J_{th} is the threshold current density, I_{th} is the threshold current, l is the length of the laser and W is the ridge width of the laser.

To obtain an L-I curve a laser is placed p-side up onto the laser holder, which is connected to a LDP-3840B precision pulsed LD current source. The laser holder is made of a copper block (cathode) with a copper clamp (anode). The temperature of the laser holder is controlled by a Peltier element placed in the copper block and operated by an ILX LDT-5910B temperature controller. Output light is collected by InGaAs power head and measured by an ILX OMM-6810B optical multimeter. Applied voltage is measured by a PicoScope-3205. For measurement visualisation and automation a LabView-based application has been created. The application provides synchronisation, controls the operation of the current source and collects measurement data.

More information about semiconductor laser characterisation can be found in [24-26].

2.5.2 Spatial Characterisation

For practical applications laser beam has to satisfy certain characteristics, like spatial mode composition, size and divergence. These are spatial characteristics of a laser and are determined by near-field and far-field measurements.

Near-field measurement is the determination of laser beam dimensions at the laser facet. Usually, the near-field measurement involves capturing the image of the beam by a detector through an optical microscope. In case of InP based lasers with the wavelength of 1.3 μm – 1.6 μm lateral resolution of the optical microscopy is not sufficient, due to diffraction limit.

In this work a confocal microscopy was employed to improve the resolution of the measurement. Confocal microscopy utilizes a pinhole aperture for optical noise filtering in Fourier space to overcome the diffraction limit. Since only one point of the image is collected at a time sample has to be scanned for a complete image.

Far-field is another very important spatial characteristic of the laser diode. It provides information about the divergence of a laser beam, since lasers do not produce collimated beams.

Usually far-field measurement is done by scanning the laser beam in lateral and transverse direction with a small-area detector. A series of those measurements can provide the information about angular divergence of the beam.

Since the energy distribution in the laser beam is not a top-hat function, consistent definition of the beam boundary is very important for practical measurements. Number of ways to define beam boundary have been proposed, but the most widely used is the point of $1/e^2$ of the maximum intensity.

Additionally spatial mode composition of the laser beam can be determined by near-field and far-field characterisations.

For more information about semiconductor laser characterisation refer to [26-28].

2.5.3 Spectral Characterisation

The optical spectrum of a conventional laser diode is the convolution of the Fabry-Perot resonator spectrum and the gain spectrum, which depends on the material bandgap.

A typical spectrum of a conventional laser diode is shown in Figure 2.14. Multiple peaks can be observed, where each peak represents a separate spectral (longitudinal) mode. The spectral position of the modes and the distance between them are determined by the optical length of the resonator. The number of modes and their height are determined by the interplay of the material gain spectrum and the losses, while their linewidth is determined by the losses or resonator quality factor.

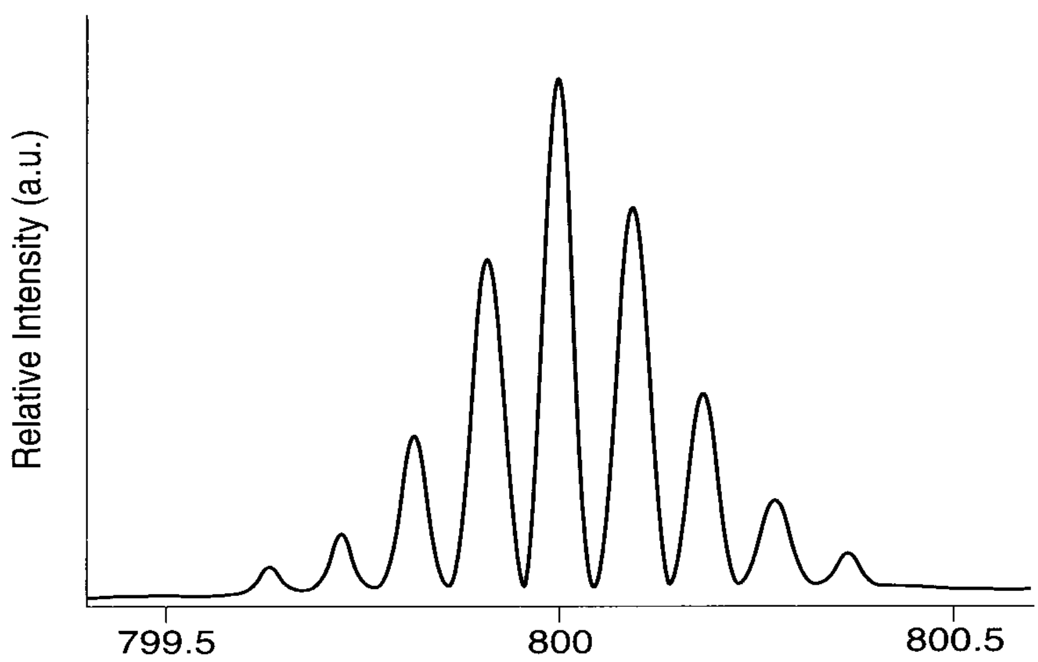

Figure 2.14 An example of the multimode spectrum of a laser diode.

Most of the conventional laser diodes generate a multimode spectrum. For a stable single mode operation a specific laser diode design has to be applied. For instance, distributed feedback (DFB), distributed Bragg reflector (DBR) and coupled cavity lasers can operate in a single spectral mode.

For spectral measurements an Agilent 86142B optical spectrum analyser was used. Light emission from the laser diode was coupled through an optical fiber into the input port of the optical spectrum analyser.

More information about laser characterisation and testing can be found in [26].

References

[1] "**Metal-organic vapor phase epitaxy**", *T.F. Kuech, Material Science Reports 2 (1987), 1-50.*

[2] "**Organometallic vapor-phase epitaxy : Theory and practice**", *G.B. Stringfellow, Academic Press, San Diego (1989).*

[3] **"Metalorganic chemical vapor deposition",** in III-V semiconductor materials and devices, *J.J. Coleman and P.D. Dapkus, R. J. Malik, editor, North Holland Publishers, Amsterdam (1989), 147-217.*

[4] **"Operation manual",** *Aixtron, www.aixtron.com.*

[5] **"Photoluminescence I : Theory",** *Chp. 4, in Semiconductors and Semimetals, Vol. 8, Transport and Optical Phenomena, H.B. Bebb and E.W. Williams. R.K. Willardson and A.C. Beer, editors, Academic Press, New York (1972), 182-320.*

[6] **"Optical processes in semiconductors",** *J.I. Pankove, Dover Publications Inc., New York (1971).*

[7] **"High resolution x-ray diffraction and topography for crystal characterization",** *B.K. Tanner, J. Cryst. Growth 99 (1990), 1315-1323.*

[8] **"X'Pert PRO X-Ray Diffraction System. User's Guide"**, *www.panalytical.com*

[9] **"Advanced X-ray scattering techniques for the characterization of semiconducting materials",** *B.K. Tanner and D.K. Bowen, J. Cryst. Growth 126 (1993), 1-18.*

[10] **"Secondary Ion Mass Spectrometry: Basic Concepts, Instrumental Aspects, Applications, and Trends",** *A. Benninghoven, F. G. Rudenauer, and H. W. Werner, Wiley, New York (1987).*

[11] **"Secondary Ion Mass Spectrometry: A Practical Handbook for Depth Profiling and Bulk Impurity Analysis"**, *Robert G. Wilson, F. A. Stevie, C. W. Magee, Wiley, New York (1989).*

[12] **"The electrical characterization of semiconductors : Majority carriers and electron states",** *P. Blood and J.W. Orton, Academic Press, London (1992).*

[13] **"PN4300PC electrochemical C-V profiler with photovoltage spectroscopy",** *Operating manual*, *Bio-Rad Micromeasurements, (1994).*

[14] **"Semiconductor lithography: Principles, practices and materials",** *W. M. Moreau, Plenum Press, New York (1988).*

[15] **"InP in HBTs by vertical and lateral wet etching",** *N. Matine, M.W. Dvorak, J.L. Pelouard, F. Pardo, and C.R. Bolognesi, Conf. Proc. Indium Phosph. (1999) 195-198.*

[16] **"AlAs Etch-Stop Layers for InGaAlAs/InP Heterostructure Devices and Circuits",** *T.P.E. Broekaert and C.G. Fonstad, IEEE Trans. Electron Devices 39 (1992), 533-536.*

[17] **"Wet chemical etching for V-grooves into InP Substrates",** *J. Wang, D.A. Thompson, and J.G. Simmons, J. Electrochem. Soc. 145 (1998), 2931-2937.*

[18] **"Handbook of plasma processing technology: Fundamentals, etching, deposition, and surface interactions",** *R. Reif, S. M. Rossnagel, J. J. Cuomo, and W. D. Westwood, Eds. Westwood, Noyes Publications (1990).*

[19] **"Glow discharge processes",** *B. Chapman, New York, John Wiley (1980).*

[20] **"Materials Science of Thin Films: Deposition and Structure"**, *M. Ohring, Academic Press, San Diego (2002).*

[21] **"Rapid thermal processing",** *R. B. Fair, Academic Press, San Diego (1993).*

[22] **"Handbook of Physical Vapor Deposition (PVD) Processing",** *D. M. Mattox, Elsevier (1995).*

[23] **"Properties of Group-IV, III-V and II-VI Semiconductors",** *S. Adachi, John Wiley (2005).*

[24] **"An Overview of Laser Diode Characteristics Test and characterisation of laser diodes: Determination of principal parameters",** *T. Hertsens, www.ilxlightwave.com*

[25] **"The Differences Between Threshold Current Calculation Methods",** *www.ilxlightwave.com*

[26] **"Test and Characterisation of Laser Diodes: Determination of Pprincipal Parameters",** *K. S. Mobarhan, www.newport.com*

[27] **"Near Field Imaging of a Laser Diode Using Scanning Method",** *J. Jeong, www.newport.com*

[28] **"How to (Maybe) Measure Laser Beam Quality",** *A. E. Siegman, in DPSS (Diode Pumped Solid State) Lasers: Applications and Issues, M. Dowley, ed., Vol. 17 of OSA Trends in Optics and Photonics (Optical Society of America, 1998), paper MQ1.*

Chapter 3

Fabrication Issues

3.1 Introduction

Due to complex nature of the laser diode fabrication process this entire chapter is dedicated to address the various issues related to laser diode fabrication. The entire processing sequence will be discussed in detail starting with epitaxial growth of the structure and finishing with sample cleaving into separate devices. This is the process developed during the course of this dissertation for the fabrication of merged beam lasers (MBL). It is not the most definitive process and the readers should develop their own fabrication process to suit their needs.

In this chapter a short fabrication flowchart will be presented first, followed by more detailed description of each step. The detailed description of the fabrication process is presented for the benefit of those who are faced with the same challenge as the author had in developing fabrication process for InP-based devices in general and lasers in particular.

3.2 Laser Diode Fabrication Flowchart

1. Epitaxial growth of the laser structure.
2. Wafer cleaving into samples.
3. Rapid thermal annealing for Zn activation.
4. Waveguide definition by optical lithography.
5. Ridge waveguide formation by RIE.
6. PECVD deposition of SiN_x passivation-insulation layer.
7. Lift-off, cleaning and native oxide removal.
8. P-contact deposition.
9. Sample thinning, cleaning and native oxide removal.
10. N-contact deposition.
11. Ohmic contacts formation by RTA.
12. Sample cleaving into separate devices.

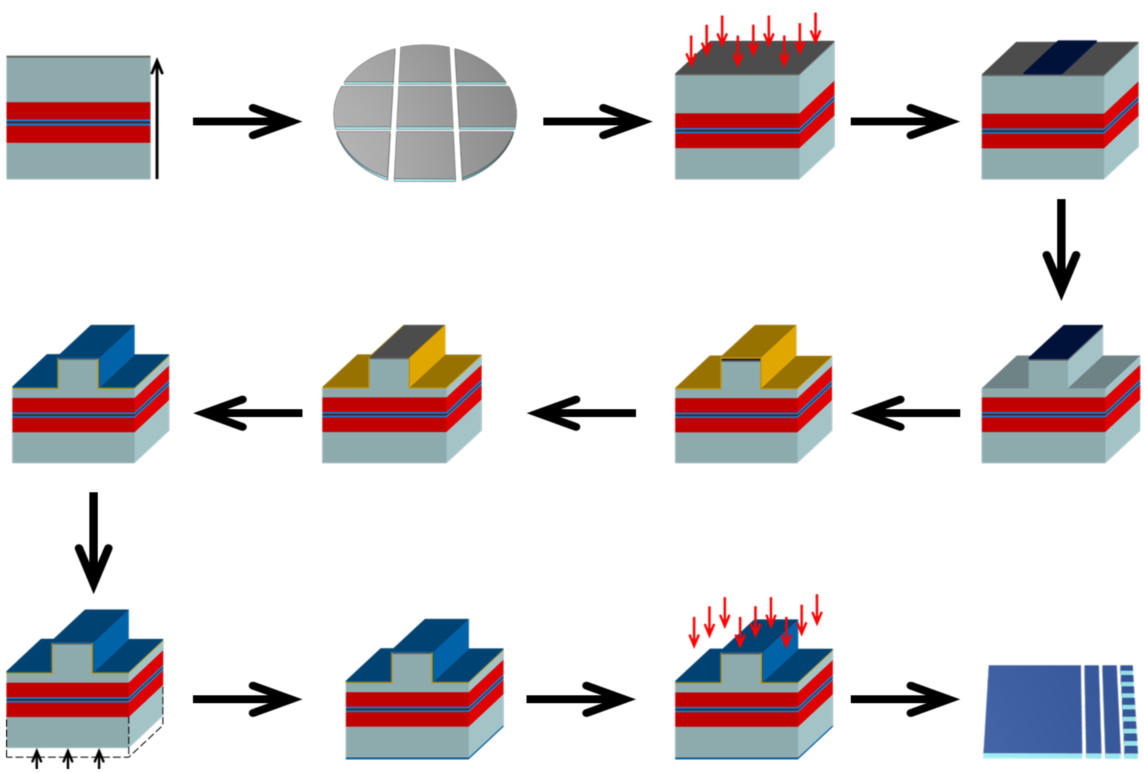

Figure 3.1 Illustration of the laser diode fabrication flowchart.

3.3 Laser Diode Fabrication

3.3.1 Epitaxial growth of the laser structure

All the samples in this work were grown in an AIXTRON AIX 200/4 horizontal flow reactor with wafer rotation. The substrates used for the growth were (100) InP substrates S-doped ($2x10^{18}$ cm^{-3}).

The substrates were baked at 700 ^{o}C under phosphine atmosphere prior to growth to remove any oxide on the surface. The reactor temperature was then reduced to 650 ^{o}C and InP buffer layer was grown. The buffer was Si-doped ($2x10^{18}$ cm^{-3}) and consisted of a 200 nm layer grown at a fast rate followed by a 100 nm layer grown at a slow rate. The slow grown buffer layer was intended to reduce surface roughness and improve the interfaces of subsequent layers. After the buffer layer growth, which also served as the n-cladding layer, an unstrained and undoped InGaAsP waveguide layer was grown. The waveguide layer contained the active region which consisted of 0.5% compressively strained InGaAs quantum wells and unstrained InGaAsP barrier layers. The following InP p-cladding was grown in two steps. First an undoped InP layer 500 nm thick was grown followed by a 1.5 μm thick Zn-doped ($2x10^{18}$ cm^{-3}) InP layer. Finally the structure was terminated by unstrained heavily Zn-doped ($1x10^{19}$ cm^{-3}) InGaAs p^{+}-contact layer. A detailed example of the structure is presented in Figure 3.2 and Table 3.1.

Highly doped (~$2x10^{18}$ cm^{-3}) p-cladding is required to reduce electron thermionic leakage into the p-cladding at high injection [1-5]. This is especially important for high power laser diodes. However, any impurities in the waveguide layer result in additional carrier and photon losses. Unfortunately excessive Zn diffusion into the waveguiding region occurs when trying to obtain highly doped p-cladding, resulting in reduced efficiency of the laser diode or even complete inoperability.

The main contributor to Zn diffusion is interstitial Zn. Even though it is preferential for Zn to incorporate substitutionally well below the solubility limit, the fraction of interstitially incorporated Zn increases rapidly when approaching this limit [6-9]. Unfortunately the solubility limit of Zn in MOCVD grown InP is about $2\text{-}4x10^{18}$ cm^{-3}

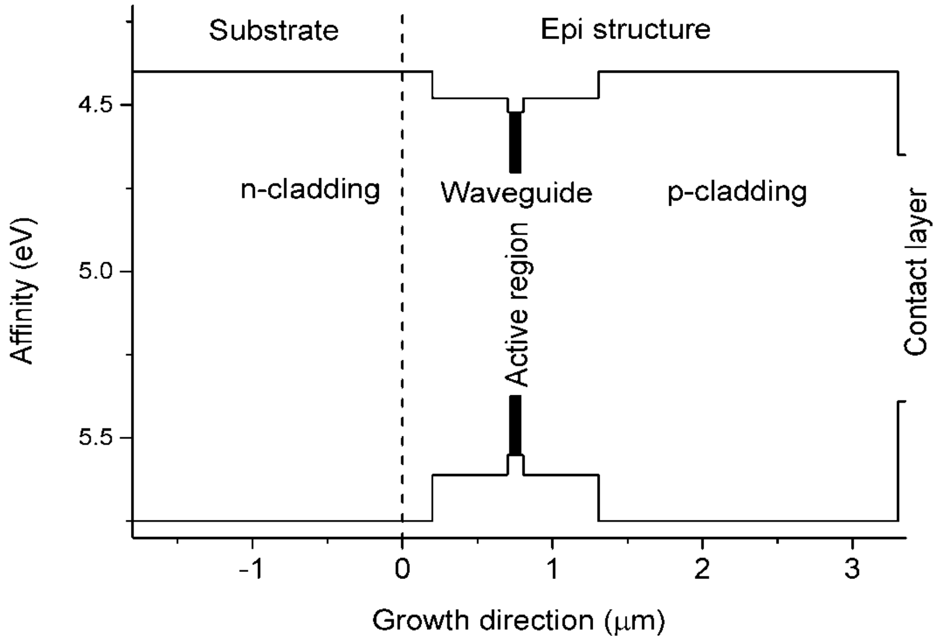

Figure 3.2 An example of the laser structure

Material	Doping (cm^{-3})	Layer thickness (μm)	Bulk bandgap (eV)	Structural function
$In_{0.53}Ga_{0.47}As$	Zn $1x10^{19}$	0.05	0.74	Contact layer
InP	Zn $2x10^{18}$	1.5	1.35	p-cladding
InP	no	0.5	1.35	
$In_{0.86}Ga_{0.14}As_{0.30}P_{0.70}$	no	0.5	1.13	Waveguide
$In_{0.79}Ga_{0.21}As_{0.45}P_{0.55}$	no	0.02	1.03	Active region
$In_{0.6}Ga_{0.4}As$	no	0.005	0.67	
$In_{0.79}Ga_{0.21}As_{0.45}P_{0.55}$	no	0.01	1.03	
$In_{0.6}Ga_{0.4}As$	no	0.005	0.67	
$In_{0.79}Ga_{0.21}As_{0.45}P_{0.55}$	no	0.01	1.03	
$In_{0.6}Ga_{0.4}As$	no	0.005	0.67	
$In_{0.79}Ga_{0.21}As_{0.45}P_{0.55}$	no	0.01	1.03	
$In_{0.6}Ga_{0.4}As$	no	0.005	0.67	
$In_{0.79}Ga_{0.21}As_{0.45}P_{0.55}$	no	0.01	1.03	
$In_{0.6}Ga_{0.4}As$	no	0.005	0.67	
$In_{0.79}Ga_{0.21}As_{0.45}P_{0.55}$	no	0.02	1.03	
$In_{0.86}Ga_{0.14}As_{0.30}P_{0.70}$	no	0.5	1.13	Waveguide
InP	Si $2x10^{18}$	0.1	1.35	n-cladding
InP	Si $2x10^{18}$	0.2	1.35	
Substrate	S $2x10^{18}$	-//-	1.35	

Table 3.1 An example of a laser structure.

[6,7] depending on growth conditions and the growth temperature in particular.

To overcome the problem of excessive Zn diffusion but avoid reducing the p-clad doping level an undoped InP “spacer” layer is introduced. The purpose of this layer is to provide a sufficiently thick layer for Zn to diffuse during the subsequent growth without reaching the waveguide region. To determine the optimal thickness of the spacing layer, which depends on a number of parameters, a number of test structures were grown and analysed by SIMS. A thickness of 500 nm of the spacing layer was determined to be the optimum for minimal Zn diffusion into the waveguide layer while keeping the p-cladding highly doped at the p-cladding/waveguide interface. Figure 3.3 illustrates Zn distribution in the structure presented in Table 3.1. Very high Zn doping is achieved in the p-cladding of $2.6x10^{18}$ cm^{-3}, where this value is close to the saturation value of Zn doping in MOCVD grown InP [6,7]. While Zn concentration slowly decreases towards the p-clad/waveguide interface, it is still relatively high ($6x10^{17}$ cm^{-3}) at the interface, but drops rapidly in the waveguide layer to $2x10^{16}$ cm^{-3} within 150 nm. This is a very good outcome since Zn solubility increases with the increase of As in the host matrix [10-12], which is well illustrated in Figure 3.5.

Figure 3.4 represents the intermediate step in the optimisation process with the spacer layer of 200 nm. An increase of Zn concentration can be observed in the InGaAsP layer at the interface with p-cladding similar to structure without a spacer layer. However the diffusion front is significantly closer to the interface.

In all of the structures a small Zn peak at waveguide/n-cladding interface can be observed. This is a result of Zn diffusion from p-cladding and preferential incorporation of Zn into material with higher As level. Gradual decrease of the peak from $5x10^{16}$ to $2x10^{16}$ cm^{-3} with the increase of spacer thickness, serves as a proof of it.

Another strong Zn peak around 3.2 μm indicates incorporation of Zn desorbed from the material deposited on the reactor chamber walls during previous growth. This is the so-called “memory effect”. In subsequent growths a 500 nm thick layer of undoped InP was grown before the next structure to reduce this “memory effect”.

Photoluminescence spectra of the structures are presented in Fig. 3.6. To avoid the PL signal from the active region being reabsorbed, before the PL measurement the highly doped contact and p-cladding layers were selectively etched. All the spectra have very

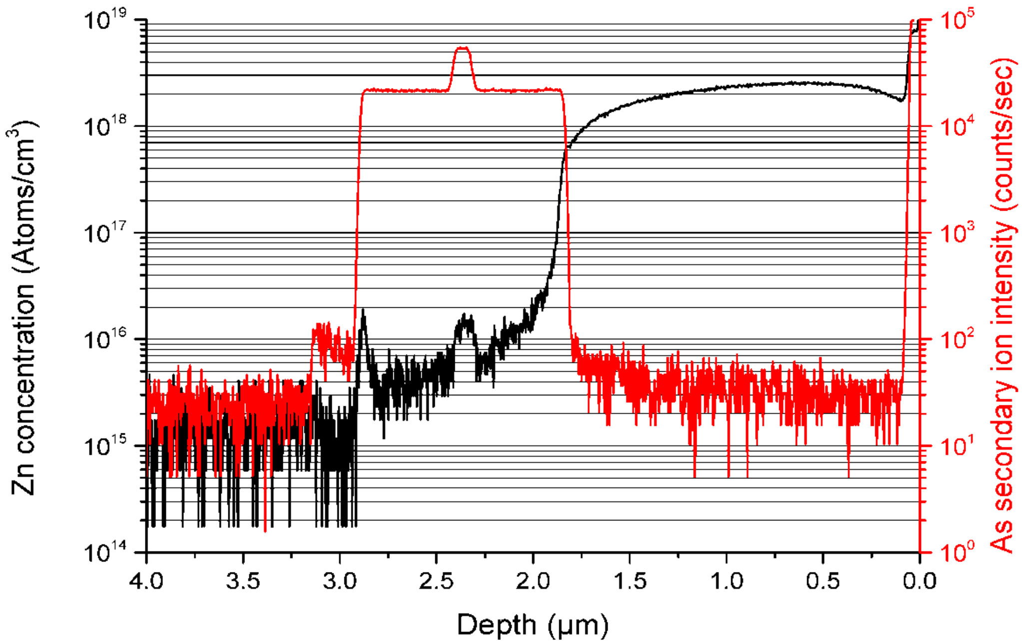

Figure 3.3 SIMS plot of Zn distribution in structure with 500 nm thick 'undoped' spacer layer (red curve represents the As signal for structure referencing).

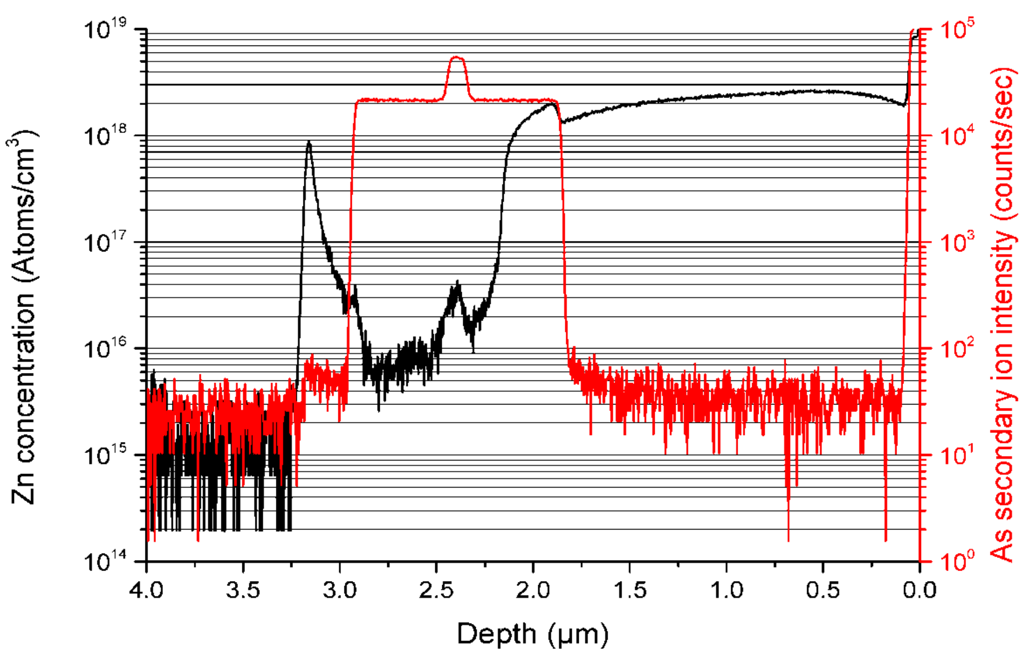

Figure 3.4 SIMS plot of Zn distribution in structure with 200 nm thick 'undoped' spacer layer (red curve represents the As signal for structure referencing).

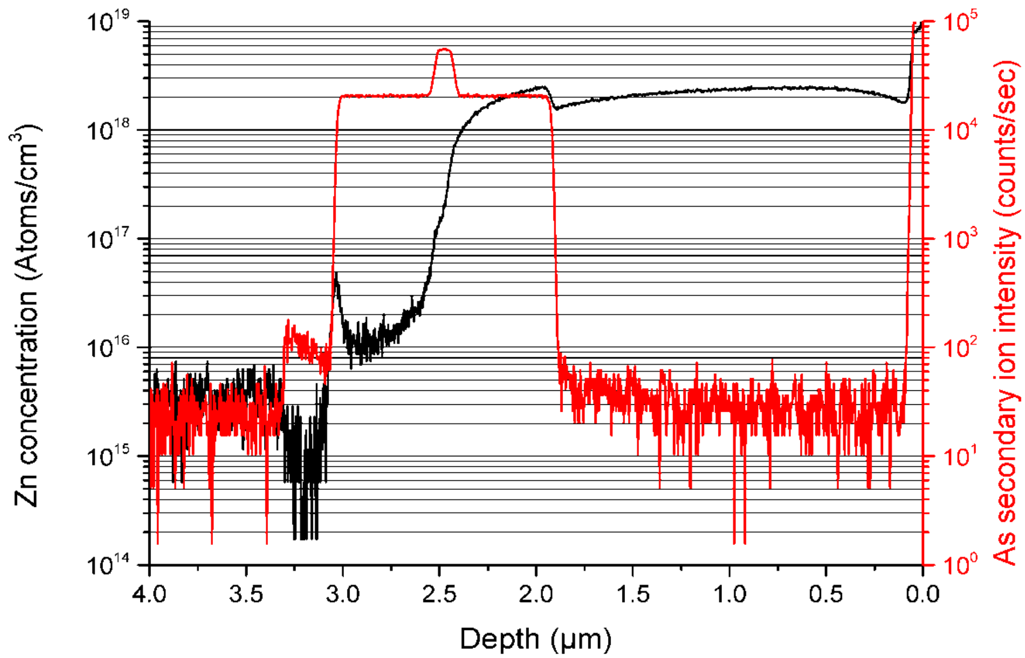

Figure 3.5 SIMS plot of Zn distribution in structure without 'undoped' spacer layer (red curve represents the As signal for structure referencing).

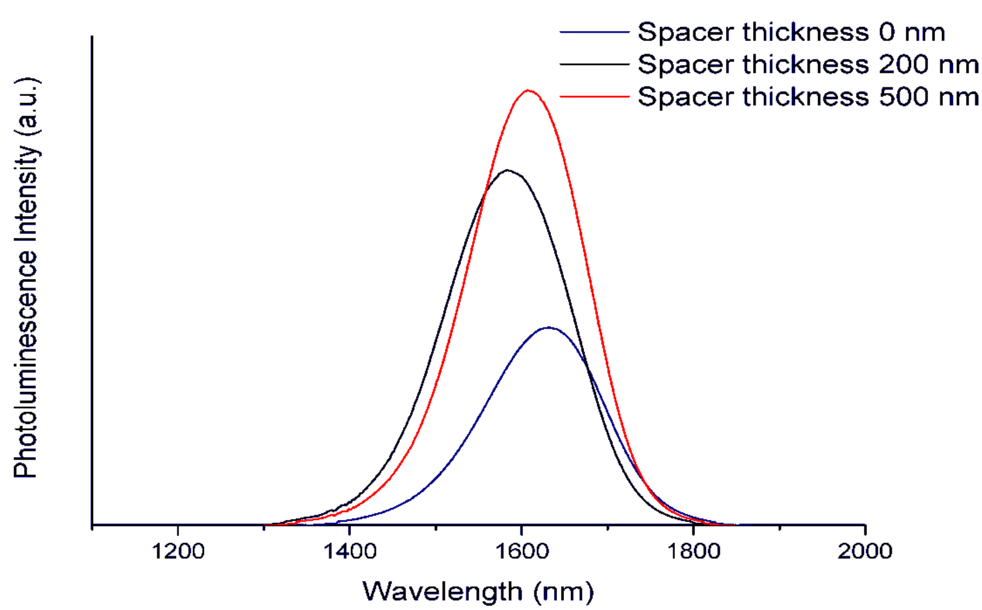

Figure 3.6 Photoluminescence of the spacer test structures. Contact layer and p-cladding layers removed.

similar value of full width at half maximum (FWHM), indicating that the structures are compatible. As expected a clear dependence between the PL signal intensity and Zn diffusion is observed. The strongest PL is produced by the sample with minimal Zn diffusion into the waveguide and minimal Zn incorporation into the active region.

3.3.2 Wafer cleaving into samples

Even though all semiconductor wafers are circular and many fabrication steps yield much better results for circular samples, like photoresist spincoating or dielectric film deposition, it would be inefficient and wasteful to use a full two inch InP wafer for each processing. Therefore, the wafers were carefully cleaved using a Loomis LSD-100 Scribe Dicing Machine into five roughly even size square samples (Fig. 3.1). At first glance it is a trivial step, but it is quite important for two reasons. Well cleaved edges provide perfect reference for mask alignment during the lithography, reducing misalignment error, which is very important for laser diode mirror-facet fabrication. Consistent sample size minimise size dependent discrepancies in some of the fabrication steps, like etching. Therefore it is strongly recommended to invest extra effort in this fabrication step and avoid manual cleaving.

3.3.3 Rapid thermal annealing for Zn activation

As mentioned above high p-doping is required for proper operation of high power laser diodes [1-5]. However not all of the incorporated Zn species are electrically active. Due to passivation of Zn the electrically measured acceptor concentration can be 2-4 times lower than the SIMS measured Zn concentration in MOCVD grown samples [12,13]. The main mechanism of Zn passivation is believed to be due to atomic hydrogen, where the pyrolysis of hydrides generates the atomic hydrogen [12,14]. This effect negates the benefits of highly doped p-cladding, resulting in enhanced leakage current in addition to increased optical losses.

Fortunately, passivated Zn can be fully recovered with simple heat treatment as suggested in references [12-14]. To quantify Zn activation in our structures and to optimise the required DEZn flow, a test structure was grown. It consisted of four 0.5 μm thick Zn-doped InP layers with various doping levels, separated by undoped 0.2 μm thick InP spacer layers. Half of the sample was kept as a reference and another half annealed for 5 min at 450 ^{o}C in Ar ambient. Subsequently the hole concentrations were measured

Material	Layer thickness (μm)	DEZn flow (mol/min)	Hole concentration (as grown) (cm^{-3})	Hole concentration (annealed 5 min @ 450 ^{o}C, in Ar) (cm^{-3})
InP	0.5	7.54×10^{-8}	undetectable	undetectable
InP	0.2			
InP	0.5	1.02×10^{-7}	1.6×10^{17}	2.2×10^{17}
InP	0.2			
InP	0.5	5.17×10^{-7}	5×10^{17}	1×10^{18}
InP	0.2			
InP	0.5	3.08×10^{-6}	5×10^{17}	3.5×10^{18}
InP	0.2			
Sub	- // -	- // -	- // -	- // -

Table 3.2 Details of Zn activation in the test structure.

using ECV profiler. The details of the test structure and hole concentrations are presented in Table 3.2.

As can be seen from the table Zn behaviour is quite complex but follows the same trend as reported in the literature. For very low DEZn flow the hole concentration is undetectable both before and after the annealing. However for low, moderate and high DEZn flows the hole concentration significantly increases after the activation procedure. The increase is 1.4 times for low DEZn flow, 2 times for moderate and 7 times for high DEZn flow. This discrepancy in fraction of as grown active Zn in the moderate and high DEZn flows was not investigated further since it was not the aim of this study. However the most plausible explanation appears to be a significantly longer exposure to the atomic hydrogen since the layer with the highest DEZn flow was grown first, which is consistent with the conclusions reported in the literature [12-14].

The most important outcome from this investigation relative to laser diode fabrication is the possibility of significant hole concentration increase by Zn activation. This results in lower DEZn flow required to achieve the desired hole concentration and as a result less Zn diffusion into the waveguide layer.

Following the heat treatment recipes in [12,13] we have selected 450 ^{o}C as the annealing temperature with an annealing time of 5 min. To avoid any unexpected effect due to sample reacting with the ambient gas we have selected a noble gas Ar as an annealing ambient.

3.3.4 Waveguide definition by optical lithography

A Karl Suss MA6/BA6 mask aligner was used for optical lithography with Cr patterned quartz mask. AZ 5214 E image reversal photoresist in positive photoresist mode was employed for waveguide definition. For consistent results the Hg lamp in the mask aligner was allowed to warm up before it was used for exposure.

1. To improve photoresist adhesion to the sample surface the sample was heat treated for 30 min at 150 ^{o}C to dehydrate the surface.

2. Immediately after the dehydration and nitrogen blow to cool the sample and remove any dust particles the sample was placed onto the spinner and photoresist applied. The sample was spun for 30 seconds at 4000 rpm, where excessive photoresist was removed resulting in a nominally 1.4 μm thick photoresist layer (no edge bead removal was performed).

3. Next the photoresist was "soft baked" in the oven for 30 min at 85 ^{o}C to remove remaining solvent, followed by a 10 min delay step for photoresist to rehydrate. This is an important step since a certain amount of water in the photoresist is required during exposure for high development rate and high contrast [15].

4. Once the photoresist had rehydrated the sample was placed into the mask aligner and the sample cleaved edge was aligned with the mask.

5. Subsequently the sample was brought up into contact with the mask and exposed using broadband UV light. After a series of tests an exposure dose of 120 mJ/cm^2 was determined to be the optimal dose for the highest contrast, minimal dark erosion and minimal indirect exposure. Another 10 min delay step is recommended at this point for outdiffusion of N_2 formed in the photoresist during exposure [15].

6. Finally the photoresist was developed using AZ 726 MIF developer. The development process was visually controlled and stopped immediately when Newton's rings are no longer observed on the sample.

7. Lastly the photoresist was "hard baked" in the oven for 15 min at 110 ^{o}C to harden it before ridge waveguide etching.

3.3.5 Ridge waveguide formation by RIE

Methane-hydrogen (CH_4/H_2) chemistry was selected for etching InP-based structures, since it results in good post etch surface quality [16-21]. This process is advantageous over Cl_2-based chemistry etching due to its non-toxic, non-corrosive properties and the ability to carry out the etching at room temperature. However excessive polymer formation [16,22] is the main drawback which could negate all these advantages. Usually polymer buildup is removed by O_2 plasma treatment [18,23-26]. In that case a typical etching process consists of alternating the etching (CH_4/H_2) with short cleaning (O_2) steps. This significantly increases the process time and prohibits the use of resists as the etching mask.

Parameters that have significant influence on CH_4/H_2 RIE etching of InP are: total flow rate of the gases, their ratio, process pressure and RF power. For optimisation study of the etching parameters, S-doped ($n = 2\times10^{18}$ cm^{-3}) InP (100) samples were used. The etched samples were evaluated using a high resolution SEM and surface roughness was measured with an optical profilometer. For the initial part of the study a SiN_x "hard mask" was used. The samples were deposited with 375 nm of SiN_x by PECVD at 300 ^{o}C. Standard photolithography was then carried out, followed by RIE etching to transfer the pattern of 3 μm wide stripes with a pitch of 300 μm onto the SiN_x layer using CHF_3/O_2 chemistry and finally the photoresist was removed in acetone.

Etching was carried out in an Oxford Instruments Plasmalab 80+ parallel plate RIE system with a 13.56 MHz RF source using a carbon plate as the sample holder. Prior to etching, the chamber was cleaned with O_2 plasma for an hour with O_2 flow of 100 sccm, RF power of 200 W and the process pressure of 100 mTorr. A sacrificial InP wafer was used to avoid any discrepancies due to loading effect, edge effect and for possibility of a simple transfer of the recipe to samples of different sizes. Before etching the sample was cleaned with O_2 plasma (O_2 flow – 100 sccm, pressure – 100 mTorr, RF power – 20 W, time – 180 seconds) to remove any photoresist and developer residue. This step is extremely important since any residue will result in micromasking and formation of unwanted features and rough etched surface [17].

During etching methane radicals (methyl) may contribute to two processes: etching of InP and polymer formation [16,22,28]. Methane radicals react with In on the sample surface to form highly volatile metalorganic compounds. At the same time hydrogen removes phosphorus from the surface of the sample by forming phosphine. However, if phosphorus removal is not sufficiently fast the surface of the sample can become indium depleted. In the absence of indium, (on the sample surface depleted of In and the mask surface) methane radicals react with each other to form polymer chains [28]. By reducing methane concentration the etch process can be made diffusion-limited so that there would be no indium depletion on the surface and hence polymer formation could be suppressed on the etched surface. However, reducing methane concentration can significantly reduce the etch rate. Thus to achieve diffusion-limited etching regime without significantly reducing the etch rate methane concentration has to be controlled carefully. There are reports in the literature [18,20,26,29] that the CH_4/H_2 ratio should be within 1/2 to 1/4. High methane concentration leads to extensive polymerisation and spontaneous micromasking [16,28,29], while low methane concentration leads to reduced etch rate [28,29].

As a starting point the standard Oxford Instrument's recipe was employed (CH_4 – 20 sccm, H_2 – 70 sccm, 35 mTorr, 150 W). Several papers [21-24,30] have reported a complete or a significant reduction of polymer formation with the addition of Ar during

$CH_4/H_2/Ar$ (sccm)	Pressure (mTorr)	RF Power (W)	Time (min)	Figure 3.7
20/70/0	35	150	30	a
20/70/10	55	150	30	b
20/70/50	55	150	30	c
20/70/90	75	150	30	d

Table 3.3 Process conditions used to determine the influence of the Ar flow on the etching and polymerization processes.

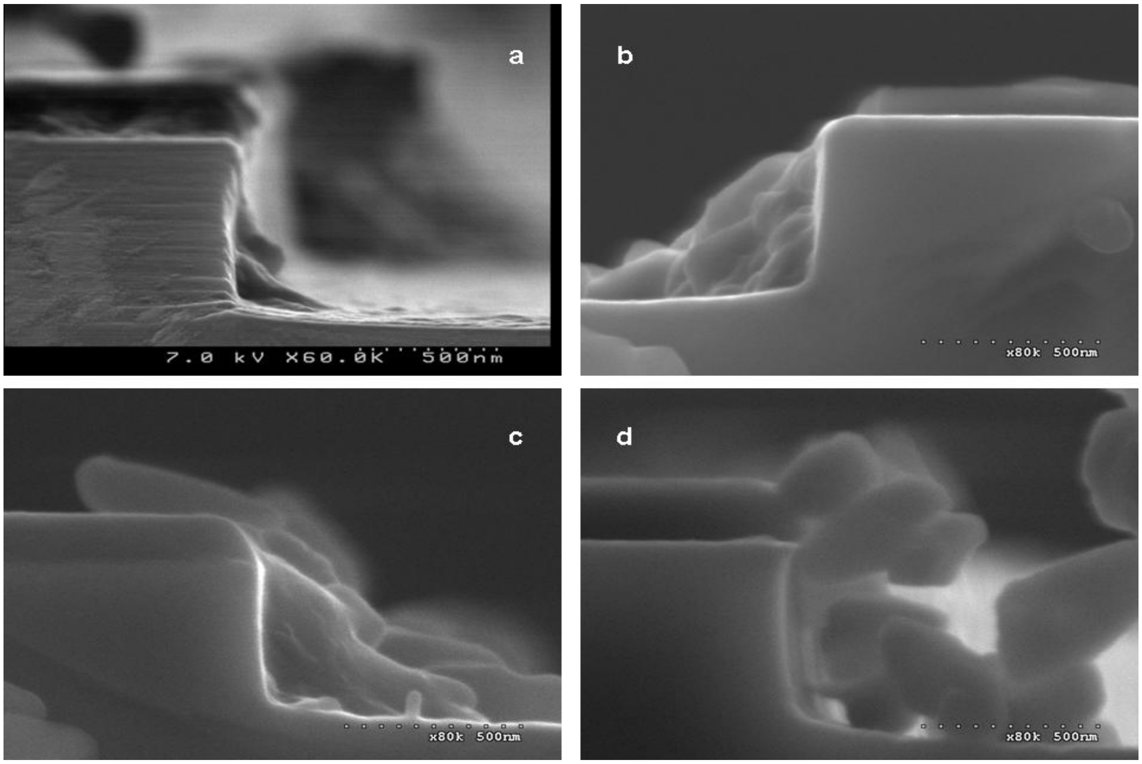

Figure 3.7 Cross-sectional SEM images of the samples etched with: a - $CH_4/H_2/Ar$ (20/70/0) at 35 mTorr; b - $CH_4/H_2/Ar$ (20/70/10) at 55 mTorr; c - $CH_4/H_2/Ar$ (20/70/50) at 55 mTorr; d - $CH_4/H_2/Ar$ (20/70/90) at 75 mTorr.

etching. Therefore, a set of four samples was etched and summarised in Table 3.3.

Initially all the samples were supposed to be etched at the same pressure of 35 mTorr. However, the small turbo pump of the system could not sustain such pressure for recipes with Ar due to increased total gas flow. Hence, the process pressure had to be increased for the recipes with Ar.

As can be seen from SEM images in Figure 3.7 (a – d), the introduction of Ar did not reduce the amount of polymer deposited on the sample. In fact the recipe without Ar (Fig. 3.7a) appears to result in the least amount of polymer formation, as well as the highest etch rate. The sample etched with $CH_4/H_2/Ar$ (20/70/90) had a significant undercut and noticeable sidewall roughness. Hence, the idea of Ar addition was disregarded in further experiments.

Another set of samples was etched to determine the influence of RF power on etching and polymerisation. As expected the etch rate increased with the increase of RF power but no correlation between RF power and polymerisation, sidewall slope or surface roughness was observed. Since 300 W is the maximum output power of the RF generator, the value of 250 W was selected for experiments in the next section.

A survey of the literature revealed a very big spread (7.5 – 90 mTorr) in the recommended process pressure [16,20,22,23,26,28,31]. Unfortunately, most of the studies were done with the focus on increasing the etch rate and not polymerisation reduction. Process pressure strongly affects polymer formation rate, since it is related to the residence time of methane in the process chamber. Therefore lowering the process pressure reduces the time methane stays in the chamber (without changing the ratio of the gases), and as a result decreases the possibility of polymerisation. In an attempt to determine the influence of process pressure on polymer formation the process pressure was reduced in steps of 10 mTorr. However, 25 mTorr was the lowest possible value for this gas flow (CH_4 - 20 sccm, H_2 - 70 sccm) that can be sustained by the turbo pump in the system. Nevertheless, it resulted in a remarkable reduction of polymerisation. In fact no polymer was observed anywhere on the sample apart from the top of the mask which can be easily removed by removing the SiN_x mask in 5% HF solution.

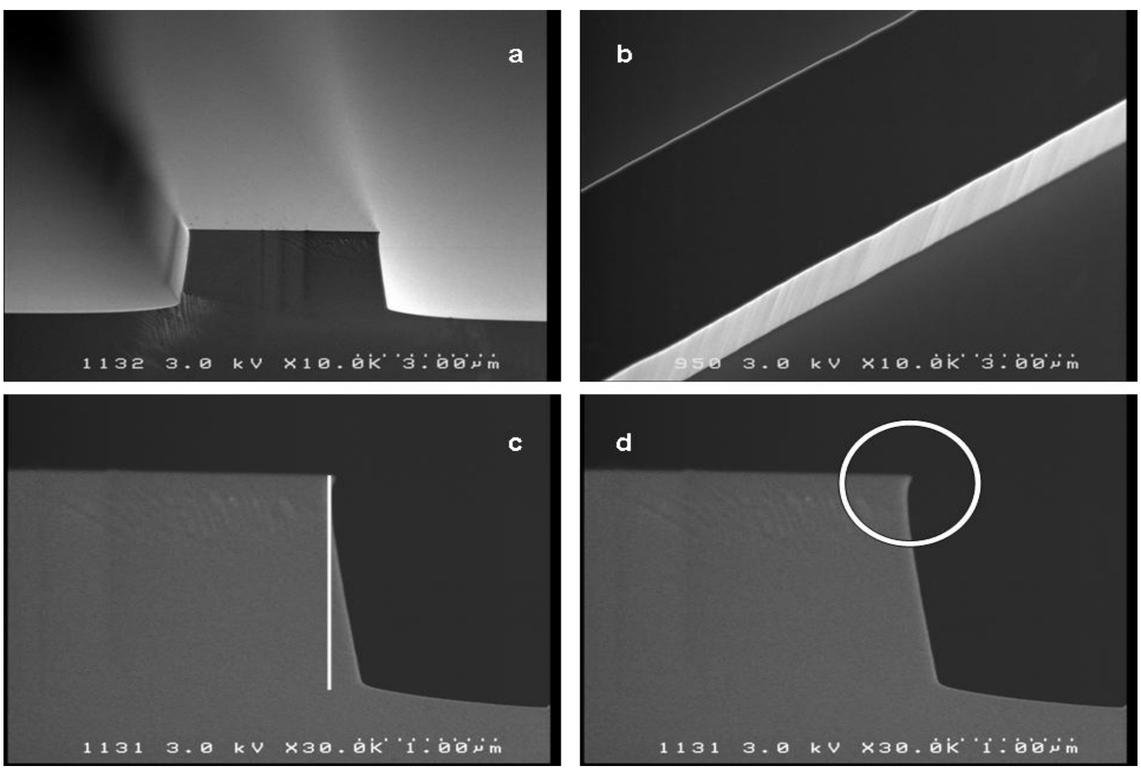

Figure 3.8 Cross-sectional views (a,c,d) and side view (b) of the waveguide ridge after the mask has been removed by 5% HF solution.

Figure 3.8a shows the cross-sectional view of the etched ridge with the mask removed. The ridge height is about 1.9 μm. The ridge sidewalls and the etched surface are flat and polymer-free, as can be seen in Figure 3.8b. The sidewalls are almost vertical with the slope ~85^{o} (Figure 3.8c), with a small undercut directly under the mask (Figure 3.8d). These are due to polymer build-up on the mask. Polymer build-up on the mask cannot be completely eliminated since on the surface of the mask methane radicals have no indium to react with and can only polymerise. However, by adding a small amount of O_2 (less than 1%) to the etching gas mixture, polymer build-up can be suppressed resulting in perfectly vertical ridge sidewalls and no undercut, as reported in [26].

The use of low pressure in this recipe eliminates the need of mid- or post-etch O_2 plasma treatment. Another added advantage is that since the polymerisation occurs on the mask, it protects the mask from erosion. As a result, a photoresist mask can be employed instead of a hard mask such as SiN_x, which would significantly reduce the number of processing steps.

To confirm the absence of polymer on the surface or the sidewalls, the sample was wet etched in $HCl:H_3PO_4$ (1:3) solution (standard solution for wet etching of InP). The cross-sectional SEM view of the sample prior to and post wet etch are shown in Fig. 3.9.

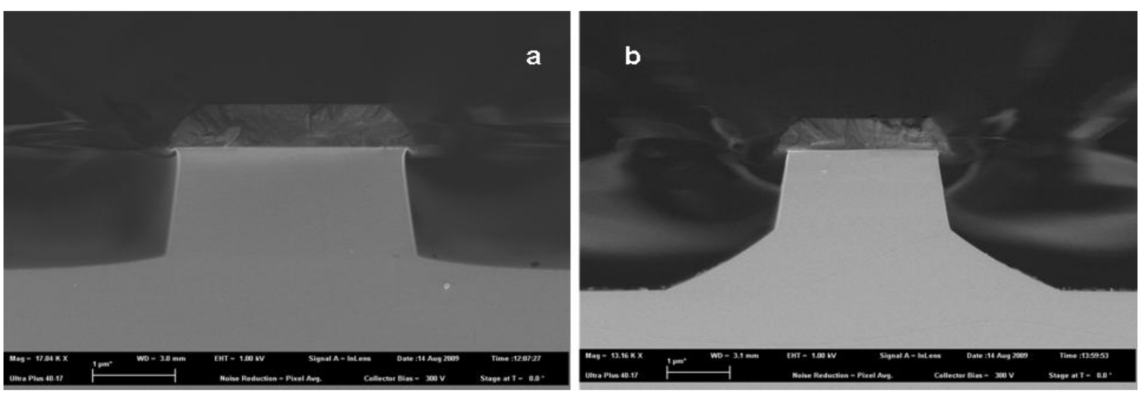

Figure 3.9. Cross-sectional SEM images of the sample prior to wet etching (a) and after a short wet etching in $HCl:H_3PO_4$ (1:3) solution (b).

Comparing the two images, the sample on the right has been etched in both vertical and horizontal directions conclusively proving the complete absence of a protective polymer after the RIE step.

To evaluate the quality of the etching recipe "shallow" etched waveguides were fabricated. An MOCVD-grown sample consisting of 0.3 μm of InP buffer layer, followed by 1 μm thick InGaAsP (λ = 1.1 μm) waveguide layer and capped with a 2 μm InP layer was used. The sample was grown on S-doped InP (100) substrate ($n = 2x10^{18}$ cm^{-3}). All layers were undoped. The sample was patterned with 3 μm SiN_x stripes and then etched to about 150 nm above the waveguide (InGaAsP) layer to create lateral confinement. The mask was then removed and surface roughness of the sample measured with an optical profilometer. The 3D image of the etched surface scanned by the profilometer is shown in Figure 3.10. The root-mean-square surface roughness was determined to be 0.66 nm,

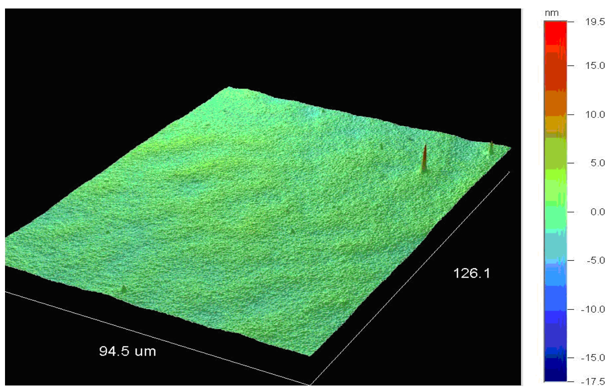

Figure 3.10. 3D topography of the etched surface, as measured by optical profilometer.

which is close to the lowest reported value in the literature achieved by RIE [21].

Waveguides with lengths varying from 3 to 10 mm were characterized for their losses using the Fabry-Perot method. Only zero order mode was observed for the field launched at the center of the waveguide. Figure 3.11 shows the measured Fabry-Perot fringes of a 3 mm long waveguide (ridge width 3 μm). High contrast between the peaks and troughs of the fringes indicates low propagation losses in the waveguide. In addition, the contrast is quite uniform across the wavelength range measured. The average propagation losses extracted from these measurements are very low, with the values of 0.28 dB/cm for the TM mode, and 0.39 dB/cm for the TE mode. These values of losses are adequate for fabricating state-of-the-art photonic devices [32]. The high quality of these waveguides confirms the excellent surface smoothness of the sample after the etching process.

Since the problem of polymer formation is eliminated on the etched surface and does not require O_2 plasma treatment, the use of a hard mask became redundant. To test the

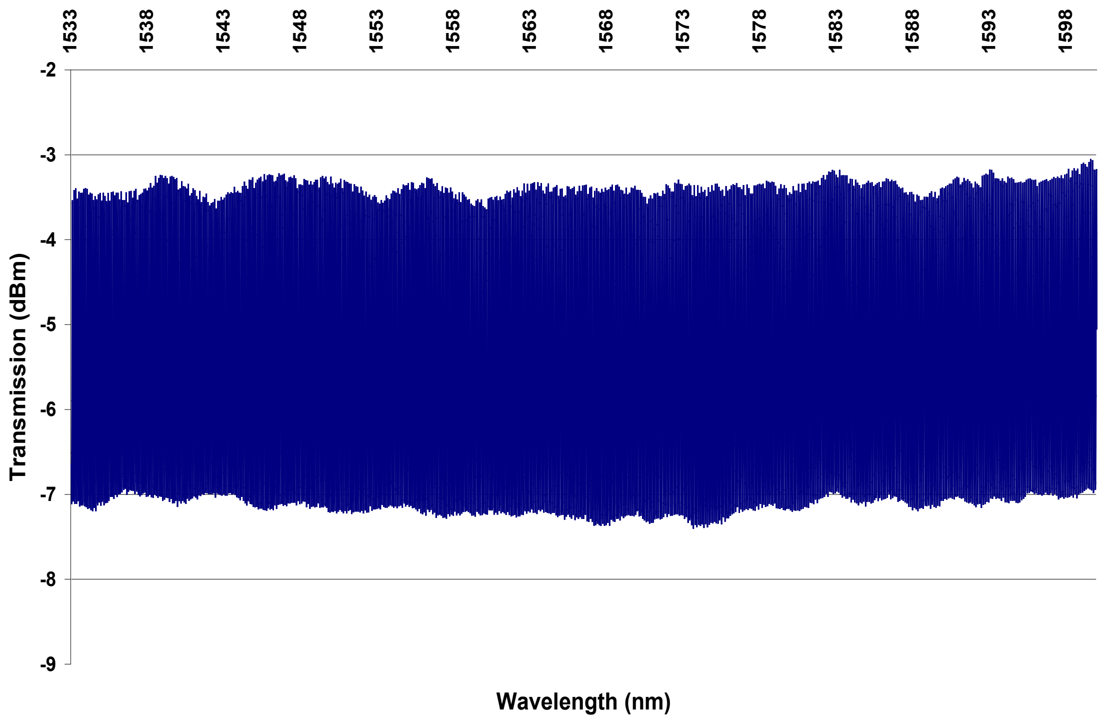

Figure 3.11 Fabry-Perot fringes of a 3 mm long, 3 μm wide waveguide.

feasibility of photoresist being employed as the mask for RIE etching, samples with only photoresist masks were etched. Since polymer is being deposited only on top of the mask, this is quite beneficial for the photoresist mask as the polymer protects the photoresist mask from erosion as a result of ion sputtering. Waveguides fabricated with the “soft” (photoresist) mask (etching depth 1.9 μm) had losses identical to those fabricated using the “hard” mask and no erosion of the mask was observed.

Therefore for the laser diode fabrication following RIE procedure was employed:

1. Before the etching the chamber was cleaned with O_2 plasma (O_2 flow – 100 sccm, RF power – 200 W, pressure – 100 mTorr, time – 1 hour).
2. The sample with the sacrificial InP wafer was placed onto the carbon electrode and cleaned with O_2 plasma (O_2 flow – 100 sccm, RF power – 20 W, pressure – 100 mTorr, time – 180 s).
3. After the sample’s cleaning etching recipe was started (CH_4 flow – 20 sccm, H_2 flow – 70 sccm, RF power – 250 W, pressure – 25 mTorr). The etching rate of InP strongly depends on chamber self-bias and at 193 V is 18.7 nm/min.

The possibility of using photoresist mask for RIE, reduces the number of the fabrication steps, therefore significantly simplifying the laser diode fabrication process.

3.3.6 PECVD deposition of SiN_x passivation-insulation layer

For electrical passivation SiN_x layer was deposited on the sample immediately after etching. The deposition was carried out in an Oxford Instruments Plasmalab 80+ parallel plate PECVD system with a 13.56 MHz RF source.

Prior to the deposition the chamber was cleaned with CF_4/O_2 (80% / 20%) at 300 ^oC (gas flow – maximum allowed by the mass flow controller, process pressure – 750 mTorr, RF power – 200 W). Next the chamber was cooled down to 100 ^oC and a "dummy" SiN_x deposition was executed to coat the chamber with a SiN_x layer.

The developed RIE process described above allows the initial photoresist mask to be used for the lift-off of SiN_x from the top of the ridge. However, the deposition temperature has to be kept at ~ 100 ^oC to avoid photoresist hardening which would prevent lift-off.

A 200 nm thick SiN_x layer was deposited on the entire sample. For SiN_x deposition the following recipe was used: temperature – 100 ^oC, NH_3 flow – 20 sccm, SiH_4/N_2 (5% / 95%) flow – 400 sccm, RF power – 20 W, process pressure – 1 Torr. The deposition rate was ~ 25 nm/min with the measured refractive index of 1.76 at 1550 nm.

3.3.7 Lift-off, cleaning and native oxide removal

For electrical contacting of the laser diode SiN_x was removed from the top of the ridge by lift-off. The sample was soaked in warm acetone for a few hours, which dissolved the photoresist. Without the support of photoresist the SiN_x from the top of the ridge can be removed by a squirt of acetone.

After the top of the ridges were open the sample was cleaned to remove any photoresist residue. The cleaning was done in the following sequence: acetone, isopropanol, ethanol, deionised water. First the sample was soaked for 15 min and then thoroughly rinsed with the same solvent before placing it in the next one. To aid cleaning the solvents were heated up. Next the sample was cleaned with O_2 plasma (O_2 flow – 100 sccm, process pressure – 100 mTorr, RF power – 150 W, time – 15 min).

Finally the sample was etched for 30 seconds in 10% solution of H_3PO_4 to remove native oxide from the InGaAs contact layer before subsequent metallisation.

3.3.8 P-contact deposition

Immediately after the native oxide removal the sample was loaded into the electron beam evaporation chamber and brought to vacuum to avoid re-formation of native oxide. For contact deposition a Temescal's BJD-2000 deposition system was used.

Once the vacuum in the chamber reached 10^{-7} Torr range, metal deposition was started. Such a high vacuum serves as an indicator that any solvent or water from the sample surface or SiN_x layer has outgassed. For p-contact based on extensive literature review [33-40] a following metal scheme was selected, Ti/Pt/Au – 50/75/1500 (nm). The thick layer of gold was intended to improve current injection by making it more uniform through reducing the layer resistance.

Before each subsequent layer the deposition was paused for vacuum to recover, but more importantly for the sample to cool down to reduce stress buildup.

3.3.9 Sample thinning, cleaning and native oxide removal

To facilitate formation of mirror-facets by cleaving and to reduce thermal resistance for n-side down mounted devices the sample had to be thinned.

The sample was mounted p-side down on a sample holder with wax. When mounting the sample it is very important to avoid air bubbles under the sample, since bubbles can break the sample when the sample becomes thinner and structurally weaker. Also the sample should not be held down when the wax hardens because the introduced strain can be excessive for the thinned sample. Excessive wax was carefully removed with a scalpel. Using progressively higher grade sandpaper (particle size 35 μm – 3 μm) the sample was hand polished to the thickness of 200 μm. Finally the sample was polished with alumina paste (0.3 μm) on wet suede to remove all the scratches. Mirror-like surface is required for cleaving step, because any scratch can serve as an unwanted guide for the propagating crack. Using this procedure the samples can be easily polished down to 100 μm but it has to be mentioned that the sample becomes very brittle and has to be handled with extreme care.

After the mirror like surface has been achieved sample was cleaned with solvents to remove any traces of wax. Similar to previous cleaning step the following cleaning sequence was used: acetone, isopropanol, ethanol, deionised water. First the sample was soaked for 15 min and then thoroughly rinsed with the same solvent before placing it in the next one. To aid cleaning the solvents were heated up.

Finally the sample was etched for 30 seconds in 10% solution of H_3PO_4 to remove native oxide, surface damage and any residual contaminants for the next metallisation step.

3.3.10 N-contact deposition

Similar to p-contact deposition, straightway after etching the sample was loaded into the electron beam evaporation chamber and brought to vacuum, to avoid native oxide re-formation.

Once the vacuum in the chamber reached 10^{-7} Torr range, metal deposition was started. For n-contact a following metal scheme was selected: Ge/Au – 50/1500 (nm) [41]. Apart from very low contact resistance this material system has another advantage of colour change from golden to yellow-brown after alloying as a result of In diffusion into the Au layer. Therefore the quality of the contact can be easily evaluated by visual inspection. Because of In – Au alloying contact peeling due to stress buildup is not an issue for this contact.

3.3.11 Ohmic contacts formation by RTA

For ohmic contact formation the sample was annealed in an AET Thermal Inc. RX rapid thermal annealer. In this system radiation generated by the IR lamps is mostly absorbed by the silicon wafer used as a sample holder and then transferred to the sample.

Hence the sample was placed p-side down onto the silicon wafer, since precise control of the annealing temperature and time is much more important for the formation of a good quality p-contact. After a broad literature review the following annealing regime was selected: temperature – 450 ^{o}C, time – 60 seconds and ambient gas – Ar. These annealing conditions were reported [33,38-41] to produce the lowest contact resistance for metal-semiconductor systems similar to both p- and n- contacts in our devices.

The gas flow was set to 5 L/min for the first 3 minutes to purge the annealing chamber and then reduced to 2 L/min. The gas flow was allowed to stabilise for 2 minutes before the temperature was ramped up to 450 ^{o}C in 5 seconds. The annealing temperature was maintained for 60 seconds. After that the IR lamps were switched off and the sample was allowed to cool down under Ar ambient.

It should be mentioned here that for samples intended for CW operation, after annealing they were loaded into a thermal evaporator and 2 μm of In was deposited on the n-side of the sample. After cleaving devices intended for CW operation were placed n-side down (with the In layer) on copper blocks which have been finely polished and heated to about 160 ^{o}C for a minute on a hotplate. This provides a relatively strong bond with good thermal, electrical and mechanical characteristics. A test attempt to remove the device from the block resulted in device disintegration rather than bonding failure.

3.3.12 Sample cleaving into separate devices

Finally the samples can be cleaved into separate devices. A Loomis LSD-100 Scribe Dicing Machine was used for cleaving.

A sample was mounted onto an adhesive film following the manufacturer's guidelines, paying special attention not to trap any air under the sample. Air bubbles would result in undesired cleaving of the sample. The sample was aligned to the scriber coordinate system using its cleaved edge. With the "notch and brake" cleaving mode the sample was cleaved perpendicular to the laser waveguides into bars of multiple devices with the desired cavity lengths. In this mode the scriber creates a one side limited scribe to form a starting point for cleaving, since full scribing would damages the waveguides. This creates the laser mirror-facets, hence it is a very critical fabrication step. Then the film was stretched to avoid bars rubbing against each other, which can damage the mirror-facets, and the bars were carefully removed.

Next, following the same procedure the bars were lined up onto the adhesive film. Each bar was aligned to the scriber coordinate system and using the “peck and brake” cleaving mode cleaved into separate devices. In this mode the scriber creates a short scribe with the maximum length of 0.7 mm. When separating devices the scribing tool should not come too close to either end of the device, to avoid chipping the mirror facets. Finally the film was stretched and the separated lasers could be carefully removed from the film.

3.4 Conclusion

InP-based laser diode fabrication process developed in this work was presented in this chapter. The process description from structure growth to device cleaving was made as comprehensive as possible with a lot of practically important details.

This process is significantly simplified compared to standard fabrication process owing to the developed single step dry etching, which allows the use of photoresist mask. Despite the fact it is less complex it is quite versatile. It can be successfully used for fabrication of lasers with complex waveguides like merged beam laser (MBL) as well as standard straight ridge waveguide lasers.

Lasers fabricated following this procedure showed very low optical losses, consistent across a number of structures.

References

[1] "**Dependance of the light-current characteristics of 1.55-µm broad-area lasers on different p-doping profiles**", *I. K. Han, S. H. Cho, P. J. S. Heim, D. H. Woo, S. H. Song, F. G. Johnson, and M. Dagenais, IEEE Photon. Technol. Lett. 12 (2000), 251-253.*

[2] "**Effect of heterobarrier leakage on the performance of high-power 1.5 µm InGaAsP multiple-quantum-well laser"**, *L. Shterengas, R. Menna, W. Trussell, D. Donetsky, G. Belenky, J. Connolly, D. Garbuzov, J. Appl. Phys. 88 (2000), 2211-2214.*

[3] **"Effect of p-doping profile on performance of strained multi-quantum-well InGaAsP-InP lasers",** *G. L. Belenky, C. L. Reynolds, R. F. Kazarinov, V. Swaminathan, S. L. Luryi, and J. Lopata, IEEE J. Quantum Electron. 32 (1996), 1450-1455 .*

[4] **"Direct measurement of the carrier leakage out of the active region in InGaAsP/InP laser heterostructures",** *G. L. Belenky, R. F. Kazarinov, J. Lopata, S. L. Luryi, T. Tanbun-Elk, and P. A. Garbinski, IEEE Trans. Electron Devices 42 (1995), 215-218.*

[5] **"Effect of p-doping profile on performance of strained InGaAs/InGaAsP multiple quantum well buried heterostructures laser diodes with Fe- or p/n/p-doped InP current blocking layer",** *H. S. Kim, D. K. Oh, I. H. Choi, Mat. Sci. Eng. B 77 (2000), 202-206.*

[6] **"Concentration dependent Zn diffusion in InP during metalorganic vapor phase epitaxy",** *S. N. G. Chu, R. A. Logan, M. Geva, N. T. Ha, J. Appl. Phys. 78 (1995), 3001-3007.*

[7] **"Zinc doping in InP grown by atmospheric pressure metalorganic vapor phase epitaxy",** *A. Molassioti, F. Scholz, Y. Gao, J. Cryst. Growth 102 (1990), 974-978.*

[8] **"Modeling of Zn diffusion in InP/InGaAs materials during MOVPE growth"**, *C. Y. Tai, J. Seiler, M. Geva, Conf. P. Indium Phosph. (1999), 245-248.*

[9] **"Zinc-doping of InP during chemical beam epitaxy using diethylzinc",** *W. T. Tsang, F. S. Choa, and N. T. Ha, J. Electron. Mater. 20 (1991), 541-544.*

[10] **"Zinc diffusion across the heterojunction in InP/InGaAsP Heterostructures",** *H. Jung, and P. Marschall, Jpn. J. Appl. Phys. 27 (1988), L2112-L2114.*

[11] **"Zn diffusion behavior at the InGaAsP/InP heterointerface grown using MOCVD"**, *K. Kadoiwa, K. Ono, Y. Ohkura, J. Cryst. Growth 297 (2006), 44-51.*

[12] **"Zn-doping in OMVPE growth InP:Zn/InGaAs/InP p-i-n double heterojunctions with InGaAs:Zn contacting layers",** *F. G. Kellert, S. R. Sloan, M. J. Ludowise, J. E. Turner, J. Electron. Mater. 21 (1992), 983-987.*

[13] **"Hydrogen passivation in InP:Zn resulting from reactive ion etching during laser stripe formation",** *J. Kreissl, M. Moehrle, A. Sigmund, R. Bochnia and P. Harde, W. Ulrici, Conf. Proc. Indium Phosph. (2000), 142-145.*

[14] **"Anomalous behaviour of dopants in atmospheric pressure MOVPE of InP",** *S. Cole, J. S. Evans, M. J. Harlow, A. W. Nelson, S. Wong, J. Cryst. Growth 93 (1988), 607-612.*

[15] **"Lithography. Theory and application of photoresists, developers, solvent and etchants",** *www.microchemicals.com*

[16] **"Selective etching and polymer deposition on InP surface in reactive ion etching with a mixture of methane and hydrogen",** *N. Yamamoto, J. Vac. Sci. Technol. B 27 (2009), L50-L53.*

[17] **"CH_4-based dry etching of high Q InP microdisks",** *S. J. Choi, K. Djordin, S. J. Choi, P.D. Dapkus, J.Vac. Sci. Technol. B 20 (2002), 301-306.*

[18] **"High rate CH_4:H_2 plasma etch processes for InP",** *C. S. Whelan, T. E. Kazior, K. Y. Hur, J. Vac. Sci. Technol. B 15 (2004), 1728-1732.*

[19] **"Reactive ion etching of InP for optoelectronic device applications: comparison in CH_4, CH_4/H_2, and CH_4/Ar gas",** *J. S. Yu, Y. T. Lee, J. Korean Phys. Soc. 37 (2000), 241-246.*

[20] **"Investigation of point defect generation in dry etched InP ridge waveguide structures",** *M. Avella, J. Jimenez, F. Pommereau, J. P. Landesman, A. Rhallabi, Appl. Phys. Lett. 90 (2007), 223510-223512.*

[21] **"CH_4/H_2 RIE of InGaAsP/InP materials: An application to DFB laser fabrication",** *G. Meneghini, L. Boschis, C. Coriasso, A. Stano, M. Gentili, L. Grella, M. Figliomeni, Microelectron. Eng. 21 (1993), 321-324.*

[22] **"Parametric reactive ion etching of InP using Cl_2 and CH_4 gases: effects of H_2 and Ar addition",** *J. S. Yu, Y. T. Lee, Semicond. Sci. Technol. 17 (2002), 230-236.*

[23] **"Reactive ion etching of InP/InAlGaAs/InGaAs heterostructures",** *C. Lemm, S. Kollakowski, D. Bimberg, K. Janiak, J. Electrochem. Soc. 144 (1997), L255-L257.*

[24] **"Fabrication of InP-based two-dimensional photonic crystal membrane",** *C A. Xing, M. Davanco, D. J. Blumenthal, E. L. Hu, J. Vac. Sci. Technol. B 22 (2004), 70-73.*

[25] **"Buried InAlGaAs-InP waveguides: etching, overgrowth, and characterization",** *S. Kollakowski, C. Lemm, A. Strittmatter, E. H. Bottcher, D. Bimberg, IEEE Photon. Technol. Lett.. 10 (1998), 114-116.*

[26] **"Fabrication of high-aspect-ratio InP-based vertical-cavity laser mirrors using $CH_4/H_2/O_2$/Ar reactive ion etching",** *J. E. Schramm, D. I. Babic, E. L. Hu, J. E. Bowers, J. L. Merz, J. Vac. Sci. Technol. B 15 (1997) , 2031-2036.*

[27] **"Simple and accurate loss measurement technique for semiconductor optical waveguides",** *R. G. Walker, Electron. Lett. 21 (1985), 581 - 583.*

[28] **"Reactive ion etching of InP using CH_4/H_2 mixtures: mechanisms of etching and anisotropy",** *T. R. Hayes, M. A. Dreisbach, P. M. Thomas, W. C. Dautremont-Smith, J. Vac. Sci. Technol. B 7 (1989) , 1130-1140.*

[29] **"Dry etching of III/V - semiconductors: fine tuning of pattern transfer and process control",** *J. Electrochem. Soc. 142(1995), 2418-2424.*

[30] **"High-Q vertically coupled InP microdisk resonators",** *K. Djordjev, S. J. Choi, P. D. Dapkus, IEEE Photonics Tech. Lett. 14 (2002), 331 - 333.*

[31] **"Nanofabrication of InGaAsP periodic 2D columns with square and hexagonal lattices by reactive ion etching",** *J. M. Lee, S. H. Oh, C. W. Lee, H. Ko, S. Park, K. S. Kim, M. H. Park, Thin Sol. Films 475 (2005), 189-193.*

[32] **"Low-loss III-V semiconductor optical waveguides",** *R. J. Deri, E. Kapon, IEEE J. Quant. Electron. 27 (1991), 626 - 640.*

[33] **"Au/Pt/Ti contacts to p-$In_{0.53}Ga_{0.47}As$ and n-InP layers formed by a single metallization common step and rapid thermal processing",** *A. Katz, B. E. Weir, W. C. Dautremont-Smith, J. Appl. Phys. 68 (1990), 1123 - 1128.*

[34] **"Formation of extremely low resistance Ti/Pt/Au ohmic contacts to p-GaAs",** *G. Stareev, Appl. Phys. Lett. 62 (1993), 2801 - 2803.*

[35] **"Comparison of Ti/Pt/Au and Ti/Ru/Au contact systems to p-type InGaP",** *V. Malina, K. Vogel, P. Ressel, W. O. Barnard, A. Knauer, Semicond. Sci. Technol. 12 (1997), 1298 - 1303.*

[36] **"A reliable fabrication technique for very low resistance ohmic contacts to p-InGaAs using low energy Ar^+ ion beam sputtering",** *G. Stareev, A. Umbach, J. Electron. Mater. 20 (1991), 1059 - 1063.*

[37] **"Microstructural analysis of Au/Pt/Ti contacts to p-type InGaAs",** *D. G. Ivey, P. Jian, J. Mater. Sci. 6 (1995), 219 - 227.*

[38] **"A controllable mechanism of forming extremely low-resistance nonalloyed ohmic contacts to group III-V compound semiconductors",** *G. Stareev, H. Kunzel, G. Dortmann, J. Appl. Phys. 74 (1993), 7344 - 7356.*

[39] **"Pt/Ti Ohmic contact to p++-InGaAsP (1.3 µm) formed by rapid thermal processing",** *A. Katz, P. M. Thomas, S. N. G. Chu, W. C. Dautremont-Smith, R. G. Sobers, S. G. Napholtz, J. Appl. Phys. 67 (1990), 884 - 889.*

[40] **"Pt/Ti/p-$In_{0.53}Ga_{0.47}As$ low-resistance nonalloyed ohmic contact formed by rapid thermal processing",** *A. Katz, W. C. Dautremont-Smith, S. N. G. Chu, P. M. Thomas, L. A. Koszi, J. W. Lee, V. G. Riggs, R. L. Brown, S. G. Napholtz, J. L. Zilko, A. Lahav, Appl. Phys. Lett. 54 (1989), 2306 - 2308.*

[41] **"AuGe/Au ohmic contacts to n-type InP by hot-plate alloying",** *S. C. Binari, J. B. Boos, Electron. Lett. 25 (1989), 1207 - 1209.*

Chapter 4

Broad-Waveguide Laser Design

4.1 Introduction

For a laser to satisfy certain characteristics predetermined by its application, it has to be properly designed. However, laser design is very challenging task because many design details can interplay and thus strongly affect the laser performance. This is even more so when the laser design is not based on previously developed devices but designed from scratch. This requires a strong understanding of laser physics and numerical modelling methods.

In this chapter the advantages of broad-waveguides (transverse direction) laser will be discussed. The process of designing the laser will be presented including, quantum well and barrier material composition, number of quantum wells, waveguide width and p-doping level. Finally the performance of these lasers will be compared with standard waveguide lasers.

4.2 Broad-Waveguide Lasers

There are numerous studies reporting significant increase of output power from lasers with broad-waveguides [1-9]. The main reason for the improved performance in broad-waveguide lasers is low optical loss. The reduction of optical losses can mostly be attributed to reduced interaction of optical field with highly doped cladding regions and to a lesser extent, to lower active region optical confinement factor resulting in lower free carrier absorption in the quantum wells. Free carrier absorption in highly doped cladding regions, especially p-doped region can be very significant [1,2,10]. Hence reduction of optical field overlap with cladding regions considerably increases the laser output power.

Unlike InP lasers, GaAs lasers are able to produce much higher output power, however they suffer from catastrophic optical damage (COD), which limits their maximum output power. Catastrophic optical damage is a laser facet degradation phenomenon caused by radiation absorption. When the power density exceeds the critical level the active region at the facet rapidly heats up and melts. When the broad-waveguide concept is applied to GaAs lasers the reduced optical confinement factor of the active region results in lower power density, hence a later onset of COD and higher maximum output power.

These advantages make the broad-waveguide laser concept very appealing for application in high power lasers. Indeed it attracted a lot of attention from researchers in the past decade and resulted in many records of output power.

4.3 Laser Design and Numerical Modelling

For numerical modelling we used a commercially available software package LaserMOD from RSOFT. It is an integrated software package for designing and numerical modelling of semiconductor lasers. LaserMOD includes a number of mode solvers including Beam Propagation Method (BMP), a free-carrier 8x8 band k•p gain calculation method, rate based carrier capture between bound and continuum states, and drift-diffusion equations fully coupled with thermionic emission and photon rate equations [11].

To perform numerical modelling a laser diode layout has to be constructed. This involves specifying the laser structure, including various material parameters. Even though LaserMOD contains a number of material files for various semiconductor materials including InP/InGaAsP/InGaAs (used in this work) with reasonable default values, for more accurate simulations some of the material coefficients had to be adjusted. The value of Lorentzian broadening used in the calculation was chosen based on widely reported [12] value of intraband relaxation time of 0.1 ps. Shockley-Read-Hall (SRH) recombination value of 10^{-7} s was selected [12,13]. Free carrier absorption values of 1.6×10^{-18} cm^2 for electrons and 21.5×10^{-18} cm^2 for holes were chosen for the calculations [1,14,15]. Auger recombination coefficient was selected to be 3.5×10^{-28} cm^{-6}/s [13,16,17].

Another important parameter to be adjusted is the material electron affinity. The value of InP electron affinity is 4.4 eV, and $InGaAs_xP$ electron affinity can be expressed as $Y=(4.4+0.268*X+0.003*X^2)$ eV [18]. Since no electron affinity expression for InGaAs could be found in the literature a polynomial curve to known electron affinity values of $InGa_xAs$ (x=0, 0.47, 1) [18] was fitted resulting in $Y=(4.9-0.26758*X-0.56242*X^2)$ eV as illustrated in Fig 4.1. This expression for InGaAs affinity was used in the simulations.

A proven InGaAs/InGaAsP material system was chosen for the active region. This material system is well studied and is commonly used in lasers designed to operate in the S, C, L and U bands (1460 – 1675 nm). Lattice matched InGaAsP (to InP) was selected as the barrier. The barrier layer composition was selected to provide the maximum barrier height for a singular confined electron level in QW.

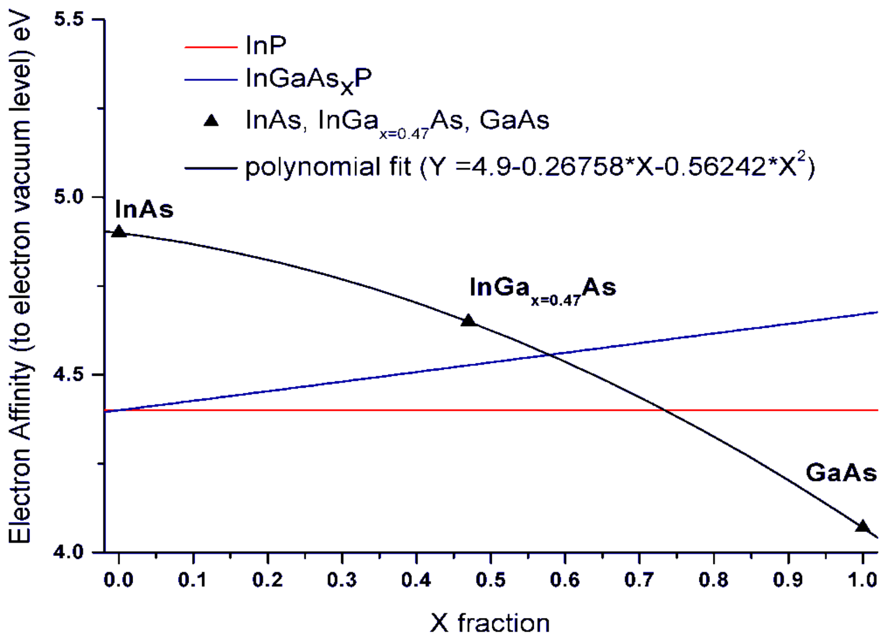

Figure 4.1 The dependence of electron affinity of various materials on their material composition.

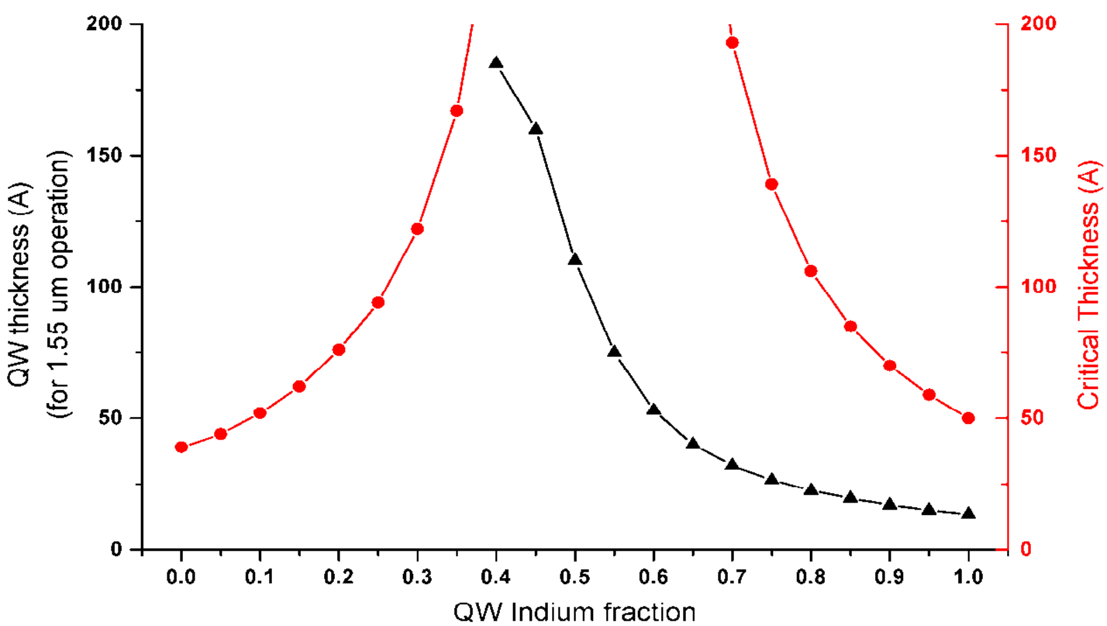

Figure 4.2 Dependence of InGaAs QW thickness (for 1.55 μm operation) and critical thickness on Indium fraction.

In the beginning the material composition of the quantum well (QW) had to be selected. The effect of lattice mismatch between epitaxial InGaAs layer and InP substrate has to be considered when designing the QW to avoid excessive strain and material relaxation. InGaAs is lattice matched to InP at the indium fraction of 0.53. Below this value InGaAs layer grown on InP will be tensile strained and above it will be compressively strained. Lattice mismatch limits the range of indium variation in the QW as shown in Fig. 4.2. The red curve represents the critical thickness of InGaAs epitaxial layer on InP substrate beyond which material relaxation is expected and the black curve represents the thickness of InGaAs QW within InGaAsP barrier adjusted for operation at 1.55 µm. As can be seen from Figure 4.2 the QW indium fraction can be varied from 0.4 to 1 without the material suffering relaxation. This is the range of composition that will be considered for QW optimisation.

The next step is QW optimisation for maximum gain. Figure 4.3 illustrates the dependence of material gain on QW indium fraction. Material gain is very low for tensile strained InGaAs and zero gain value is obtained for the assumed injection current at

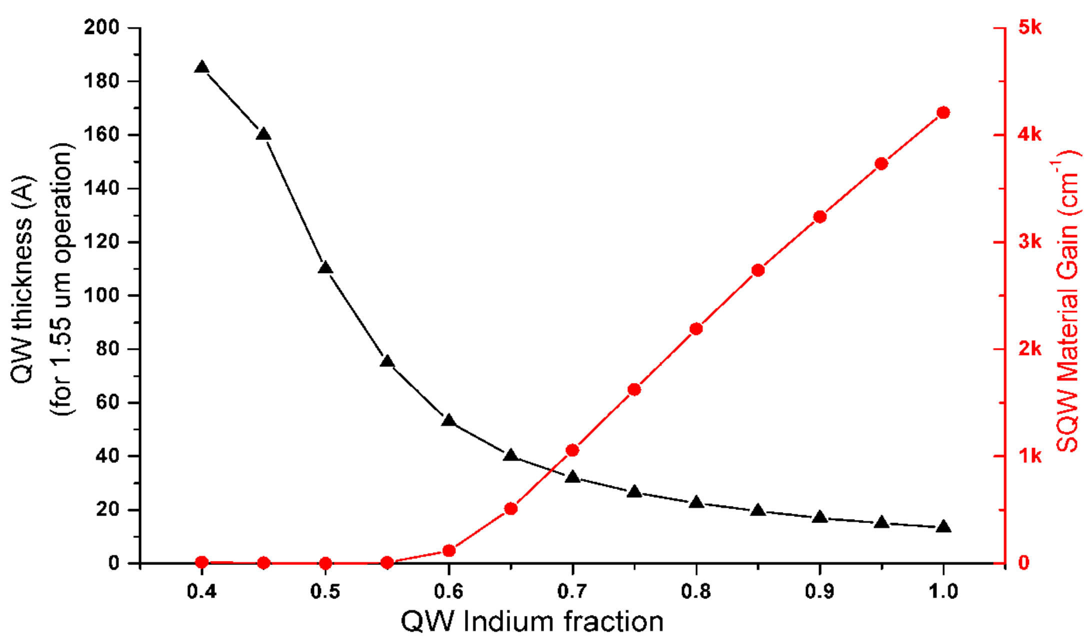

Figure 4.3 Dependence of InGaAs QW thickness (for 1.55 µm operation) and material gain on Indium fraction.

indium fraction of 0.5, which is expected due to higher density of states in unstrained material. For compressively strained QW the material gain increases rapidly with increasing indium fraction. Intuitively one would simply select the material composition with the highest material gain. However the second plot in the figure represents the thickness of InGaAs QW within InGaAsP barrier adjusted for operation at 1.55 μm, which decreases quickly with increase in indium fraction. This results in an overall gain reduction of the QW due to the smaller volume of gain medium. To illustrate this effect material gain was multiplied by the respective QW thickness and the results are shown in Fig. 4.4. The resulting curve has a saturation region for indium fractions above 0.8.

The other curve in Fig. 4.4 represents electron confinement level in the QW for different InGaAs compositions. Since the electron confinement is related to the dimensions of the QW it peaks at indium fraction of 0.5 and drops with increasing indium fraction.

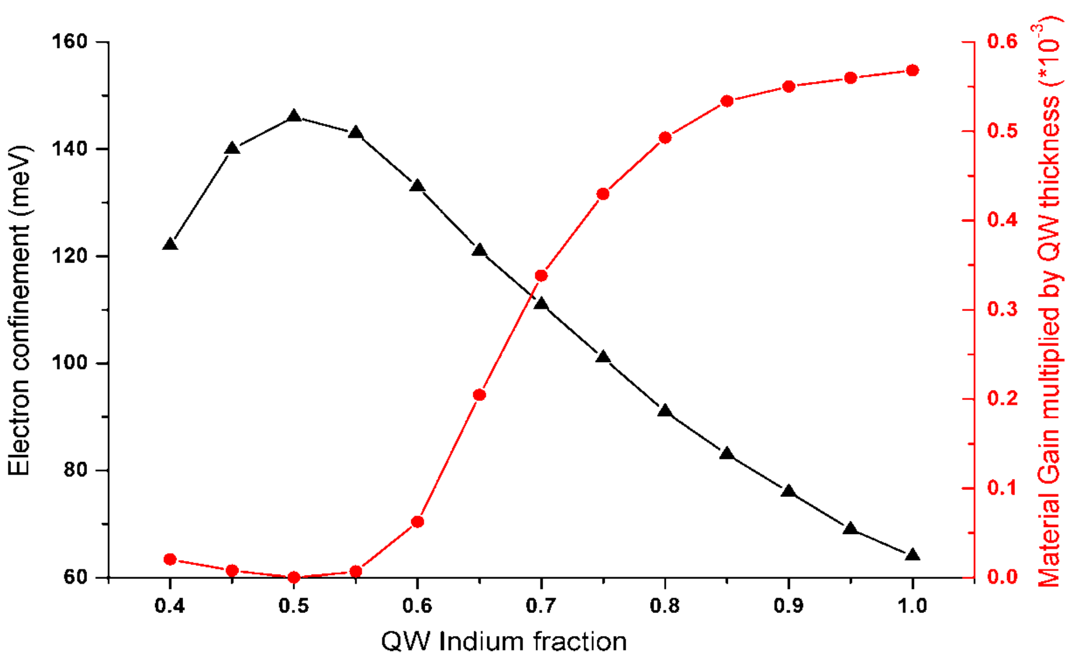

Figure 4.4 Dependence of InGaAs QW thickness (for 1.55 μm operation) multiplied by the material gain and electron confinement on Indium fraction.

Electron confinement is very important for lasers with InGaAs/InGaAsP active region in which 60% of the bandgap discontinuity is in the valence band. This is particularly important for high power lasers intended to operate at high injection currents where it has been shown that substantial amount of injected carriers can leak out of the active region [19-21]. At high injection the leakage current becomes very significant, resulting in device heating, reduced efficiency and low output power.

Therefore both gain and electron confinement have to be considered when designing the active region of high power lasers. The region with indium fraction below 0.6 is disregarded due to very low gain and multiple electron levels in the QW. The region with indium fraction above 0.8 is unsuitable due to steadily dropping electron confinement, while the gain increases just marginally. Hence as a compromise between high gain and high electron confinement, InGaAs material compositions with indium fractions in the range of 0.6 – 0.8 were selected for device simulations.

Next a number of laser simulations were initiated to determine the best combination of QW, barrier and waveguide material compositions. Various material compositions used in the simulations are presented in Table 4.1.

Figure 4.5 illustrates the simulation results of lasers with $In_{0.60}GaAs$ single quantum well (SQW) for various combinations of barrier, waveguide compositions. The best performance was consistently obtained for all simulated QW material compositions with barrier/waveguide combination of $In_{0.79}GaAs_{0.45}P/In_{0.86}GaAs_{0.30}P$. The best performing QW was $In_{0.60}GaAs$ due to better electron confinement and lower carrier leakage, resulting in less rollover. Hence a combination of QW/barrier/waveguide – $In_{0.60}GaAs/In_{0.79}GaAs_{0.45}P/In_{0.86}GaAs_{0.30}P$ was selected.

Even though theory predicts better performance from lasers with single quantum well over multiple quantum wells for long devices [22], an active region consisting of five

Quantum Well	Waveguide	Barrier
Q_1 – $In_{0.60}GaAs$	W_1 – $In_{0.93}GaAs_{0.15}P$	B_1 – $In_{0.86}GaAs_{0.30}P$
Q_2 – $In_{0.65}GaAs$	W_2 – $In_{0.86}GaAs_{0.30}P$	B_2 – $In_{0.79}GaAs_{0.45}P$
Q_3 – $In_{0.70}GaAs$	W_3 – $In_{0.79}GaAs_{0.45}P$	B_3 – $In_{0.73}GaAs_{0.57}P$
Q_4 – $In_{0.75}GaAs$	-//-	-//-
Q_5 – $In_{0.80}GaAs$	-//-	-//-

Table 4.1 Various quantum well, barrier and waveguide material compositions used in laser simulations.

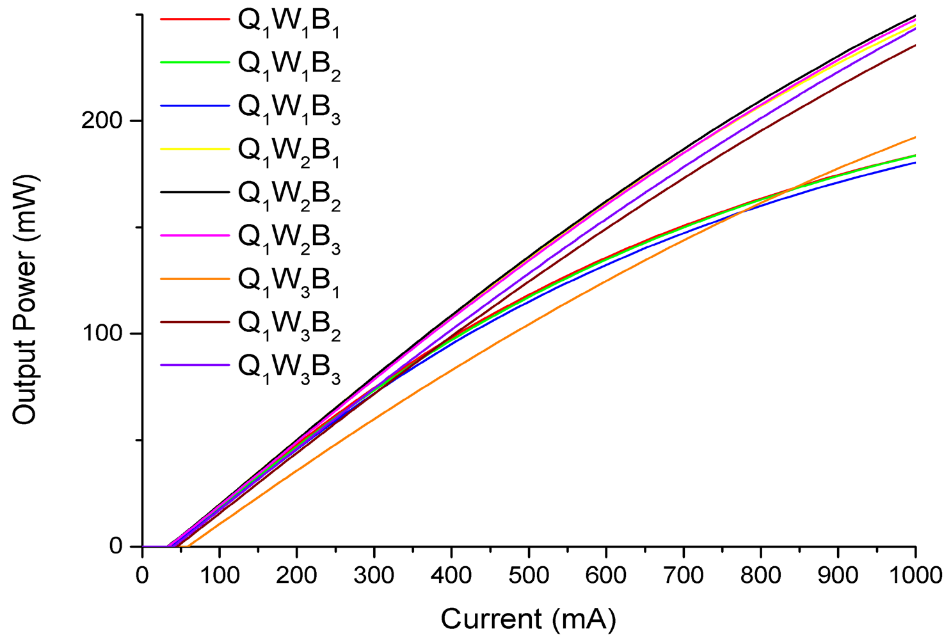

Figure 4.5 Numerically modelled L-I curves of lasers with various QW/ waveguide/ barrier combinations (Curves are indexed according to Table 4.1).

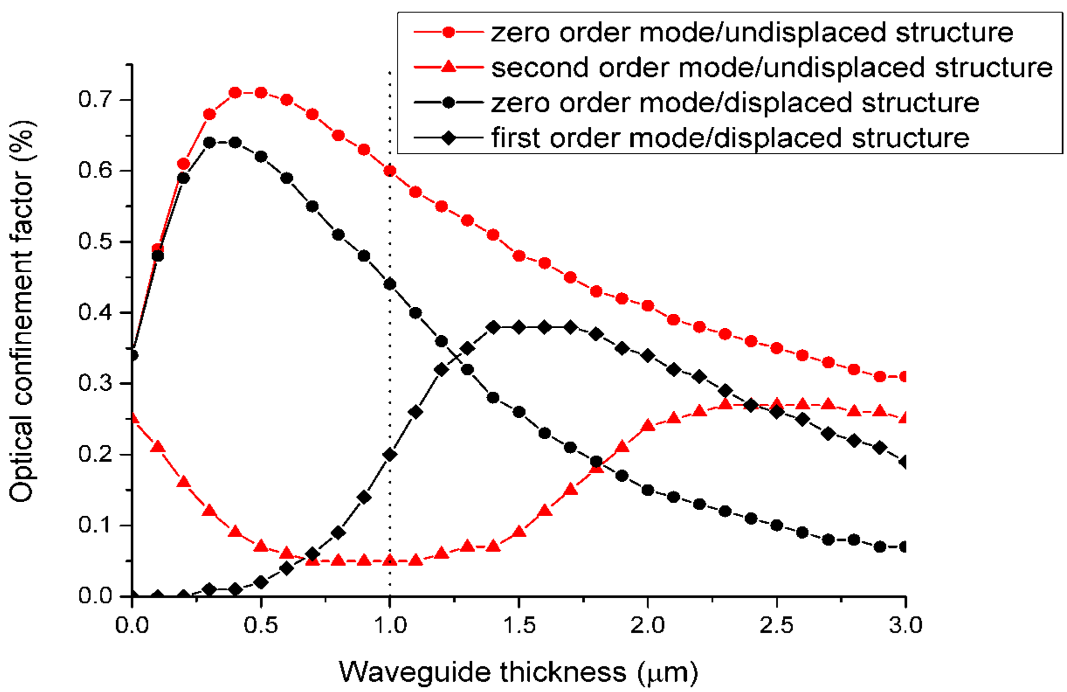

Figure 4.6 Numerically modelled optical confinement factor for fundamental and higher order modes in structures with undisplaced and displaced active regions.

quantum wells was selected for device fabrication to provide a gain safety net for any unexpected losses caused by material or fabrication imperfections.

Although the laser performance is expected to improve with the increase of the waveguide thickness, the purpose of this work is to improve the power output of single mode laser and therefore waveguides supporting higher order modes should be avoided. To determine the waveguide cut-off thickness for single mode operation optical confinement factor for fundamental, first and second order modes were calculated (illustrated in Figure 4.6). For a symmetrical waveguide (undisplaced active region structure) the first order mode can be ignored due to mode minimum at the active region, resulting in waveguide thickness of 2.5 μm at which the second order mode confinement factor becomes comparable to the confinement factor of the fundamental mode. However for the structures with active region displaced from the middle of the waveguide (discussed in Chapter 5), the first order mode has to be considered. The first order mode will dominate in the structure with such a thick waveguide and the active region displaced from the middle of the waveguide. This will make the comparison of different structures impossible. Hence a 1 μm thick waveguide was selected since it produces maximal waveguide thickness while still producing sufficient discrimination of higher order modes in both undisplaced and displaced active region structures.

A number of reports [23-26] show increase in laser output power from devices with increasing p-doping levels. Some studies experimentally measured the electron leakage current [19,20], reporting a superlinear increase of the leakage current with increasing injection current. Thermionic leakage current contributes to the reduction of the laser efficiency and as a result light output rollover.

Hence doping level in the p-cladding region has to be optimised as this will determine the electron thermionic leakage current. Due to their much lower mass compared to holes, electrons require higher confinement energy. This is even more critical for InP/InGaAsP material system, since about 60% of the bandgap discontinuity is in the valence band, resulting in insufficient electron confinement and very strong hole confinement. Hence, hole thermionic leakage current is negligible and can be ignored.

To determine the influence of p-doping on laser performance and to determine the optimum doping level a set of laser structures was simulated. The resulting L-I curves of three simulated structures with doping levels of $2x10^{16}$ cm^{-3}, $2x10^{17}$ cm^{-3} and $2x10^{18}$ cm^{-3} are shown in Fig. 4.7. These doping levels are easily achievable in MOCVD grown InP.

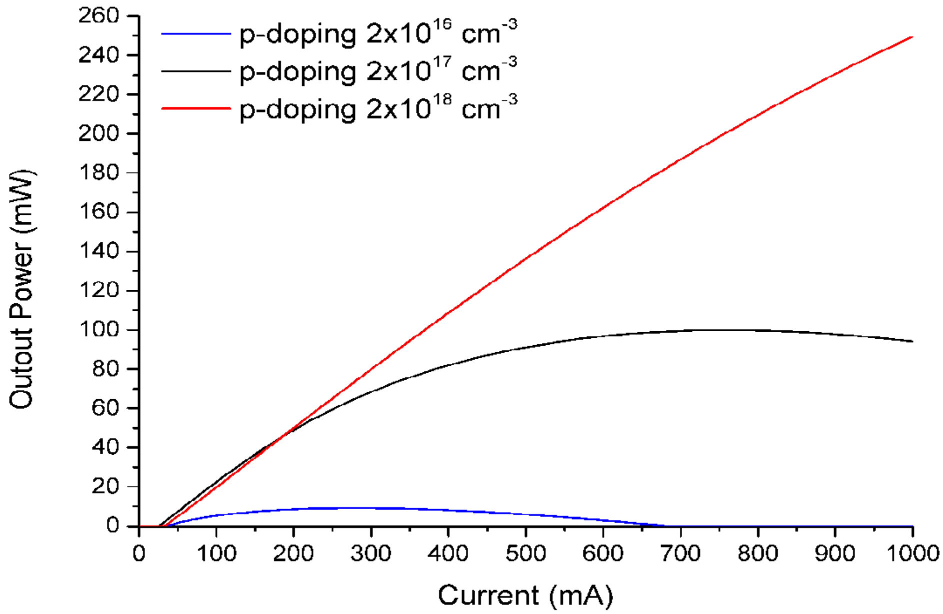

Figure 4.7 Simulated L-I curves of lasers with different doping levels in the p-clad layer.

From this figure it is clear that higher doping level improves the output power of the laser, which is the result of reduced electron thermionic leakage into the p-cladding region. Under an applied bias the laser bandstructure becomes distorted. Due to lower hole mobility most of the distortion happens at the p-cladding region. The level of p-doping of this region can affect the resulting band profile substantially. As illustrated in Fig. 4.8 high doping level reduces the effect of electron heterobarrier lowering caused by an applied bias and thus decreases the electron leakage current. This in turn leads to less rollover and higher optical output power. This result is consistent with the results reported in literature [23-26]. Therefore doping level of $2x10^{18}$ cm^{-3} was selected. This doping level is close to maximum achievable for Zn doped MOCVD grown InP, as reported in the literature [27,28]. The final broad-waveguide laser structure is presented in Tab. 4.2.

To evaluate the performance of broad-waveguide lasers, a set of thin-waveguide lasers were also fabricated. The thin-waveguide laser structure is identical to the one presented in Tab. 4.2 with the only exception of the waveguiding layers thickness which are reduced to 100 nm.

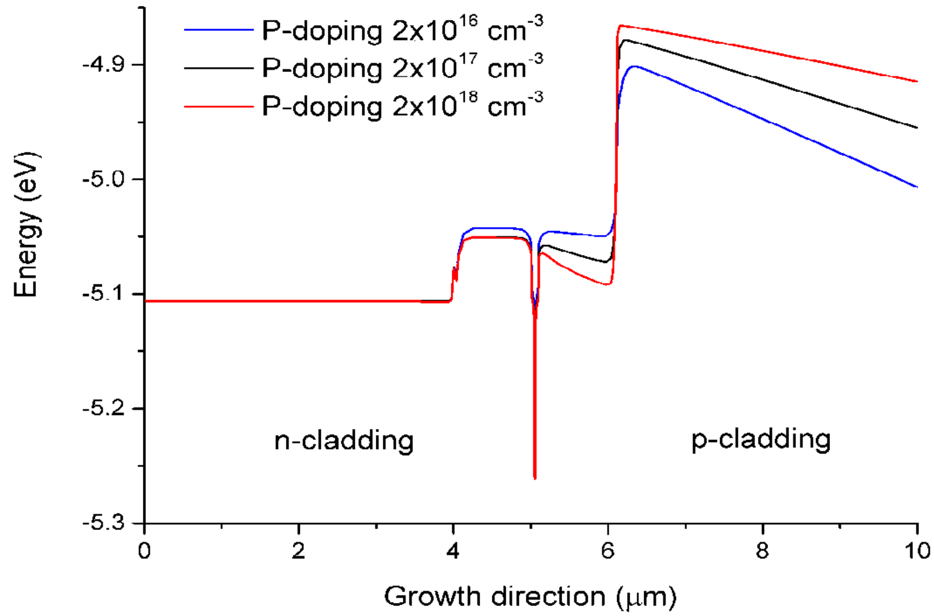

Figure 4.8 Simulated conduction band profiles of lasers with various p-clad doping level under moderate injection.

Material	Doping (cm^{-3})	Layer thickness (μm)	Bulk bandgap (eV)	Structural function
$In_{0.53}Ga_{0.47}As$	Zn $1x10^{19}$	0.05	0.74	Contact layer
InP	Zn $2x10^{18}$	1.5	1.35	p-cladding
InP	no	0.5	1.35	
$In_{0.86}Ga_{0.14}As_{0.30}P_{0.70}$	no	0.5	1.13	Waveguide
$In_{0.79}Ga_{0.21}As_{0.45}P_{0.55}$	no	0.02	1.03	Active region
$In_{0.6}Ga_{0.4}As$	no	0.005	0.67	
$In_{0.79}Ga_{0.21}As_{0.45}P_{0.55}$	no	0.01	1.03	
$In_{0.6}Ga_{0.4}As$	no	0.005	0.67	
$In_{0.79}Ga_{0.21}As_{0.45}P_{0.55}$	no	0.01	1.03	
$In_{0.6}Ga_{0.4}As$	no	0.005	0.67	
$In_{0.79}Ga_{0.21}As_{0.45}P_{0.55}$	no	0.01	1.03	
$In_{0.6}Ga_{0.4}As$	no	0.005	0.67	
$In_{0.79}Ga_{0.21}As_{0.45}P_{0.55}$	no	0.01	1.03	
$In_{0.6}Ga_{0.4}As$	no	0.005	0.67	
$In_{0.79}Ga_{0.21}As_{0.45}P_{0.55}$	no	0.02	1.03	
$In_{0.86}Ga_{0.14}As_{0.30}P_{0.70}$	no	0.5	1.13	Waveguide
InP	Si $2x10^{18}$	0.1	1.35	n-cladding
InP	Si $2x10^{18}$	0.2	1.35	
Substrate	S $2x10^{18}$	-//-	1.35	

Table 4.2 Detailed description of the designed broad-waveguide laser structure.

4.4 Experimental results

Laser structures with broad-waveguide and thin waveguide were grown and processed together as described in Chapter 3 (Fabrication Issues). To estimate the material quality room temperature PL of the as-grown structures were measured. To avoid PL signal reabsorption prior to PL measurement the samples had their InGaAs contact layers and p-cladding layers selectively etched off.

The PL spectra are presented in Fig. 4.9 which shows the peak amplitudes of two curves are significantly different. The reduction of PL from sample with thin-waveguide structure is the result of Zn diffusion into the active region, as described in Chapter 3. In thin-waveguide structure the active region overlaps with the Zn "tail" and as a result more Zn is incorporated into the active region. Otherwise the two spectra are quite similar with FWHM of 165 nm for broad-waveguide and 159 nm for thin-waveguide structure

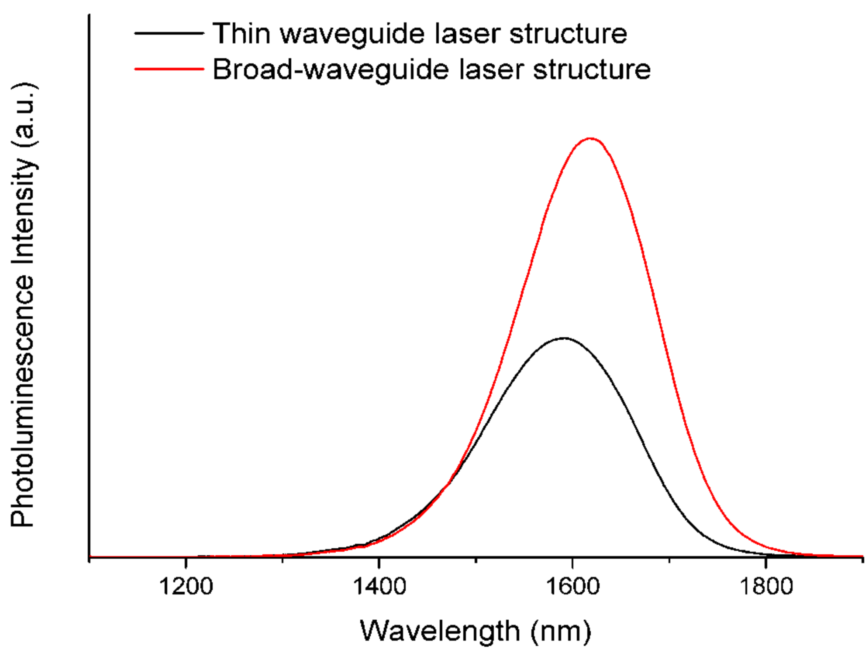

Figure 4.9 Photoluminescence spectra of thin-waveguide and broad-waveguide laser structures (p-doped InGaAs and InP selectively etched off).

and peaks at 1618 and 1592 nm, respectively. The slight variation in the peak wavelengths is due to the small run-to-run variation in the MOCVD system.

Both samples were cleaved into separate devices of 1, 1.5, 2 and 3 mm in length and tested. The devices were tested as described in Chapter 2 (Experimental Techniques).

The L-I curves of the broad-waveguide laser and thin-waveguide laser of 3 mm in length are shown in Fig. 4.10. The thin-waveguide laser produced less rollover and as a result higher maximum output power. Similar results were obtained for all the devices of various lengths as illustrated in Fig. 4.11.

Even though this result might look counterintuitive, it reveals the complexity of laser operation and highlights the importance of factors other than optical loss to laser operation. Higher output power from thin-waveguide lasers can be explained as follows.

Figures 4.12 and 4.13 show the dependence of inverse external differential efficiency on laser cavity length for thin-waveguide and broad-waveguide lasers, respectively. The active regions of both structures provide identical internal differential efficiency of 31% indicating no major degradation due to the expected slightly higher Zn incorporation in the thin-waveguide structure. As expected broad-waveguide structure produces very low

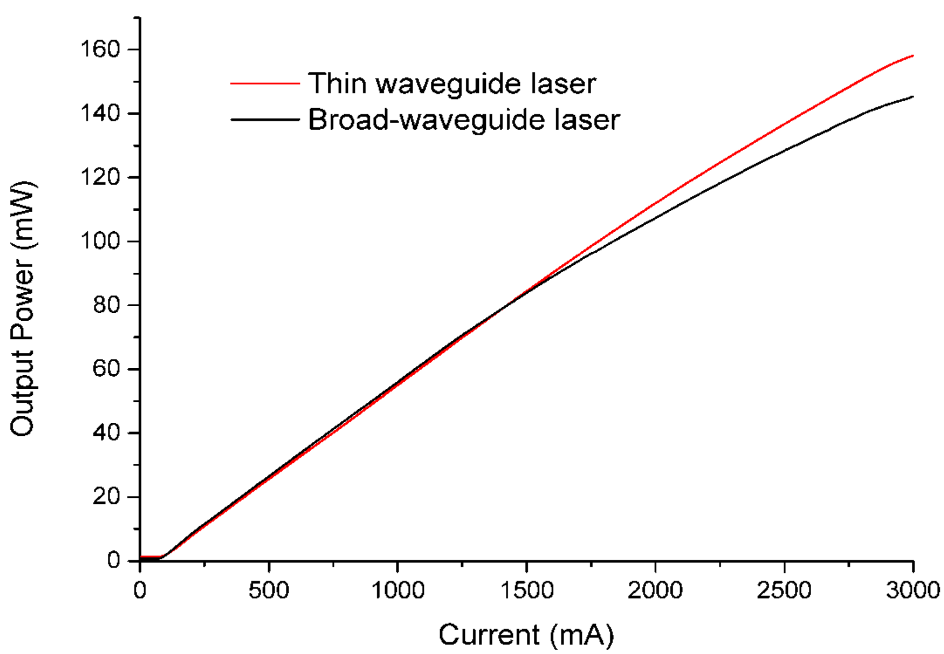

Figure 4.10 Light-current curves of 3 mm long thin-waveguide and broad-waveguide.

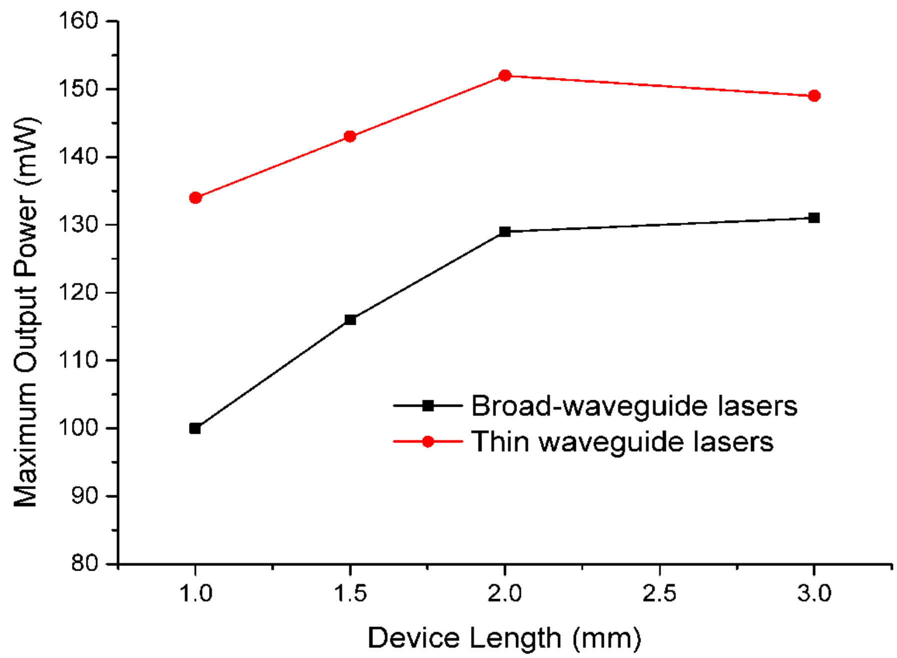

Figure 4.11 Averaged maximum output power of thin-waveguide and broad-waveguide lasers of various lengths.

optical loss of 2.3 cm^{-1}. Even though the thin-waveguide structure has an optical loss of 4.3 cm^{-1}, which is almost double that of the broad-waveguide laser it is still relatively low. This indicates only a minor increase of the optical loss due to greater mode overlap with the highly doped p-cladding region, which can be attributed to the optimised Zn doping (Chapter 3). Increased optical loss of the thin-waveguide lasers is reflected in higher threshold current density of 300 A/cm^2 compared to 170 A/cm^2 for broad-waveguide lasers as shown in Fig. 4.14 and Fig. 4.15.

This additional optical loss is not sufficient to drastically reduce the laser performance of thin-waveguide lasers. This could be due to better carrier injection in thin-waveguide lasers due to the close proximity of the active region to the highly doped cladding regions. The L-I curve rollover in Fig. 4.10 of broad-waveguide laser could be an indication of increasing electron leakage which is the result of reduced conduction band potential, which is confirmed by simulation. Figure 4.16 depicts numerically modelled conduction band diagrams of both structures under the same injection current. The electron potential barrier of the broad-waveguide laser is more strongly deformed

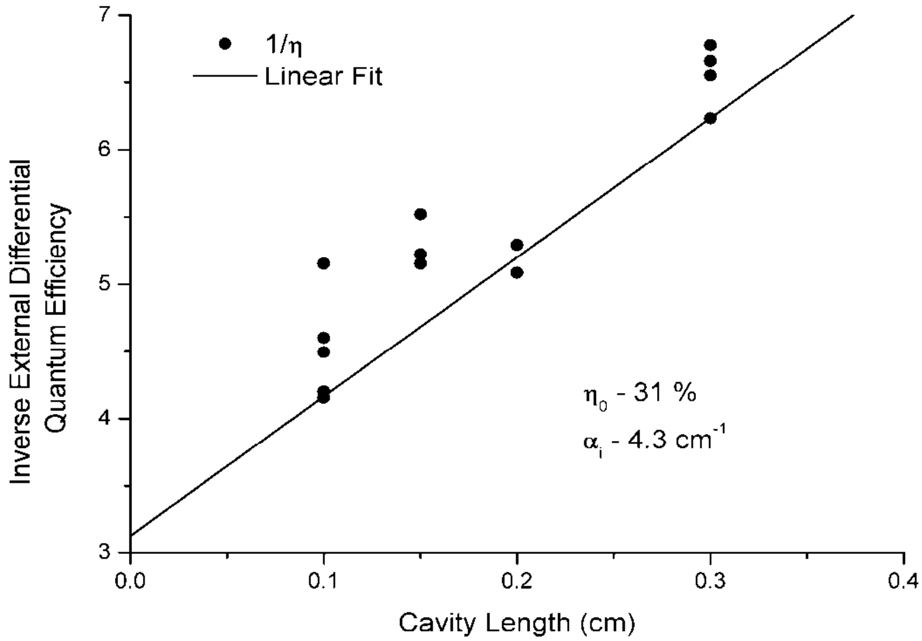

Figure 4.12 Dependence of inverse external differential quantum efficiency of thin-waveguide lasers on cavity length.

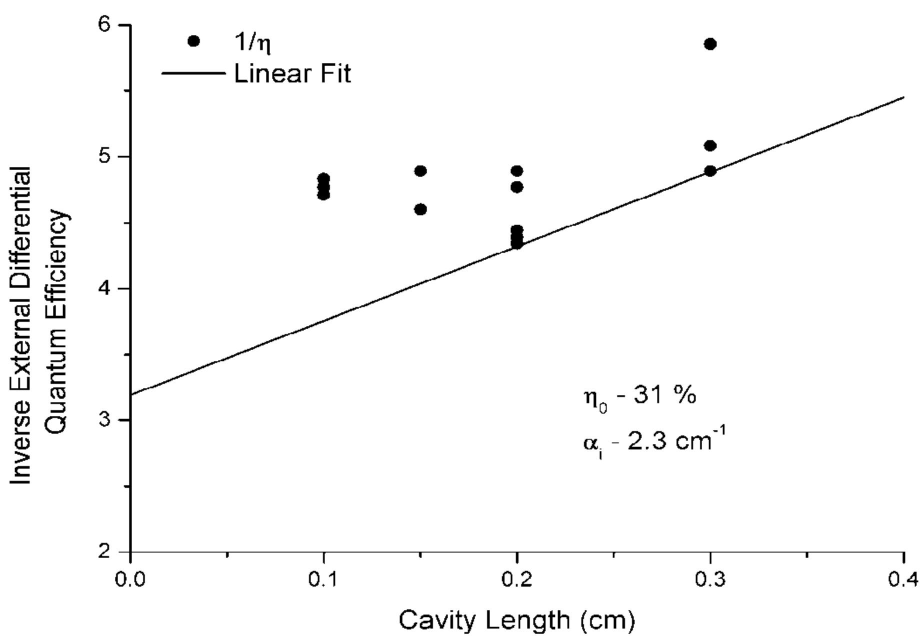

Figure 4.13 Dependence of inverse external differential quantum efficiency of broad-waveguide lasers on cavity length.

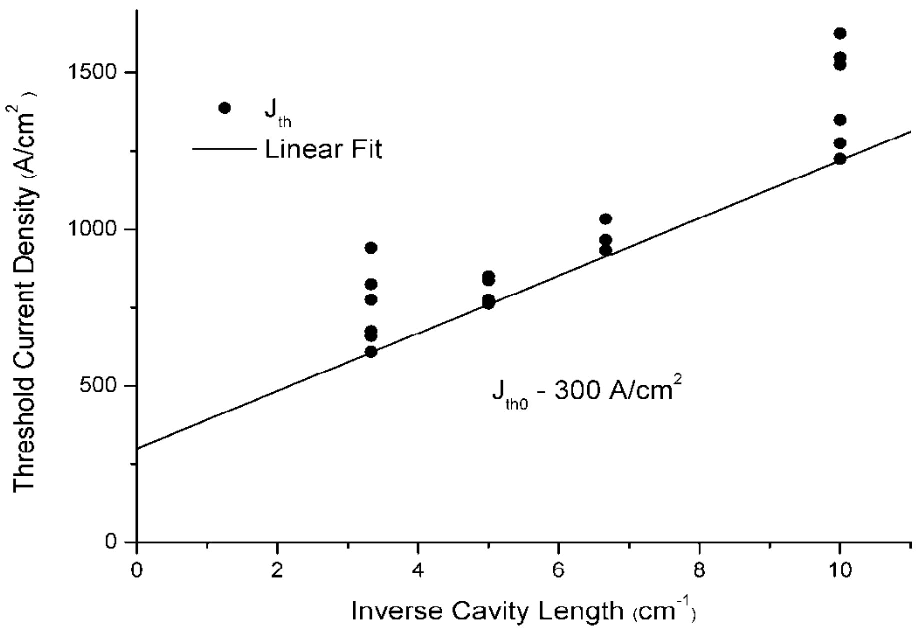

Figure 4.14 Threshold current density of thin-waveguide lasers as a function of inverse cavity length.

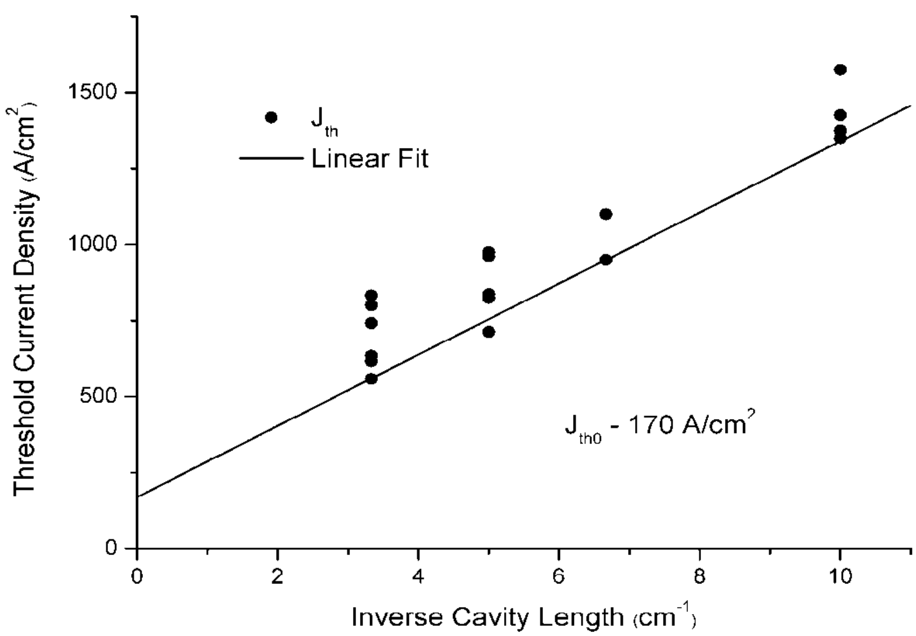

Figure 4.15 Threshold current density of broad-waveguide lasers as a function of inverse cavity length.

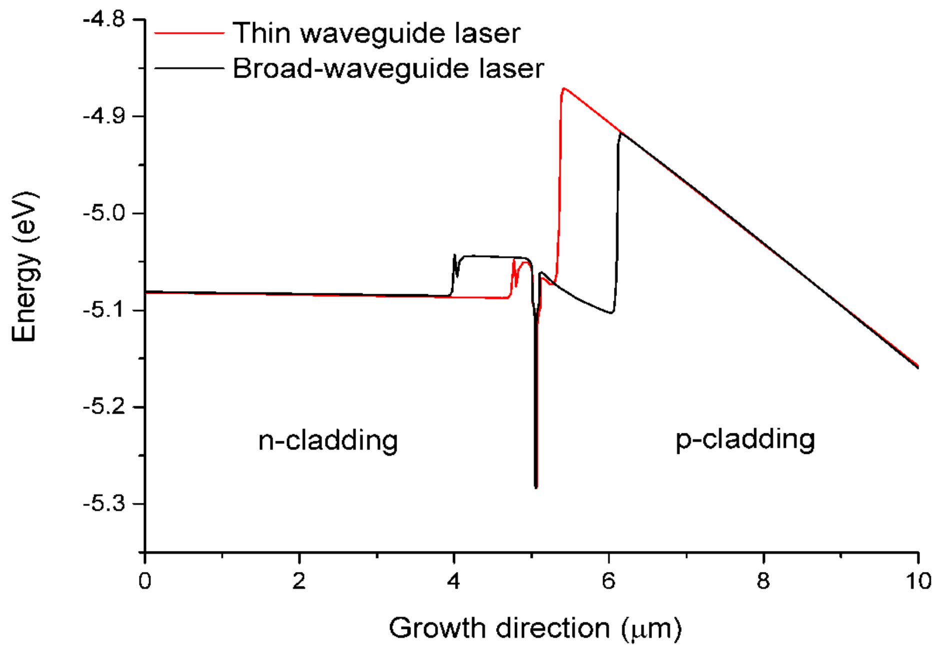

Figure 4.16 Numerically modelled conduction bands of thin-waveguide and broad-waveguide lasers under identical injection.

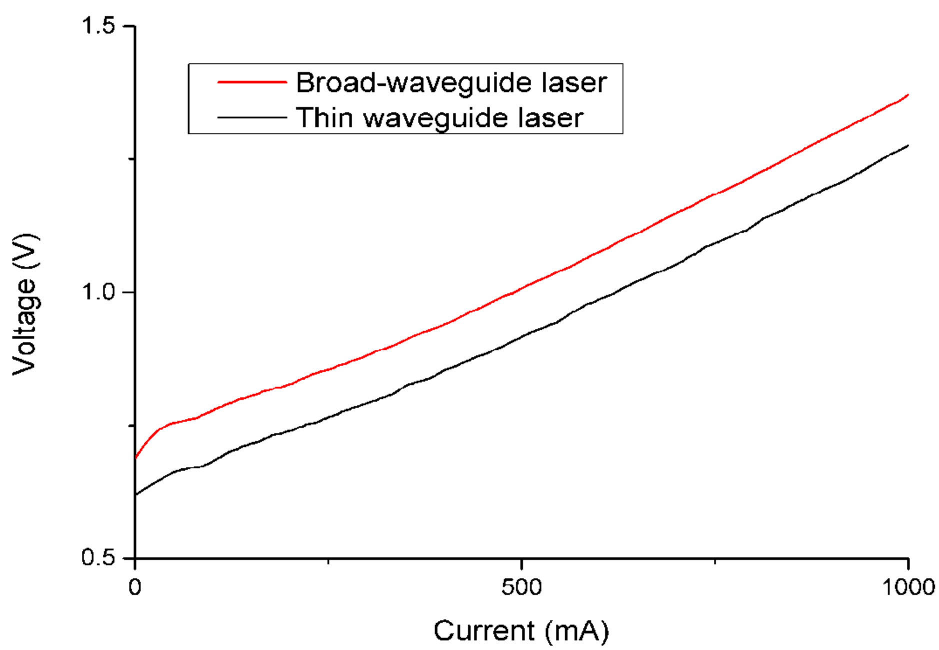

Figure 4.17 Typical current-voltage curves of thin-waveguide and broad-waveguide lasers.

compared to the thin-waveguide laser as a result of higher applied bias required to achieve the needed injection level due to less efficient hole injection. Figure 4.17 shows typical I-V curves of two structures, clearly illustrating a higher operation voltage of the broad-waveguide laser.

4.5 Conclusion

Broad-waveguide design significantly reduced the laser internal loss which is a requirement for high power laser operation. However broad-waveguide decreases hole injection efficiency resulting in higher bias required for operation. This, in turn, reduces the p-cladding conduction band potential resulting in higher electron leakage, L-I rollover and lower maximum output power. Hence to benefit from the broad-waveguide design and to increase laser output power the issue of hole injection has to be resolved. Investigation of the hole injection process in the broad-waveguide laser is the subject of the next chapter.

References

[1] "**1.5 µm wavelength, SCH-MQW InGaAsP/InP broadened-waveguide laser diodes with low internal loss and high output power**", D. *Garbuzov, L. Xu, S. R. Forrest, R. Menna, R. Martinelli, and J. C. Connolly, Electron*. *Lett*. 32 *(1996), 1717-1719.*

[2] "**High-power high-efficiency 0.98-µm wavelength InGaAs-(In)GaAs(P)-InGaP broadened waveguide lasers grown by gas-source molecular beam epitaxy"**, *M. R. Gokhale, J. C. Dries, P. V. Studenkov, S. R. Forrest, D. Z. Garbuzov, IEEE J. Quantum Electron. 33 (1997), 2266-2276.*

[3] "**Effects of broad-waveguide structure in 0.8 µm high-power InGaAsP/InGaP/AlGaAs lasers"**, *T. Hayakawa, M. Wada, F. Yamanaka, H. Asano, T. Kuniyasu, T. Ohgoh, and T. Fukunaga, Appl. Phys. Lett. 75 (1999), 1839-1841.*

[4] "**High-power (>10 W) continuous-wave operation from 100-µm-aperture 0.97-µm-emitting Al-free diode lasers"**, *A. Al-Muhanna, L. J. Mawst, D. Botez, D. Z. Garbuzov, R. U. Martinelli, and J. C. Connolly, Appl. Phys. Lett. 73 (1998), 1182-1184.*

[5] "**14.3 W quasicontinuous wave front-facet power from broad-waveguide Al-free 970 nm diode lasers"**, *A. Al-Muhanna, L. J. Mawst, D. Botez, D. Z. Garbuzov, R. U. Martinelli, and J. C. Connolly, Appl. Phys. Lett. 71 (1997), 1142-1144.*

[6] "**2.3-2.7-µm room temperature CW operation of InGaAsSb-AlGaAsSb broad waveguide SCH-QW diode lasers"**, *D. Z. Garbuzov, H. Lee, V. Khalfin, R. Martinelli, J. C. Connolly, and G. L. Belenky, IEEE Photon. Technol. Lett. 11 (1999), 794-796.*

[7] "**8 W continuous wave front-facet power from broad-waveguide Al-free 980 nm diode lasers"**, *L. J. Mawst, A. Bhattacharya, J. Lopez, D. Botez, D. Z. Garbuzov, L. DeMarco, J. C. Connolly, M. Jansen, F. Fang, and R. F. Nabiev, Appl. Phys. Lett. 69 (1996), 1532-1534.*

[8] "**High power InGaAsP/InP broad-waveguide single-mode ridge-waveguide lasers**", *M. Maiorov, R. Menna, A. Komissarov, D. Z. Garbuzov, and J. Connolly, OFC 4 (2001), WC2 1-3.*

[9] "**Slab-coupled 1.3-μm semiconductor laser with single-spatial large-diameter mode**", *J. N. Walpole, J. P. Donnelly, P. J. Taylor, L. J. Missaggia, C. T. Harris, R. J. Bailey, A. Napoleone, S. H. Groves, S. R. Chinn, R. Huang, and J. Plant, IEEE Photon. Technol. Lett.. 14 (2002), 756-758.*

[10] "**Low loss, thin p-clad 980-nm InGaAs semiconductor laser diodes with an asymmetric structure design**", *M. Buda, J. Hay, H. H. Tan, J. Wong-Leung, and C. Jagadish, IEEE J. Quantum Electron. 39 (2003), 625-633.*

[11] "**LaserMOD user guide**", *RSOFT Design Group, Inc.*

[12] "**Self-consistent analysis of high-temperature effects on strained-layer multiquantum-well InGaAsP-InP lasers**", *J. Piprek, P. Abraham, and J. E. Bowers, J. Quantum Electron. 36 (2000), 366-374.*

[13] "**Auger recombination in bulk and quantum well InGaAs**", *S. Hausser, G. Fuchs, A. Hangleiter, K. Streubel, and W. T. Tsang, Appl. Phys. Lett. 56 (1990), 913-915.*

[14] "**Double doped low etch pit density InP with reduced optical absorption**", *A. A. Ballman, A. M. Glass, R. E. Nahory, and H. Brown, J. Cryst. Growth 62 (1983), 198-202.*

[15] "**Variation of intervalence band absorption with hole concentration in p-type InP**", *H. C. Casey, and P. L. Carter, Appl. Phys. Lett. 44 (1984), 82-83.*

[16] "**Compositional dependence of the Auger coefficient for InGaAsP lattice matched to InP**", *W. Bardyszewski, and D. Yevick, J. Appl. Phys. 58 (1985), 2713-2723.*

[17] "**Auger recombination in low-band-gap n-type InGaAs**", *W. K. Metzger, M. W. Wanlass, R. J. Ellingson, R. K. Ahrenkiel, and J. J. Carapella, Appl. Phys. Lett. 79 (2001), 3272-3274.*

[18] "**InP-based materials and devices: physics and technology**", *O. Wada, and H. Hasegawa, (John Wiley & Sons, USA, 1999).*

[19] "**Direct measurement of the carrier leakage in an InGaAsP/InP laser"**, *T. R. Chen, S. Margalit, U. Koren, K. L. Yu, L. C. Chiu, A. Hasson, and A. Yariv, Appl. Phys. Lett. 42 (1983), 1000-1002.*

[20] "**Direct Measurement of the carrier leakage out of the active region in InGaAsP/InP laser heterostructures"**, *G. L. Belenky, R. F. Kazarinov, J. Lopata, S. Luryi, T. Tanbun-Elk, and P. A. Garbinski, IEEE Trans. Electron Dev. 42 (1995), 215-218.*

[21] "**Effect of p-doping profile on performance of strained multi-quantum-well InGaAsP-InP lasers"**, *G. L. Belenky, C. L. Reynolds, R. F. Kazarinov, V. Swaminathan, S. L. Luryi, and J. Lopata, IEEE J. Quantum Electron. 32 (1996), 1450-1455.*

[22] "**Analysis and application of theoretical gain curves to the design of multi-quantum-well lasers**", *P. W. A. McIlroy, A. Kurobe, and Y. Uematsu, IEEE J. Quantum Electron. 12 (1985), 1958-1963.*

[23] "**Depenance of the light-current characteristics of 1.55-µm broad-area lasers on different p-doping profiles**", *I. K. Han, S. H. Cho, P. J. S. Heim, D. H. Woo, S. H. Song, F. G. Johnson, and M. Dagenais, IEEE Photon. Technol. Lett. 12 (2000), 251-253.*

[24] "**Effect of heterobarrier leakage on the performance of high-power 1.5 µm InGaAsP multiple-quantum-well laser"**, *L. Shterengas, R. Menna, W. Trussell, D. Donetsky, G. Belenky, J. Connolly, D. Garbuzov, J. Appl. Phys. 88 (2000), 2211-2214.*

[25] **"Effect of p-doping profile on performance of strained InGaAs/InGaAsP multiple quantum well buried heterostructures laser diodes with Fe- or p/n/p-doped InP current blocking layer",** *H. S. Kim, D. K. Oh, I. H. Choi, Mat. Sci. Eng. B 77 (2000), 202-206.*

[26] "**Temperature Performance of 1.3-µm InGaAsP-InP lasers with different profile of p-doping"**, *G. L. Belenky, D. V. Donetsky, C. L. Reynolds, R. F. Kazarinov, G. E. Shtengel, S. L. Luryi, and J. Lopata, IEEE Photon. Technol. Lett. 9 (1997), 1558-1560.*

[27] **"Concentration dependent Zn diffusion in InP during metalorganic vapor phase epitaxy",** *S. N. G. Chu, R. A. Logan, M. Geva, N. T. Ha, J. Appl. Phys. 78 (1995), 3001-3007.*

[28] **"Zinc doping in InP grown by atmospheric pressure metalorganic vapor phase epitaxy",** *A. Molassioti, F. Scholz, Y. Gao, J. Cryst. Growth 102 (1990), 974-978.*

Chapter 5

Hole Injection in Broad-Waveguide Laser

5.1 Introduction

The broad-waveguide laser concept has proven to be a very successful approach for high power operation. It reduces the internal losses of the laser significantly which is essential for high power operation. However as shown in the previous chapter hole injection becomes an issue in this type of lasers due to thick undoped waveguiding layer. It can negate the positive effect of the reduced optical loss and reduce the maximum output power of the laser.

This chapter investigates the effect of the active region position in the waveguide. To avoid confusion between the carrier transport and optical confinement factor effects, in this study they were separated by designing structures with similar confinement factors but different hole injection conditions. The performance of laser structures with various active region positions in simulations and real devices will be presented and compared.

5.2 Hole injection

Usually the active region of a laser diode is placed in the middle of the waveguide, which is an acceptable practice for producing simple devices. However, to produce state-of-the-art lasers precise design of all laser parameters including the position of active region in the waveguide is required. This might be less obvious for thin waveguide lasers (transverse waveguide thickness of the order of few hundred nanometers) but in the design of broad-waveguide lasers (transverse waveguide thickness exceeding one micrometer), the position of the active region can dramatically affect the performance of the device.

Changing the position of active region in the waveguide changes a number of laser parameters. The most obvious effect is the change of the optical mode confinement factor. Displacing the active region to either side from the middle of the waveguide will reduce the active region optical confinement factor. This leads to reduced modal gain with the most obvious manifestation of increased threshold current (assuming it still satisfies the laser threshold condition). On the other hand reduced optical confinement factor leads to a reduction of free carrier absorption in the active region, increase of catastrophic optical damage energy density [1], and laser gain-saturation as will be shown in the following chapter. There are also numerous reports of significantly increased output power from laser structures with reduced optical confinement [1-6].

Another parameter influenced by the active region position is the active region carrier injection. As shown in ref. [7-9] optimised carrier injection can similarly lead to improved laser performance, resulting in confusion between the effects of carrier injection and optical confinement factor.

Carrier transport can significantly affect the properties of semiconductor lasers. A lot of attention has been paid to carrier transport affecting the modulation characteristics of laser diodes [7-9]. Those reports clearly indicate the importance of carrier transport, hole injection in particular, for high-speed laser operation, reporting a strong dependence of the laser performance on the thickness of the waveguide layer between the p-cladding and the active region. Special attention was drawn to the fact that ambipolar transport approximation (which uses a single averaged value for mobility for both electrons and holes) should not be applied to lasers with thick waveguide layers due to very significant difference in electron and hole transport time.

Despite the abovementioned no studies of carrier transport effect on the performance of high power lasers or broad-waveguide lasers could be found. Some studies deal with carrier transport in term of thermionic heterobarrier leakage and p-clad doping level [10,11]. Even though other studies clearly indicate significant increase in maximum output power and slope efficiency from laser structures with the p-doping front approaching the active region [12,13], they fail to link it to improved hole injection. This is especially obvious in study reported in [13], where the doping level was identical in two structures but the doping fronts were at different distances to the active region.

There is a paper highlighting the importance of hole injection, by reporting nonuniform and preferential localisation of injected carriers in the quantum well closest to the p-cladding layer in multi quantum well structures [14] due to the lower mobility of holes, which preferentially occupy the closest QW and then electrostatically attract more electrons into the QW.

In some studies [2-4] the displacement of the active region towards the p-cladding is governed by the requirement of low optical confinement factor or mode selection and is completely unrelated to carrier transport design parameters. However no justification is provided for the displacement towards the p-cladding and not the n-cladding region.

5.3 Numerical Modelling

In this chapter the influence of the active region position on laser performance is investigated. In order to isolate the influence of optical confinement factor and carrier injection, three laser structures were grown and investigated:

- one symmetrical structure with the active region positioned in the middle of the waveguide layer;
- two structures with the active regions displaced, one towards the p-cladding and another towards the n-cladding layer.

Both structures with the displaced active regions yield the same optical confinement factor (based on 1D analysis) since the active region displacements are symmetrical relatively to the middle of the waveguide layer. This isolates the effect of carrier injection in the two structures with displaced active regions.

As a starting point for determining the optimum position of the active region a set of well-known formulae for minority carrier injection was used:

$$p(x) = p_{N0}(e^{qV_f/k_BT} - 1)e^{-x/L_h} \tag{5.1}$$

$$n(x) = n_{P0}(e^{qV_f/k_BT} - 1)e^{-x/L_e} \tag{5.2}$$

where $p(x)$, $n(x)$ are the injected carrier density, p_{N0}, n_{P0} the equilibrium minority carrier density, q the electron charge, V_f applied bias, k_B Boltzmann constant, T temperature, x the coordinate, and L_h, L_e carrier (hole and electron) diffusion length.

For initial simulation purposes we considered a 1 μm thick InGaAsP nominally undoped waveguide layer as lightly p-doped for electron injection calculation and lightly n-doped for hole injection calculation. Using diffusion length values of L_e = 3 μm, L_h = 0.5 μm [15], and the value of applied forward bias corresponding to the typical InP based laser operation condition, the typical concentration distributions of injected electrons and holes in the waveguide layer were calculated and the results are shown in Fig. 5.1. The abscissa represents the position in the waveguide layer, where holes are injected from the right (x > 3000 nm) and electrons from the left (x < 2000 nm). Needless to say that an equal number of electrons and holes are required for optimum laser performance and as shown in this figure, the curves intersect at around 2800 nm, which is

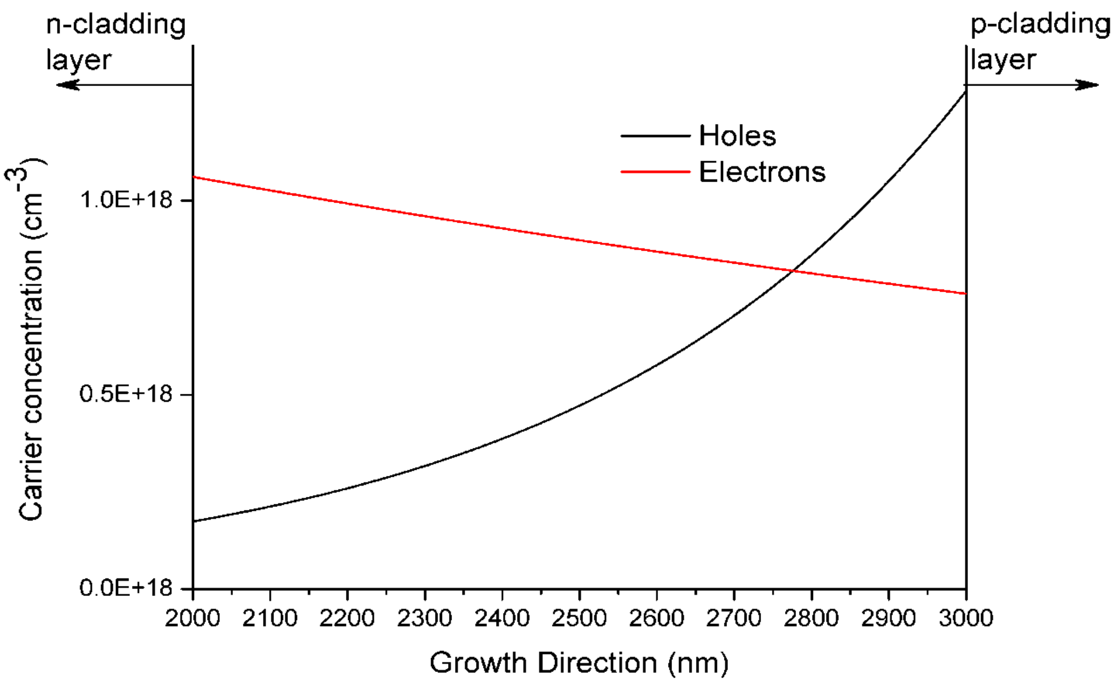

Fig. 5.1 Calculated typical injection profile of electrons and holes into 1000 nm InGaAsP waveguide layer.

300 nm away from the middle of the waveguide. Hence a value of 300 nm displacement was chosen for this study.

For numerical modelling a commercially available software package LaserMOD from RSOFT [16] was used.

Detailed descriptions of the structures used in this study are presented in Tab. 5.1. With the exception of the number of quantum wells (one quantum well was used in the simulations) the real structures were replicating the simulated structures as closely as possible.

The confinement factors for the structures were determined to be 0.69% for the undisplaced active region (from now onwards will be referred to as 000), 0.50% for the structure displaced towards the p-cladding (referred to as +300) and 0.54% for the structure displaced towards the n-cladding (referred to as -300). The small difference in confinement factors of the (+300) and (-300) samples are due to ridge waveguide formation on top of the structure which pushes the mode slightly towards the substrate,

Material	Doping (cm^{-3})	Layer thickness (µm)	Bulk bandgap (eV)	Structural function
$In_{0.53}Ga_{0.47}As$	Zn $1x10^{19}$	0.05	0.74	Contact layer
InP	Zn $2x10^{18}$	1.5	1.35	p-cladding
InP	no	0.5	1.35	
$In_{0.86}Ga_{0.14}As_{0.30}P_{0.70}$	no	X	1.13	Waveguide
$In_{0.79}Ga_{0.21}As_{0.45}P_{0.55}$	no	0.02	1.03	Active region
$In_{0.6}Ga_{0.4}As$	no	0.005	0.67	
$In_{0.79}Ga_{0.21}As_{0.45}P_{0.55}$	no	0.01	1.03	
$In_{0.6}Ga_{0.4}As$	no	0.005	0.67	
$In_{0.79}Ga_{0.21}As_{0.45}P_{0.55}$	no	0.01	1.03	
$In_{0.6}Ga_{0.4}As$	no	0.005	0.67	
$In_{0.79}Ga_{0.21}As_{0.45}P_{0.55}$	no	0.01	1.03	
$In_{0.6}Ga_{0.4}As$	no	0.005	0.67	
$In_{0.79}Ga_{0.21}As_{0.45}P_{0.55}$	no	0.01	1.03	
$In_{0.6}Ga_{0.4}As$	no	0.005	0.67	
$In_{0.79}Ga_{0.21}As_{0.45}P_{0.55}$	no	0.02	1.03	
$In_{0.86}Ga_{0.14}As_{0.30}P_{0.70}$	no	1-X	1.13	Waveguide
InP	Si $2x10^{18}$	0.1	1.35	n-cladding
InP	Si $2x10^{18}$	0.2	1.35	
Substrate	S $2x10^{18}$	-//-	1.35	

Table 5.1 Detailed description of the laser structures. X values are 0.2, 0.5 and 0.8 µm for structures (+300), (000) and (-300) respectively.

resulting in marginally higher overlap with active region of the (-300) structure. The difference is very small and not expected to affect the results significantly.

Considering only the confinement factor, the performance of the (+300) and (-300) structures should be almost identical, with their threshold current higher than that of the (000) structure, but less roll-over and as a result higher maximum output power [2]. However, as seen in Fig. 5.2, which depicts the results of numerical modelling of the light-current (L-I) curves, the performance of the (-300) structure is significantly degraded compared to other samples, while the (+300) structure showed the best performance. The inset in Fig. 5.2 is the magnified image of the threshold region of the L-I curves, which illustrates the expected increase of threshold current with the decrease of the confinement factor. It is evident that other parameters rather than confinement factor have to be considered to explain the obtained results.

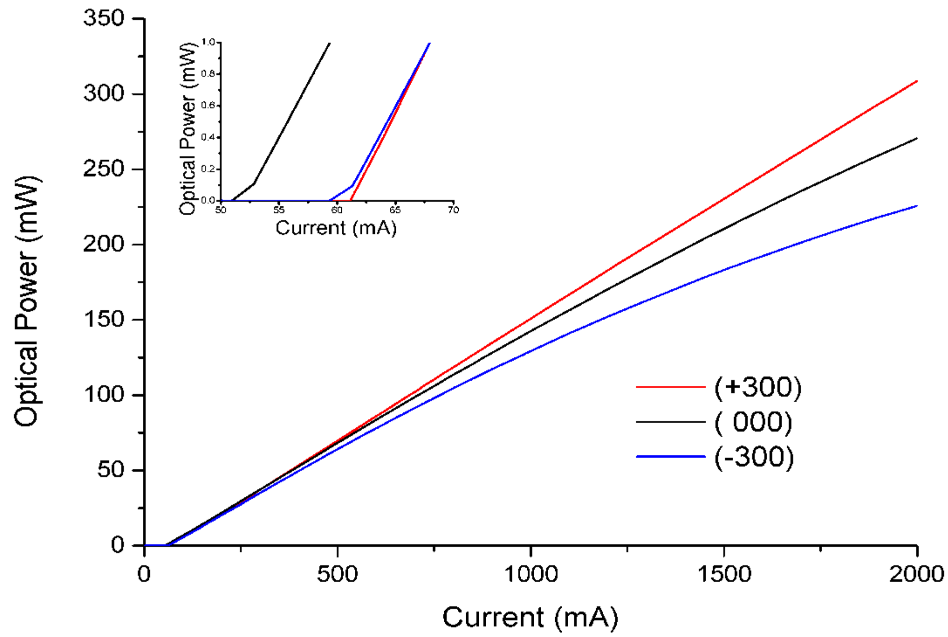

Fig. 5.2 Simulated light-current curves of the structures with different active region positions. The inset shows the enlarged threshold region.

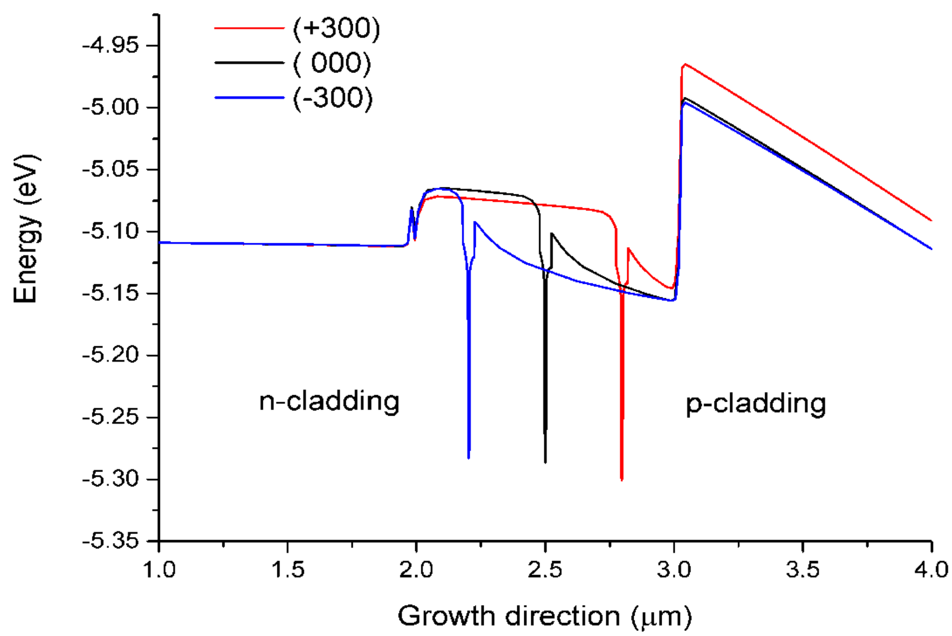

Fig. 5.3 Simulated conduction band diagram of the three different structures under identical injection conditions.

The operation of III-V semiconductor devices is usually based on bandgap engineering, therefore the bandstructure has to be studied to explain the differences in laser performance. In Fig. 5.3, the numerically modelled conduction band diagrams of the structures under identical high injection are shown. The structure with the active region displaced towards the p-cladding (+300) appears to be the least deformed, while the (000) and (-300) structures are much more deformed, being 28 meV and 32 meV lower than that of the (+300) structure, respectively.

The potential barrier for electrons consists of conduction band discontinuity between the waveguide and the p-cladding layers, and the built-in potential. The different amount of deformation can be explained with the guide of Fig. 5.4 which shows the hole quasi-Fermi levels for the three structures. The built-in potential is reduced by the applied voltage, which is equal to the hole quasi-Fermi level separation and depletion region voltage drop [5].

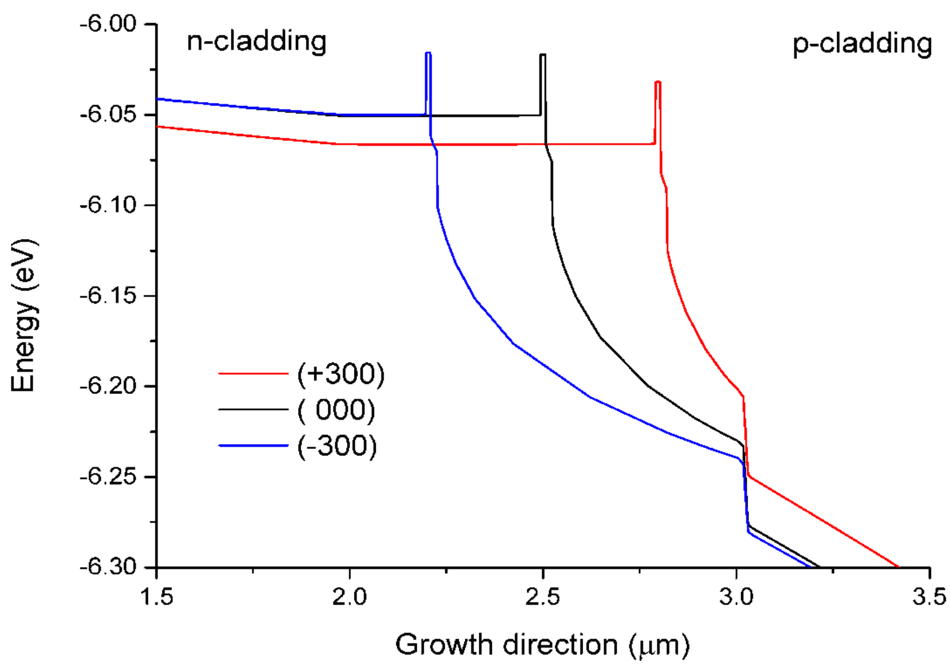

Fig. 5.4 Simulated hole quasi-Fermi levels of the three structures under identical injection.

Efficient hole injection in the (+300) structure provides enough holes in the active region for electrons to recombine with, while in the (000) and (-300) structures the number of holes in the quantum well is significantly lower, requiring higher bias to provide the same hole injection level. This leads to a lower number of electrons recombining in the quantum well and therefore, excess electrons spill over and accumulate at the waveguide – p-cladding interface. This excessive number of electrons deforms the band structure as seen in Fig. 5.3 by increasing the hole quasi-Fermi level separation, leading to the reduction of the potential barrier at the p-cladding layer and therefore increases electron thermionic leakage current.

Reduction of the potential barrier explains better performance of the (+300) structure. However the (-300) structure does not have significantly lower barrier height compared to the (000) structure, due to almost complete reduction of the built-in potential. To explain the inferior performance of the (-300) structure as compared to the (000) structure

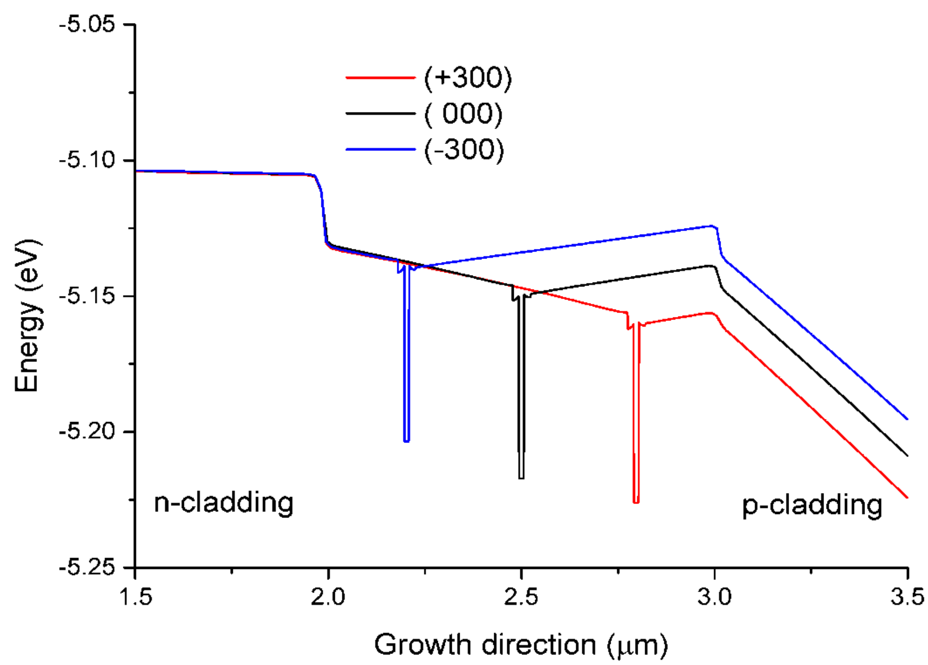

Fig. 5.5 Simulated electron quasi-Fermi levels of the studied structures under identical injection level.

we have to compare their electron quasi-Fermi levels. As shown in Fig. 5.5 electron quasi-Fermi level of the (-300) structure is 14 meV higher compared to the (000) structure in the vicinity of the waveguide – p-cladding interface, resulting in higher number of electrons capable of overcoming the barrier. As a result of both of these effects the electron thermionic leakage current across the waveguide – p-cladding interface is the lowest in the (+300) structure, increases in the (000) structure and is the highest in the (-300) structure as can be seen in the inset of Fig. 5.6. It is the electron thermionic leakage that leads to an increased L-I roll-over in the (000) structure and even more so in the (-300) structure, as observed in Fig. 5.2.

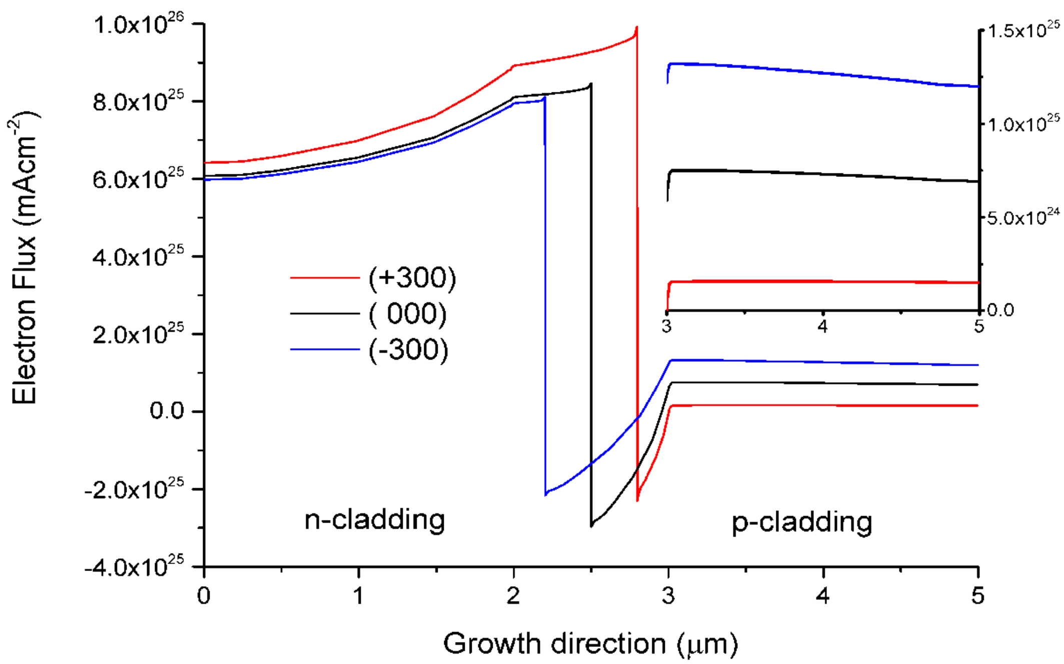

Fig. 5.6 Simulated electron flux of the studied structures. The inset shows the blowup of the p-cladding region of the structure.

5.4 Experimental results

The laser structures were grown as described in Chapter 3 (Fabrication Issues). In the first structure the active region is displaced by 300 nm from the middle of the waveguide layer towards the p-cladding (+300), in the second structure the active region is positioned in the middle of the waveguide layer (000) and in the third structure the active region is displaced by 300 nm from the middle towards the n-cladding (-300).

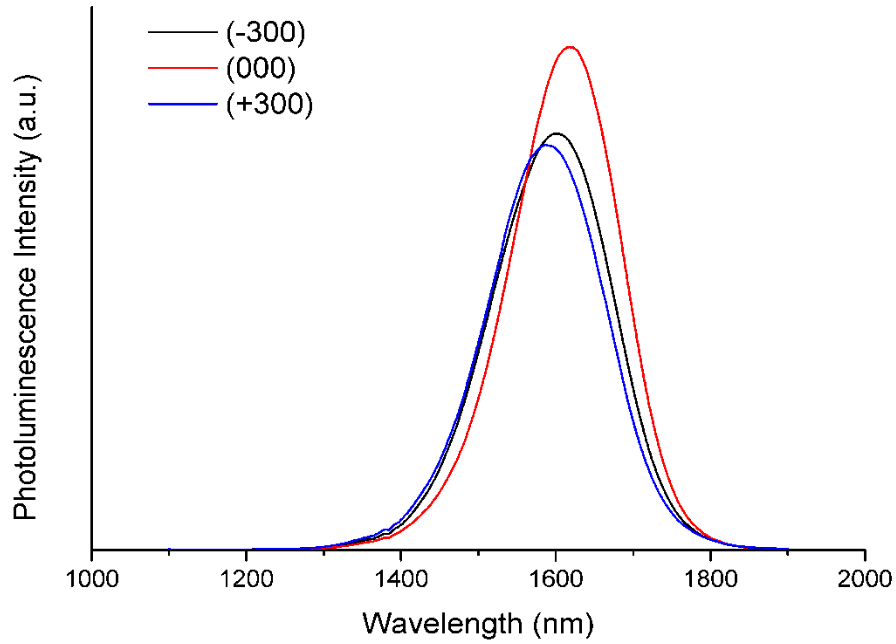

Fig. 5.7 Photoluminescence spectra of the grown structures (p-doped InGaAs and InP selectively etched off).

To evaluate the quality of the grown structures the PL spectra of the structures were measured and compared, as illustrated in Fig. 5.7. Before PL measurement the highly doped top contact and p-cladding layers were selectively etched off. The PL spectra for the (-300) and (+300) structures are almost identical while that of the undisplaced structure has a slightly higher peak intensity.

The structures were processed simultaneously following the same laser fabrication procedure, as described in Chapter 3 (Fabrication Issues). The samples were cleaved into separate devices of 1, 1.5, 2 and 3 mm long for testing as described in Chapter 2 (Experimental Techniques). Testing was carried out at a constant temperature of 10 ^{o}C. To avoid device heating the lasers were tested under pulsed condition (1% duty cycle and pulse duration of 100 ns). The light output was collected from a single facet and measured with an integrating power meter.

Figure 5.8 illustrate the typical L-I curves of 3 mm long devices of the three structures. As can be seen from the figure the (+300) structure has the steepest slope even

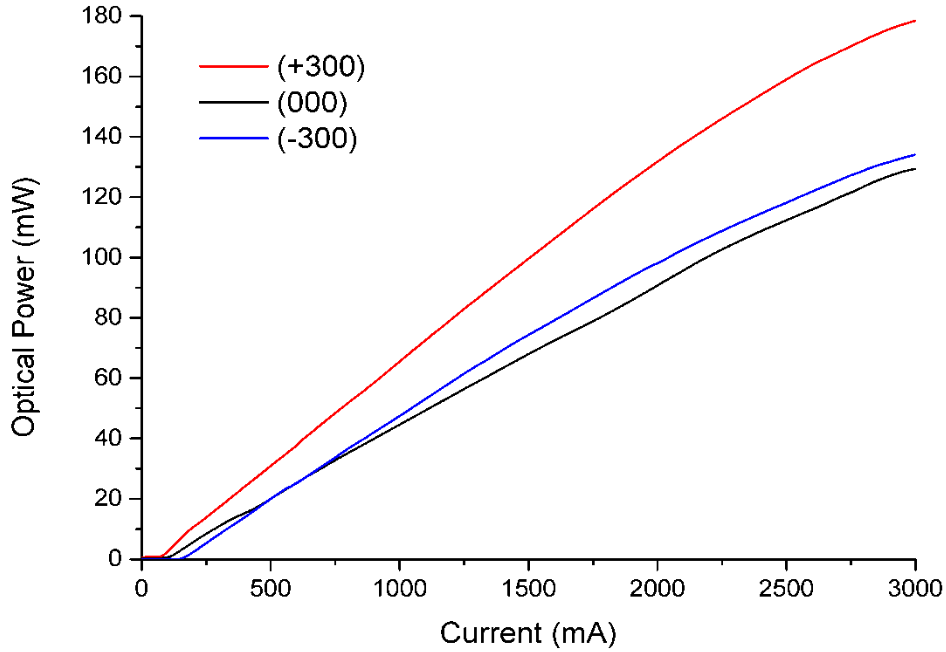

Fig. 5.8 Typical L-I curves of 3 mm long devices of the studied structures.

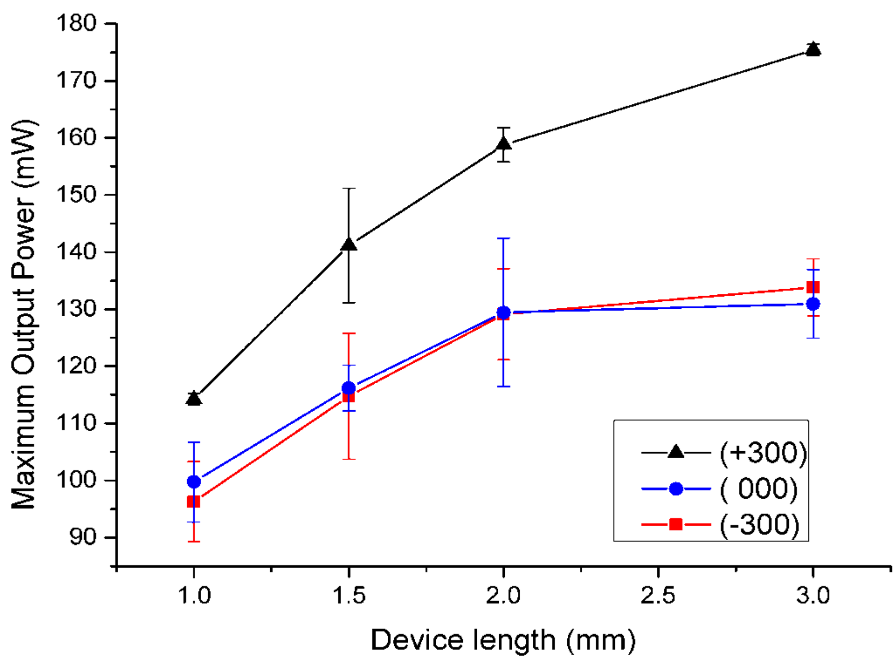

Fig. 5.9 Averaged measured maximum output power from different device length and different structures. (Lines are a guide to the eye).

at low injection while the (000) and (-300) structures have comparable slopes. Unlike the numerical modelling the experimental results show the lowest threshold was produced by the (+300) structure. The average values (multiple devices for every device length of each structure were tested) of maximum output powers for different device lengths of the three structures are shown in Fig. 5.9. As expected the (+300) structure outperformed the other structures, with a clear trend of increasing margin with increasing device length, up to 25% for 3 mm long devices.

Illustrated in Fig. 5.10 are the dependence of inverse external differential quantum efficiency of the structures on the laser cavity length and their respective internal differential quantum efficiency and internal optical loss (data fitting is done according to the procedure described in Chapter 2). The internal differential quantum efficiency (which characterises the active region performance) and the internal optical loss (which characterises the waveguide) of the three structures are almost identical. This indicates an absence of any material or structural characteristics other than active region position

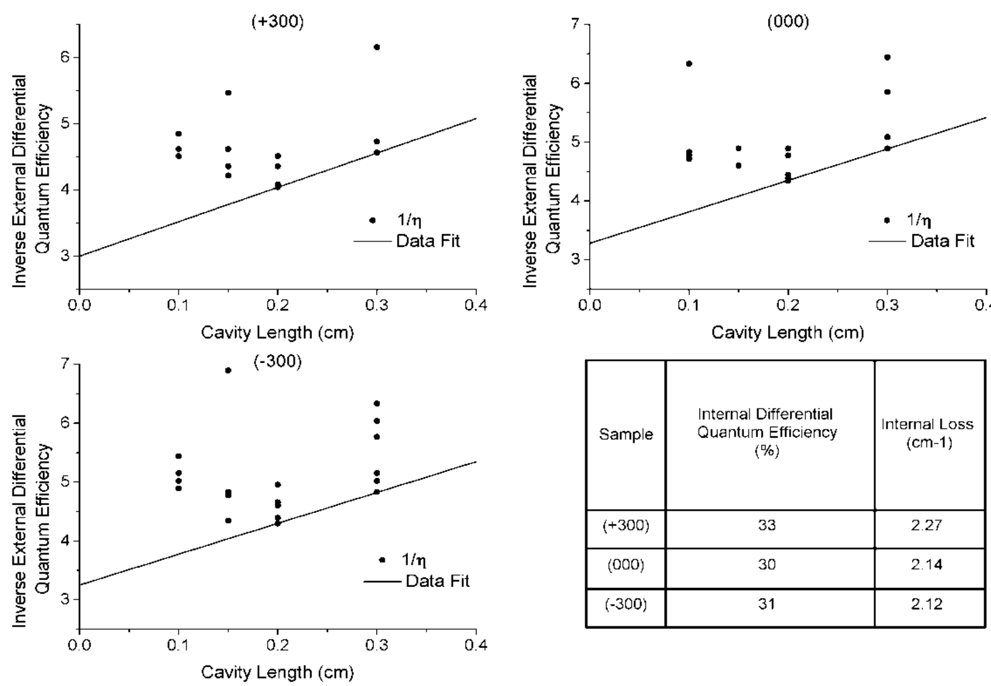

Sample	Internal Differential Quantum Efficiency (%)	Internal Loss (cm-1)
(+300)	33	2.27
(000)	30	2.14
(-300)	31	2.12

Fig. 5.10 Dependence of inverse external differential quantum efficiency of the three structures on the laser cavity length and their respective internal differential quantum efficiency and internal optical loss.

which is responsible for the significant change in laser performance.

Comparing the performance of the (+300) and (-300) structures clearly shows that the improvement in laser performance is due to improved hole injection in the (+300) structure and not merely due to the reduced optical confinement which is almost identical in both structures. This unquestionably proves the importance of carrier injection in broad-waveguide lasers, especially hole injection and the advantage of positioning the active region closer to the p-cladding region for improved hole injection.

However, the experimental results shown in Fig. 5.9 agree with the modeled results only for 1 and 1.5 mm long devices, where the averaged maximum output power values of the (000) sample falling between those of the (-300) and (+300) samples. For 2 mm long device the average maximum output power values of samples (000) and (-300) overlap and for 3 mm long device the average maximum output power values of (000) sample become lower than that of (-300) sample. This can be explained by the sublinear dependence of gain on the injection current. Hence there is an optimum device length for a certain modal gain provided by the active region [17]. Since the confinement factor for the (000) structure is the highest its optimum device length is significantly shorter than that of the (-300) and (+300) structures [18]. Therefore the higher maximum output power of (-300) structure over the (000) structure from long devices is the result of lower confinement factor. The same argument is applicable to explaining the increasing gap between the performance of the (+300) and (-300) structures with increasing device length, since the confinement factor of the (+300) structure is slightly lower than that of the (-300).

5.5 Conclusions

A comparative study of three laser structures with the active region located in different positions in the waveguide was conducted. The structures were 1 μm broad-waveguide laser structures, with the reference structure (000) undisplaced (active region in the middle of the waveguide) while the other two structures have their active region displaced by 300 nm from the center towards n-cladding (-300) or p-cladding (+300) layer. All the structures showed very similar internal differential quantum efficiency and the internal optical loss, indicating no material quality difference or structural differences other than the active region position which could result in different laser performance. The two displaced structures have almost identical confinement factors and by comparing their performance the effect of carrier injection from the effect of reduced confinement factor could be isolated.

The (+300) structure showed less roll-over and produced significantly higher average maximum output power, up to 25% for 3 mm long devices, compared to other structures. This illustrates the importance of carrier injection and active region position in broad-waveguide laser diodes and clearly proves that the improvement in laser performance depends strongly on hole injection and not merely due to reduced optical confinement.

References

[1] **"High power CW output from low confinement asymmetric structure diode laser,"** *G. Iordache, M. Buda, G. A. Acket, T. G. van de Roer, L. M. F. Kaufmann, F. Karouta, C. Jagadish and H.H. Tan, Electron. Lett. 35 (1999), 148-149.*

[2] "**Slab-coupled 1.3-μm semiconductor laser with single-spatial large-diameter mode"**, *J. N. Walpole, J. P. Donnelly, P. J. Taylor, L. J. Missaggia, C. T. Harris, R. J. Bailey, A. Napoleone, S. H. Groves, S. R. Chinn, R. Huang, and J. Plant, IEEE Photon. Technol. Lett. 14 (2002), 756-758.*

[3] **"1.5-μm InGaAsP-InP slab-coupled optical waveguide lasers,"** *J. J. Plant, P. W. Juodawlkis, R. K. Huang, J. P. Donnelly, L. J. Missaggia, K. G. Ray, IEEE Photon. Technol. Lett. 17 (2005), 735-737.*

[4] **"16W continuous-wave output power from 100 μm-aperture laser with quantum well asymmetric heterostructure,"** *N. A. Pikhtin, S. O. Slipchenko, Z. N. Sokolova, A. L. Stankevich, D. A. Vinokurov, I. S. Tarasov, and Zh. I. Alferov, Electron. Lett. 40 (2004), 1413 – 1414.*

[5] **"8 W continuous wave front-facet power from broad-waveguide Al-free 980 nm diode lasers,"** *L. J. Mawst, A. Bhattacharya, J. Lopez, D. Botez, D. Z. Garbuzov, L. DeMarco, J. C. Connolly, M. Jansen, F. Fang, R. F. Nabiev, Appl. Phys. Lett. 69 (1996), 1532-1534.*

[6] **"1.5 μm wavelength, SCH-MQW InGaAsP/InP broadened-waveguide laser diodes with low internal loss and high output power,"** *D. Garbuzov, L. Xu, S. R. Forest, R. Menna, R. Martinelli, and J. C. Connolly, Electron. Lett. 32 (1996), 1717-1719.*

[7] "**Carrier transport effects in quantum well lasers: an overview**", *R. Nagarajan, Opt. Quant. Electron*. 26 *(1994), S647-S666.*

[8] "**A time-domain model for high-speed quantum-well lasers including carrier transport effects"**, *L. V. T. Nguyen, A. J. Lowery, P. C. R. Gurney, and D. Novak, IEEE J. Sel. Top. Quant. Electron. 1 (1995), 494-504.*

[9] "**High speed quantum-well lasers and carrier transport effects"**, *R. Nagarajan, M. Ishikawa, T. Fukushima, R. S. Geels, and J. E. Bowers, IEEE J. Quantum Electron. 28 (1992), 1990-2008.*

[10] "**Drift leakage current in AlGaInP quantum-well lasers"**, *D. P. Bour, D. W. Treat, R. L. Thornton, R. S. Geels, and D. F. Welch, IEEE J. Quantum Electron. 29 (1993), 1337-1343.*

[11] "**Carrier transport in laser heterostructures"**, *R. F. Kazarinov, and M. R. Pinto, IEEE J. Quantum Electron. 30 (1994), 49-53.*

[12] "**Dependence of the light-current characteristics of 1.55-µm broad-area lasers on different p-doping profiles**", *I. K. Han, S. H. Cho, P. J. S. Heim, D. H. Woo, S. H. Song, F. G. Johnson, and M. Dagenais, Photon. Technol. Lett. 12 (2000), 251-253.*

[13] **"Effect of p-doping profile on performance of strained InGaAs/InGaAsP multiple quantum well buried heterostructures laser diodes with Fe- or p/n/p-doped InP current blocking layer",** *H. S. Kim, D. K. Oh, I. H. Choi, Mat. Sci. Eng. B 77 (2000), 202-206.*

[14] **"Evidence of nonuniform carrier distribution in multiple quantum well lasers,"** *H. Yamazaki, A. Tomita, M. Yamaguchi, and Y. Sasaki, Appl. Phys. Lett. 71 (1997), 767-769.*

[15] **"Minority carrier diffusion lengths in liquid phase epitaxial InGaAsP and InGaAs,"** *M. M. Tashima, L. W. Cook,G. E. Stillman, J. Electron. Mater. 11 (1982),* 831-846.

[16] **"LaserMOD user guide,"** *RSOFT Design Group, Inc.*

[17] **"Analysis and application of theoretical gain curves to the design of multi-quantum-well lasers,"** *P. W. A. McIlroy, A. Kurobe, and Y. Uematsu, IEEE J. Quantum Electron. 21 (1985), 1958-1963.*

[18] **"Fabrication of short GaAs wet-etched mirror lasers and their complex spectral behavior,"** *F. Karouta, E. Smalbrugge, W. C. van der Vleuten, S. Gaillard, and G. A. Acket, IEEE J. Quantum Electron. 34 (1998), 1474-1479.*

Chapter 6

Merged Beam Laser (MBL)

6.1 Introduction

There are a number of different approaches for increasing the output power of semiconductor lasers. All of them have their advantages and disadvantages which will be briefly discussed in this chapter. The absence of a single dominating approach illustrates the complexity of the issue and the struggle for increased laser output power.

In this chapter Merged Beam Laser (MBL) design will be presented. The operation principle, advantages and the most important design parameters of MBL will be discussed. Finally the performance of the MBLs will be presented and compared with standard ridge waveguide lasers.

6.2 High Power Lasers and Y-Coupling

A lot of effort has been devoted to increasing the power output of semiconductor lasers, resulting in a number of different methods.

The simplest method of increasing light output from a chip is the laser array. Practical requirement for single lobe output led to the development of evanescently coupled arrays [1] and leaky-wave coupled arrays [2]. However the evanescently coupled arrays provide only partial coupling, resulting in multiple peak output, while the leaky-wave coupled arrays are extremely sensitive to intraelement optical distance, resulting in unstable single lobe output.

Another popular approach of increasing the laser output power is the wide aperture laser [3]. This approach increases the width of the ridge waveguide from 3 – 4 μm for standard single mode laser to 100 – 200 μm. The advantage of this approach is the simplicity of device fabrication but the output is multimode, making its application limited.

Tapered waveguide laser [4] is the approach that tries to combine the advantages of standard single mode laser and wide aperture lasers. Tapered region provides high gain, while the single mode region should discriminate higher order modes. However higher order mode suppression is insufficient in simple waveguide and requires additional implantation or etching of trenches next to the ridge, which makes the fabrication process much more complicated.

Broad-waveguide laser [5] is the approach that has attracted a lot of attention lately. By increasing the thickness of the waveguiding layers (transverse direction), the optical mode penetration into the adjacent highly doped regions in broad-waveguide laser is significantly reduced. As free carrier absorption in highly doped layers is one of the main contributors to optical losses in semiconductor lasers [5,6]. Reducing the interaction of the optical field with doped regions leads to reduced optical loss in the cavity and as a result higher net gain and higher output power. In this case the limiting factor for the thickness of the waveguiding layer is the onset of higher order modes. Advantages of this method are the simple fabrication process and single mode operation.

The best results in output power so far have been obtained by slab-coupled optical waveguide lasers (SCOWLs) [7]. SCOWL is the improvement of the broad-waveguide design and based on Marcatili's coupled-mode analysis [8]. It shows that higher order modes in a large multimode waveguide can be coupled into the slab leaving only the fundamental mode in the waveguide. This approach allows the fabrication of even larger cavities than those of broad-waveguide lasers and yet maintains fundamental mode operation. Extension of the laser cavity in the transverse direction results in significantly reduced optical losses due to reduced mode interaction with the highly doped regions of the device. At the same time, increased laser cavity width results in higher modal gain as a result of the increased effective volume of the optical mode.

Broad-waveguide lasers and slab-coupled optical waveguide lasers are capable of producing output beam quality required for efficient coupling to a single mode optical fiber without additional optical elements unlike other types of lasers.

Nevertheless these types of lasers also have their limitations. The two main mechanisms limiting the output power of these InP-based lasers are gain-saturation and two-photon absorption. Both of these processes have the same origin and are proportional to the photon concentration in the laser cavity. Therefore the approach for gain-saturation reduction presented in this work will also be effective in reducing two-photon absorption.

Two-photon absorption is a nonlinear effect, which depends on square of the optical field intensity. It can be expressed as:

$$-\frac{dP}{dz} = \beta P_0^2 \tag{6.1}$$

where β is the two-photon absorption coefficient, z is the optical field propagation direction, P is the optical field intensity and P_0 is the initial intensity (at z = 0). Two-photon absorption becomes significant only at very high optical field intensity. On the other hand gain-saturation affects all gain media regardless of optical field intensity.

The gain of a laser medium taking into account the gain-saturation process can be expressed as:

$$g = \frac{g_0}{1 + \frac{P}{P_{sat}}} \tag{6.2}$$

where g is the gain coefficient, g_o is the gain coefficient in absence of an optical field, P is the optical field intensity, P_{sat} is the saturation intensity (saturation intensity is the optical field intensity at which gain is reduced by a factor of two). Since the coefficients g_o and P_{sat} are constants for a given device structure, the only option to reduce the gain-saturation for a given laser structure is to reduce the optical field intensity P in the active region.

Proposed in this work merged beam laser (MBL) is designed to utilize the reduction of the optical field intensity in laser cavity to increase the laser output. It consists of two single mode waveguides connected by Y-couplers. The MBL design achieves the reduction of the optical field intensity by doubling the cross-sectional area of the optical mode while always maintaining single mode operation, unlike wide aperture lasers and tapered waveguide laser. Figure 6.1 shows simulated gain curves as a function of optical

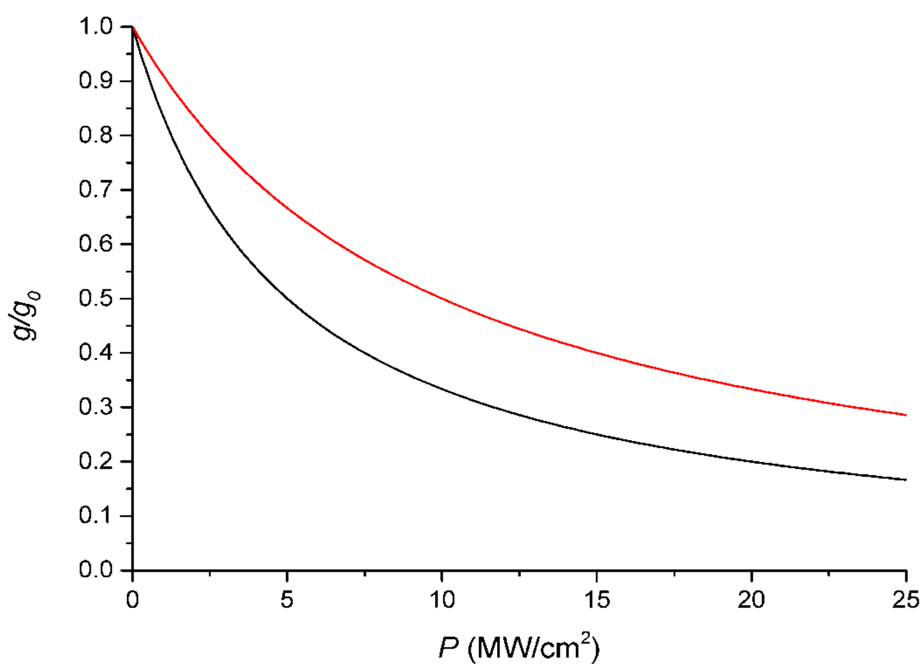

Fig. 6.1 Gain-saturation (g/g_o) as a function of electromagnetic field intensity (P) of a standard ridge waveguide laser (black) and a laser with doubled cross-section area of the mode (red).

intensity (Eq. 6.2) for a standard ridge waveguide laser and a laser with twice the cross-sectional area of the mode, such as the MBL. In both cases the gain drops monotonically with increasing optical intensity. However, this effect is significantly reduced in case of the laser with twice the mode area.

Two important remarks about MBL have to be made.

First, merged beam laser (MBL) is a set of parallel single mode waveguides coupled at each end by a Y-coupler. The set of waveguides provides increased modal area, hence reduces the modal gain drop due to gain-saturation. Unlike tapered waveguide laser all the waveguide branches of MBL are single mode. Therefore, there is no need for higher order mode discrimination schemes which results in a straightforward fabrication process.

Secondly, Y-couplers ensure that the same mode propagates in all of the waveguides. Unlike coupled lasers, there is only one set of mirrors that forms the optical resonator in MBL and the mode has to satisfy the threshold condition in all of the waveguide branches. Therefore the mode is not coupled modes, but the same mode that propagates in all the waveguide branches of the device.

6.3 Numerical Modelling

For numerical modelling commercially available software package BeamPROP [9] from RSOFT was used. BeamPROP is a general numerical modelling package for computing electromagnetic field propagation in arbitrary waveguides. This package is based on finite difference beam propagation method (BPM), which is the most widely used technique for modeling field propagation in integrated and fiber-optic photonic devices [9]. We used BeamPROP to simulate one directional propagation of the optical field through the MBL waveguide structure, since one of the limitations of BPM is its inability to deal with reflections, which makes it impossible to simulate laser resonators.

Figure 6.2 illustrates the numerical modelling results of optical field propagation in the MBL cavity. Optical mode launched at point (0,0) splits evenly at the first Y-junction, propagates through the branches and then merges together at the other Y-junction, resulting in mode intensity at the end point (0,3000) of near unity. Dark blue ripples outside the waveguide represent the electromagnetic field losses. From numerical modelling it is obvious that both Y-junctions can introduce additional optical losses.

Optical mode encounters this additional loss on each pass of the waveguide, hence it is very important in this type of device to minimise the optical loss at the Y-junction.

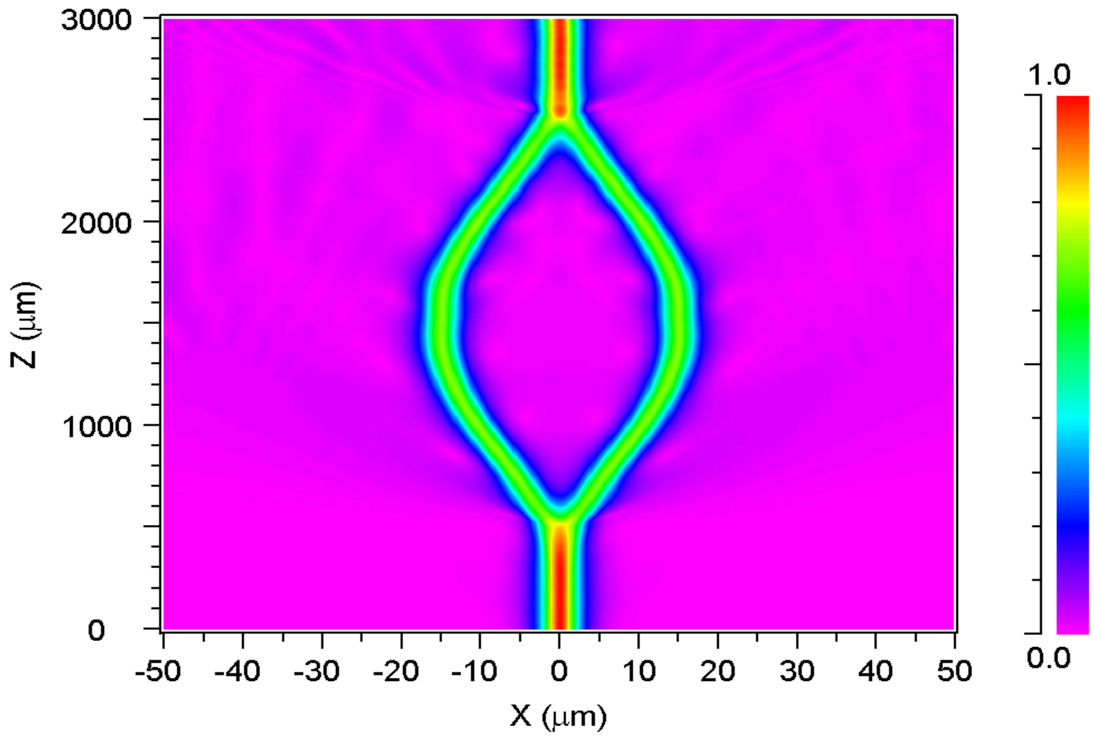

Fig. 6.2 Colour-coded result of BeamPROP (RSoft) numerical modelling of the electromagnetic field propagation in MBL. The mode launched at the beginning (0,0) of the waveguide splits evenly at the first Y-junction and then merges at the other Y-junction. At the end (0,3000) of the waveguide the mode intensity nearly reaches unity.

The losses arising from the electromagnetic field passing through the Y-junction are the result of electromagnetic field escaping from the waveguides. Hence, all the numerical modellings are performed with the aim of reducing field escape. The factors significantly influencing the confinement of the field are following:

(1) curvature radius of the Y-junction or equivalently the distance between two waveguides,

(2) refractive index of the insulating material (SiN_x) covering the waveguide,

(3) the waveguide height or the etch depth.

To determine the optimum values of these parameters, three sets of inter-dependent numerical modelling were performed. A priori limit for optical losses introduced by the Y-couplers (additional loss) in the structure was set to 5%, which for this cavity translates into a loss equivalent to about 0.1 cm^{-1}. The optical field transmission from one facet of the MBL to the other facet was then numerically calculated. The results are illustrated in Fig. 6.3 – 6.5, for the three different factors, respectively.

From Fig. 6.3 transmission of the electromagnetic field through the MBL waveguide

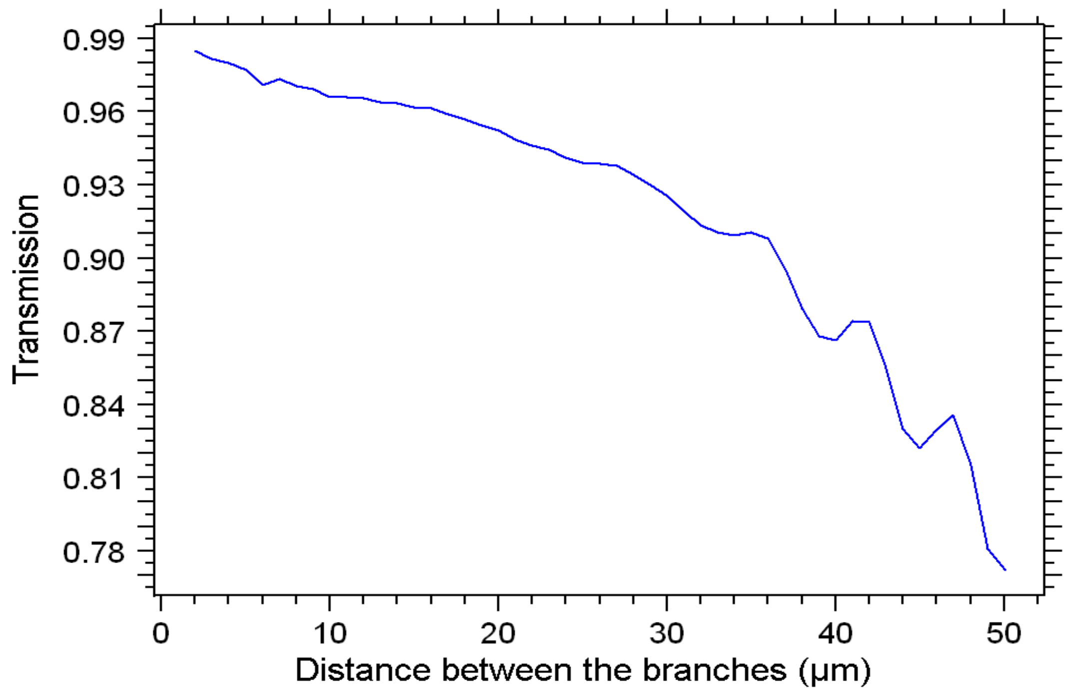

Fig. 6.3 Dependence of electromagnetic field transmission through MBL waveguide as a function of the distance between the branches (BeamPROP numerical modelling).

gradually decreases with distance between the branches up to about 20 μm. Beyond this value there is a much faster drop. For the distance between the branches of 50 μm, only ~ 77% of the light is transmitted. The oscillating behaviour of the curve observed between values 30 μm – 50 μm is due to reduced confinement and more pronounced interference from the leaky field. Hence as long as the distance between the waveguides is maintained below 20 μm (Y-junction radius longer than 25 mm) the optical propagation losses will be less than 5%.

Similarly numerical modelling was done for the dependence of field transmission through the structure as function of the insulating material refractive index. For the numerical modelling of the effect of insulating layer refractive index, we used the refractive index values of SiN_x ranging from 1.6 to 2.1, values that are regularly obtained in our PECVD system by changing the deposition conditions. The results in Fig. 6.4 show that as long as the refractive index of the SiN_x layer is above 1.7 transmission of 95% or higher can be obtained. Below this value, there is a sudden drop in the transmission across the MBL waveguide.

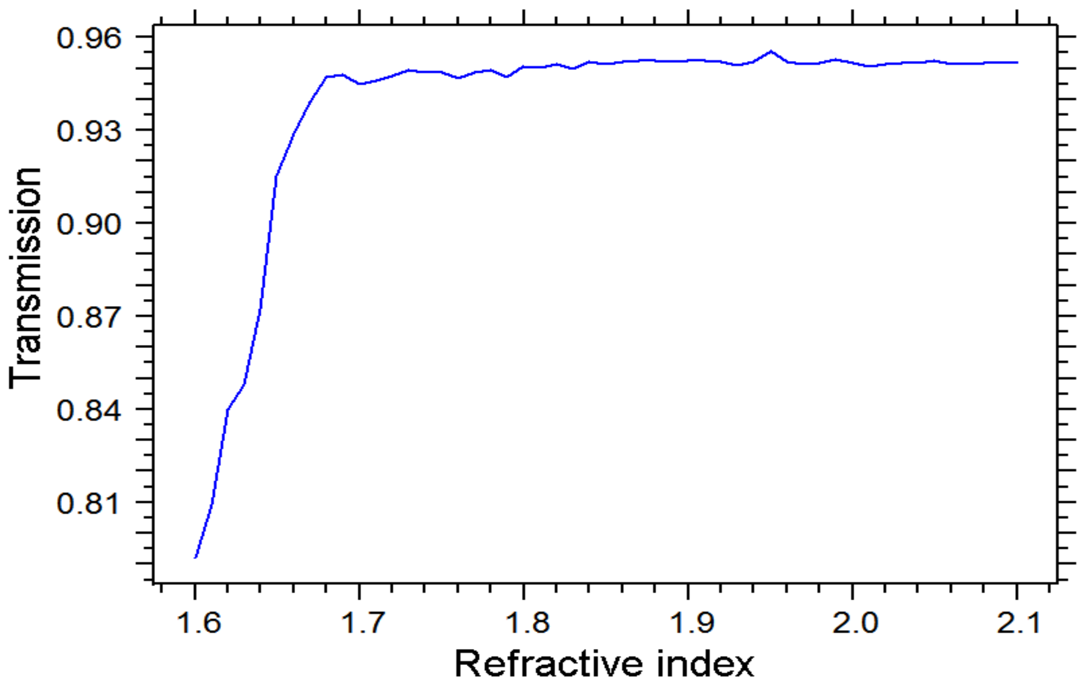

Fig. 6.4 Dependence of electromagnetic field transmission through the MBL as a function of the SiN_x insulating layer refractive index. (BeamPROP numerical modelling).

The precise control of etch depth during the ridge waveguide formation is even more important as illustrated in Fig. 6.5. There is a window around the etch depth of 1.9 µm in which 95 % optical transmission is achievable. Too shallow an etch (less than 1.86 µm) results in reduced lateral confinement of the mode and increased field leakage from the waveguide at the Y-junctions, and as a result increased transmission losses. On the other hand, etching too deep into the waveguide layer (more than 2.0 µm) results in additional losses from more pronounced field interaction with the etched surface.

Obviously high transmission losses at the Y-junctions would negate the benefits of reduced gain-saturation and should therefore be avoided.

From numerical modelling for a laser 3 mm long the following optimised parameters were determined: laser ridge width 3 µm, the distance between the waveguides 15 µm

(Y-junction curvature radius of 67 mm), refractive index of 1.88 for the SiN_x insulating layer and the etch depth of 1.9 μm (0.1 μm above the waveguide layer).

Using these optimised parameters, very low additional transmission losses in the MBLs can be obtained, as shown in Fig. 6.2. The electromagnetic field introduced into

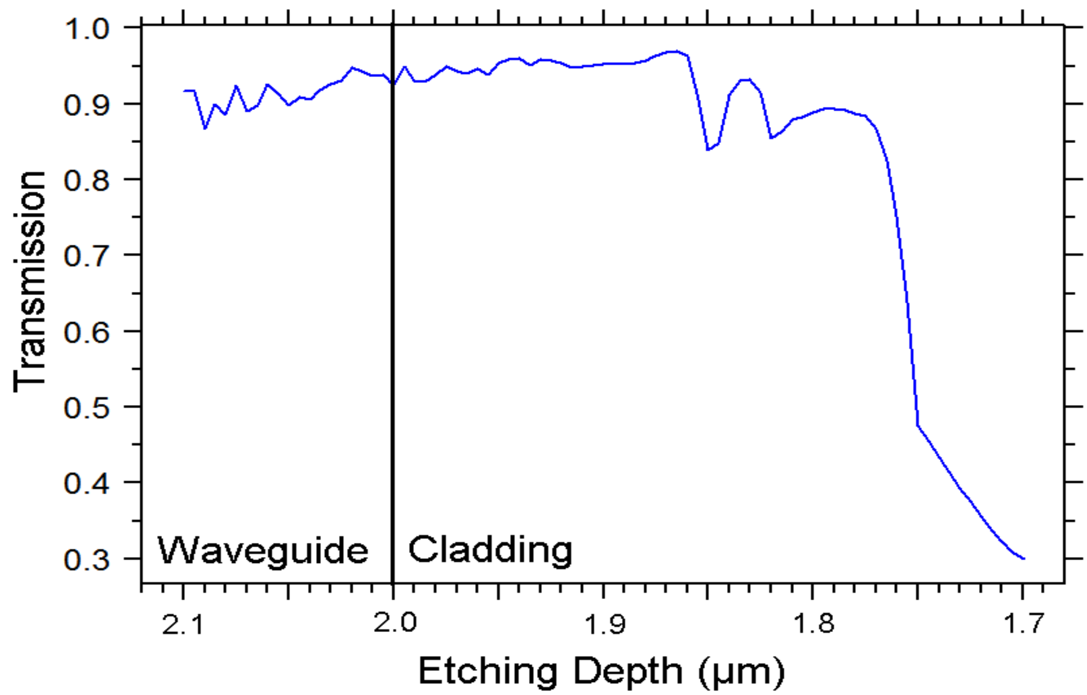

Fig. 6.5 Dependence of electromagnetic field transmission through the MBL as a function of ridge etch depth. (BeamPROP numerical modelling).Vertical bar represents the cladding and the waveguide layer interface.

the waveguide at point (0,0), splits evenly, passes through the waveguides, recombines and emerges at the exit point (0,3000) with losses of less than 5%.

6.4 Experimental Results

Both MBLs and conventional ridge waveguide lasers were fabricated on the same broad-waveguide laser structure (Chapter 4). The laser structure was grown and processed as described in Chapter 3 (Fabrication Issues). The samples were cleaved into separate devices of 3 mm long (designed length of the MBL) for testing as described in

Chapter 2 (Experimental Techniques). Device testing was carried out at a constant temperature of 10 ^{o}C. To avoid device heating the lasers were tested under pulsed condition (1% duty cycle and pulse duration of 100 ns). The light output was collected from a single facet and measured with an integrating power meter.

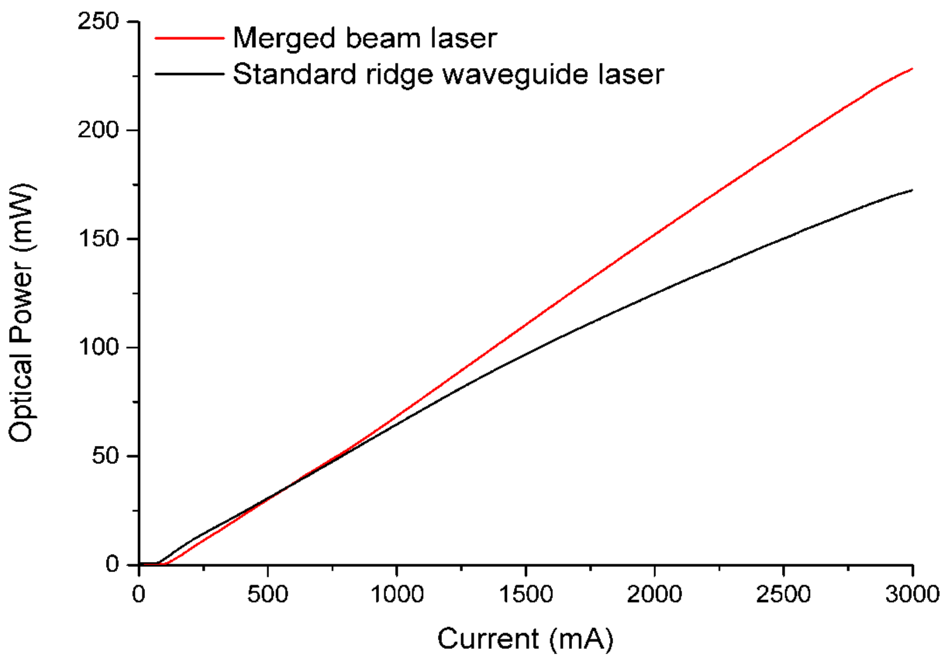

Fig. 6.6 Light – current (L-I) curves of MBL (red curve) and standard ridge waveguide laser (black curve). The output light was collected from a single facet. The devices' facets are "as-cleaved".

The light versus current (L-I) curves of both type of devices are shown in Fig. 6.6. Both curves do not have any "kinks", implying that they operate in a single mode up to injection current of 3000 mA (limited by the current source).

The L-I curve of the MBL is nearly perfectly straight line in contrast to the standard ridge waveguide laser which has a noticeable rollover at higher current. Since the testing of both devices was carried out under the same conditions, on a temperature controlled stage and at very short current pulses of 100 ns with 1% duty cycle, the effect of thermal heating was negligible. Hence the L-I curve rollover of the standard ridge waveguide laser can only be the result of the more severe effect of material gain-saturation.

Additional losses introduced by the Y-junctions lead to a slight increase of the threshold current value in the MBL. However the reduction of gain-saturation in MBL results in a power output of 228.5 mW at 3000 mA (limited by the current source), which is 30% higher than the power output of 172.6 mW from conventional ridge waveguide laser at the same injection current.

As shown in Fig. 6.1 doubling of the cross-sectional area of the mode results in a significant reduction of gain-saturation. This reduction of gain-saturation in MBL can be clearly seen in the slope efficiency as a function of output power as shown in Fig. 6.7. The slope efficiency of a laser is the slope of L-I curve and represents the rate of output power increase with injected current. Hence higher gain results in higher slope efficiency. In Fig. 6.7, the slope efficiency of the standard ridge waveguide laser is initially higher, however it drops quickly with the increase of the output power, while that of the MBL is almost constant over the entire range of measurement. The sharp drop of both curves at high output power is due to instabilities of the current source at the end of the range.

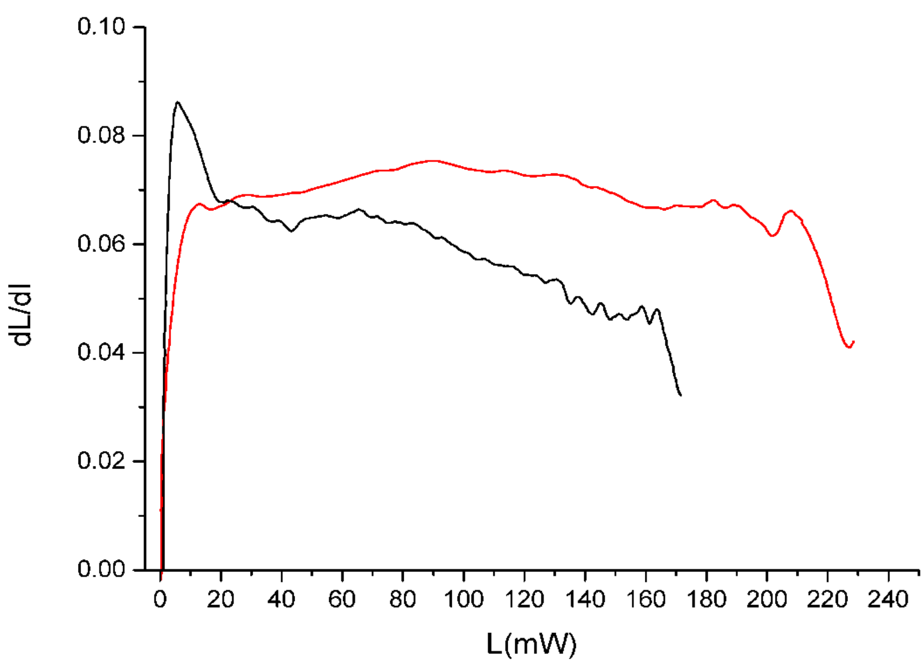

Fig. 6.7 Slope efficiency vs. output power for the MBL (red curve) and standard ridge waveguide laser (black curve). The sharp drop at the end of the curves is due to instabilities of the current source and happened for all devices tested.

Since the objective of this study is to produce an increased power output from a single mode laser, near-field and far-field studies of the MBL laser were carried out to determine the mode profile. For the near-field study a confocal microscope was employed to increase the optical resolution for this wavelength. Only a single lobe is visible in the near-field image of the MBL shown in Fig. 6.8.

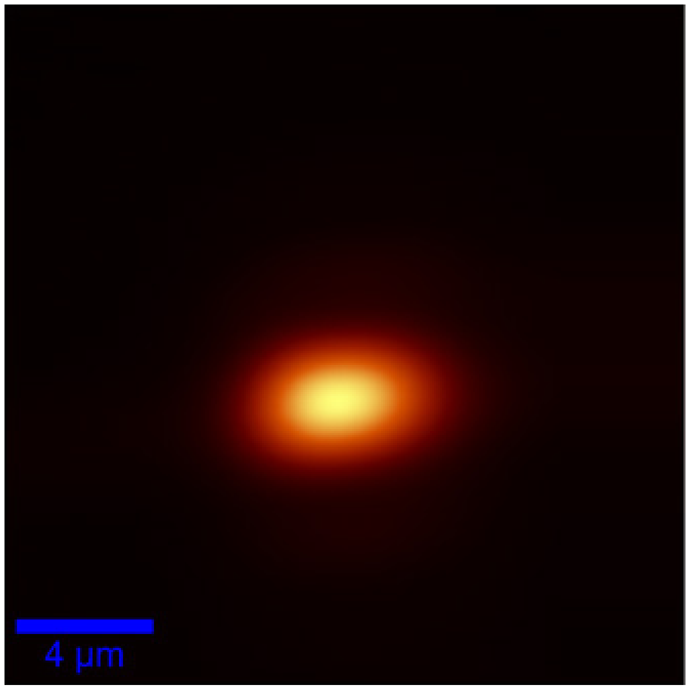

Fig. 6.8 Near-field image of the MBL (CW operation at three time the threshold current).

For the far-field study a scanning-slit method was used. It uses a narrow slit to scan across the optical field, by measuring the transmitted optical power the beam profile can then be reconstructed. Beam divergence for the slow axes of 16.9^o was derived for MBL, whereas a value of 16.7^o was obtained for the standard single mode ridge waveguide laser. Single lobe near-field, together with beam divergence value close to the value for the standard single mode ridge waveguide laser and a "kink"-free L-I curve are obvious indicators of a single spatial mode operation of the MBL.

As for the spectral characteristics, laser resonator formed by cleaving is a form of Fabry-Perot interferometer, with a set of Fabry-Perot modes supported by the geometry of the resonator. Overlap of Fabry-Perot modes with material gain spectrum determines the set of spectral modes supported by a given laser. Usually semiconductor lasers produce multimode spectrum, unless special measures are undertaken like distributed feedback (DFB), distributed Bragg reflector (DBR) or coupled cavity resonators. An example of multimode spectrum produced by the standard ridge waveguide laser is shown in Fig. 6.9. The spectral amplitude distribution of the modes is quite random.

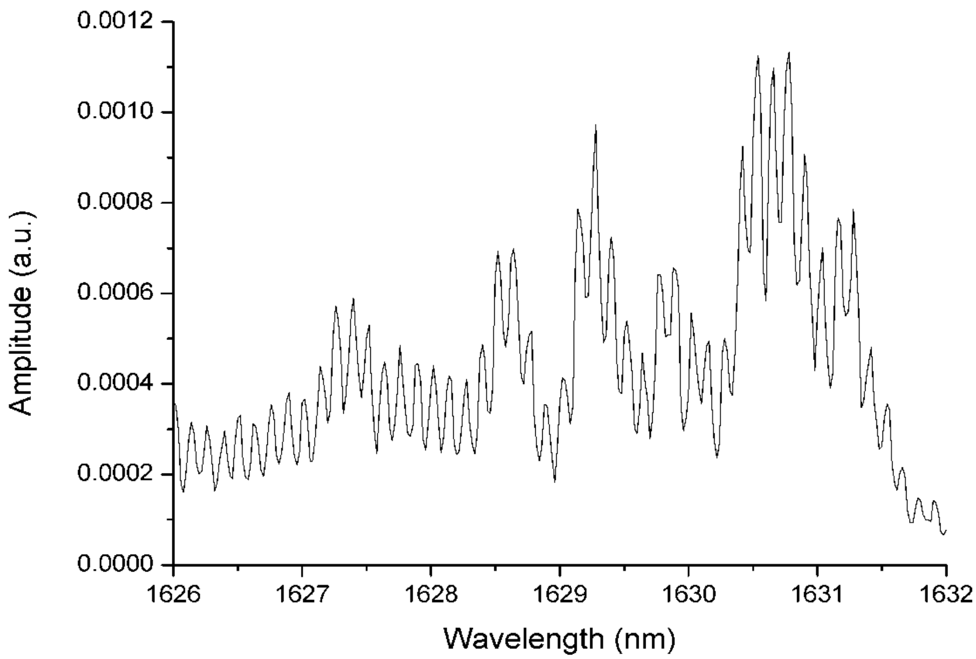

Fig. 6.9 Spectrum of the standard ridge waveguide laser at an injection current of 1000 mA (CW operation).

On the other hand the modal spectrum of the MBL laser has a strongly dominating mode, as illustrated in Fig. 6.10 at 1000 mA injection current (CW operation). A strong domination of one spectral mode is the inherent characteristic of MBL cavity due to joining of two waveguide branches by Y-couplers inside a Fabry-Perot optical resonator. In an MBL device the spectral modes are the result of the convolution of two sets of Fabry-Perot modes from two waveguides that form the MBL cavity with the gain spectrum. Due to a small difference in the path length of each waveguide (as a result of fabrication imperfection), only a few overlapping modes exist. This results in a dominating mode in the vicinity of gain curve maximum. It is worth mentioning that optimisation has not been performed to increase spectral mode selectivity of these MBLs and both branches were designed to be of the same geometry. For true single spectral mode operation with sufficient side mode suppression the branches should be designed so

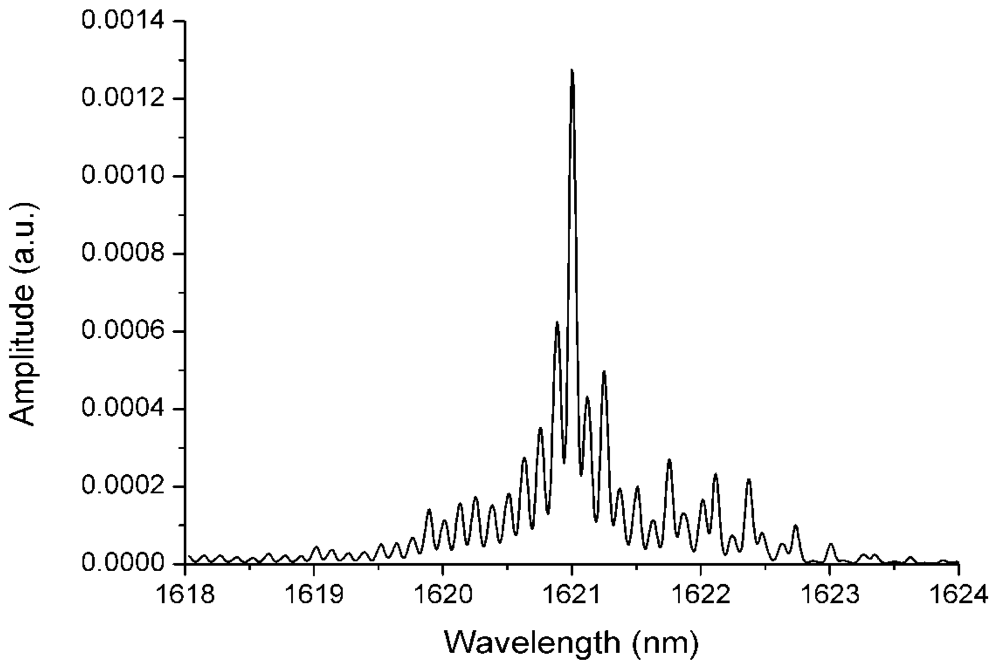

Fig. 6.10 Spectrum of the MBL at an injection current of 1000 mA (CW operation).

that the optical lengths of both branches are significantly different.

Even though the branches were designed to be of the same length and the side mode suppression is due to fabrication imperfections, the effect was expected since Fabry-Perot resonator is extremely sensitive to the optical length. It has been shown previously that by injecting current separately into different parts of this type of device spectral mode control can be achieved [10].

6.5 Conclusions

The results from merged beam lasers (MBLs) were presented and compared with those of standard ridge waveguide lasers. This type of laser cavity is capable of increasing the output power of a single mode laser by reducing the optical field intensity in the cavity, hence reducing the gain saturation of the active medium. The comparative study between the two types of lasers shows that 30% higher output power can be produced by the MBL. Since the mechanisms of gain-saturation and two-photon absorption are strongly dependent on the optical field intensity in the laser cavity, this type of laser cavity can also be used to reduce two-photon absorption.

The study clearly shows that MBL is operating in a single spatial mode regime. Additionally due to its distinctive cavity a single spectral mode is clearly dominating in the spectrum of the MBL.

It is very important in this laser cavity design to reduce the additional losses introduced by the Y-junctions. By carefully designing and optimising parameters like the radius of the Y-junctions, insulating material refractive index and waveguide height, additional losses introduced by the Y-junctions can be limited to less than 5% or equivalently to less than 0.1 cm^{-1} for our MBL cavity.

This design can be extended to lasers with higher number of branches. Our numerical modelling of light propagation through a four branch MBL indicate that transmission losses of less than 5% can be achieved. This opens up the path for a further increase of output power.

References

[1] "**High-power, 8 W cw, single-quantum-well laser diode array**", *D. F. Welch, B. Chan, W. Streifer, and D. R. Scifres, Electron. Lett. 24(2), (1988), 113-115 .*

[2] "**Resonant leaky-wave coupling in linear arrays of antiguides**", *D. Botez, L. J. Mawst, and G. Peterson, Electron. Lett. 24, (1988), 1328-1330 .*

[3] "**High-power (>10 W) continuous-wave operation from 100-µm-aperture 0.97-µm-emitting Al-free diode lasers**", *A. Al-Muhanna, L. J. Mawst, D. Botez, D. Z. Garbuzov, and R. U. Martinelli, Appl. Phys. Lett. 73, (1998), 1182-1184 .*

[4] "**High-power, high-brightness semiconductor tapered diode lasers for the red and near infrared spectral range**", *B. Sumpf, H. Wenzel, and G. Erbert, Proc. of SPIE 7616, (2010), 76161L-(1-11).*

[5] "**1.5 µm wavelength, SCH-MQW InGaAsP/InP broadened-waveguide laser diodes with low internal loss and high output power**", *D. Garbuzov, L. Xu, S. R. Forest, R. Menna, R. Martinelli, and J. C. Connolly, Electron. Lett. 32, (1996), 1717-1719.*

[6] "**Free-carrier effects on optical properties**", *S. Adachi, in Physical Properties of III-V Semiconductor Compounds: InP, InAs, GaAs, GaP, InGaAs, and InGaAsP, (John Wiley & Sons, USA, 1992).*

[7] "**1.5-µm InGaAsP-InP slab-coupled optical waveguide lasers**", *J. J. Plant, P. W. Juodawlkis, R. K. Huang, J. P. Donnelly, L. J. Missaggia, and K. G. Ray, Photon. Techn. Lett. 17(4), (2005), 735-737.*

[8] "**Slab-coupled waveguides**", *E. A. J. Marcatili, http://www.alcatel-lucent.com/bstj/vol53-1974/articles/bstj53-4-645.pdf*

[9] "**BeamPROP user guide**", *RSOFT Design Group, Inc.*

[10] "**Multifunctional photonic switching operation of 1500 nm Y-coupled cavity laser (YCCL) with 28 nm tuning capability**", *M. Schilling, W. Idler, D. Baums, G. Laube, K. Wunstel, and O. Hildebrand, Photon. Technol. Lett. 3, (1991), 1054-1057.*

Chapter 7
Summary and Recommendation for Future Research

This work concentrated on various methods of increasing light output from telecom wavelength InP-based single spatial mode lasers.

The broad-waveguide approach for increasing laser output power was presented in chapter 4. The concept behind the increased output power from lasers with broad-waveguide design is based on reduction of the internal optical losses due to reduced optical field interaction with highly doped regions (especially the p-doping). Indeed the broad-waveguide lasers in conjunction with the optimised Zn doping (as discussed in chapter 3) produced very low optical loss of 2.3 cm^{-1}. For this work the waveguide layer was selected to be 1 μm thick, even though when considering only the single mode operation criterion the thickness of the waveguide layer can be increased to about 2 μm, which would reduce the internal optical loss even further. However for the study of hole injection efficiency (chapter 5) waveguide thickness cannot exceed 1 μm in the structure with displaced active region to avoid appearance of higher order modes. Hence for the purpose of comparative study of structures with displaced active regions and a symmetric structure the waveguide thickness is set to 1 μm in all of the structures.

However, as shown in chapter 4, while simple increase of the waveguide thickness while reducing the internal optical loss will not result in increased output power, due to decreased efficiency of the hole injection. Two possible methods for increasing hole injection efficiency are: doping the waveguide layer between the p-cladding and the active region or moving the active region from the middle of the waveguide towards the p-cladding.

The former method is in contradiction to the principle of the broad-waveguide laser design, which lowers the optical loss by reducing the overlap between the mode and the doped region.

The later method, on the other hand, is much more suitable for incorporation into broad-waveguide laser design. This approach was studied in chapter 5. By comparing the performance of two structures with similar optical confinement factors but different hole injection conditions the effect of improved hole injection could be decoupled from reduced optical confinement and investigated. As expected the improved hole injection significantly increased the laser output power by up to 25%. Even though the optimal position of the active region was determined by numerical modelling, further fine tweaking of the active region position might still provide some increase of the laser output power.

Doping optimisation conducted in this work produced highly doped p-cladding region, required for blocking of thermionic leakage current, while producing minimal Zn diffusion into adjacent waveguide layer, required for minimization of optical loss. Doping value ($2.6\text{x}10^{18}$ cm^{-3}) close to the saturation value of Zn doping in MOCVD grown InP was achieved in the p-cladding, while Zn concentration in the waveguide layer drops rapidly to $2\text{x}10^{16}$ cm^{-3} within 150 nm indicating very low diffusion.

Some improvement to the laser output power may be obtained by employing Be as a p-dopant instead of Zn. Due to lower diffusion of Be in InP, reducing the p-dopant "tail" in the waveguide would result in lower internal optical loss. Another expected benefit of using Be, which would lead to increased laser output power is the reduction of the thermionic leakage current due to higher obtainable doping level.

Structures with 5 QWs active region were used in this work to provide gain safety net against any unexpected additional losses caused by material or fabrication imperfections, especially during Merged Beam Laser (MBL) fabrication, presented in chapter 6.

However, as mentioned in chapter 4 the optimum number of quantum wells in the active region is one. Hence using the structure with single quantum well active region and optimising the length of the laser diode according to the quantum well number would allow to further increase the laser output power.

The above-mentioned optimisations are expected to improve the maximum output power of MBL as well as standard ridge waveguide laser.

Compared to abovementioned, MBL is a more complex method of increasing output power from a single spatial mode laser. This method is based on reducing gain saturation by decreasing the optical field intensity in the laser waveguide through waveguide branching. A two-branch MBL was designed, fabricated and compared with a standard ridge waveguide laser. The results showed that MBL has less rollover and as result ~30% higher output power than the standard ridge waveguide laser. Output power of 229 mW at 3000 mA (limited by the current source) was obtained from a single facet of the MBL without any facet coating. Near-field and far-field study of the MBL indicate single spatial mode operation. Moreover due to unique cavity design of MBL a strong domination of a single spectral mode was observed.

Specifically for MBLs a few more steps to further improve the performance can be employed. For instance the number of the branches can be increased. As mentioned in chapter 6, a four-branch MBL with low transmission losses (~5%) was successfully numerically modelled. This suggests that four and more branch MBLs can be fabricated to further increase their output power.

In chapter 6 the spectral characteristic of MBL shows a strong domination of a single spectral mode. This is due to the effect of tiny length difference between the two branches as a result of fabrication imperfections. The spectral modes of MBLs are the result of the convolution of two sets of Fabry-Perot modes with the material gain spectrum. Hence, by intentionally designing the two branches of the MBL to be of different lengths their Fabry-Perot mode sets can be made to differ significantly which would result in sufficient side mode suppression for single frequency operation. Additionally by fabricating separate contacts on the MBL and separately controlling the injection into different parts of the device its operational frequency can be controlled and tuned, making the MBL the simplest tunable single frequency laser, in terms of the device fabrication aspect.

List of amendments.

Section 1.2 “Motivation”. A paragraph was added at the end of the section (page 5).

- This work focuses on studying the broad-waveguide laser concept, its advantages, disadvantages and the methods of improving its power output. To evaluate broad-waveguide lasers their performance is compared with the performance of standard thin waveguide lasers. Based on the evaluation two methods of improving broad-waveguide laser performance has been proposed both resulting in increased output power. Method for improved hole injection resulted in increased laser output power by up to 25%. While Merged Beam Laser design increased laser output power by 30%.

Section 3.2 “Laser Diode Fabrication Flowchart”. Figure 3.1 Fabrication steps were numbered.

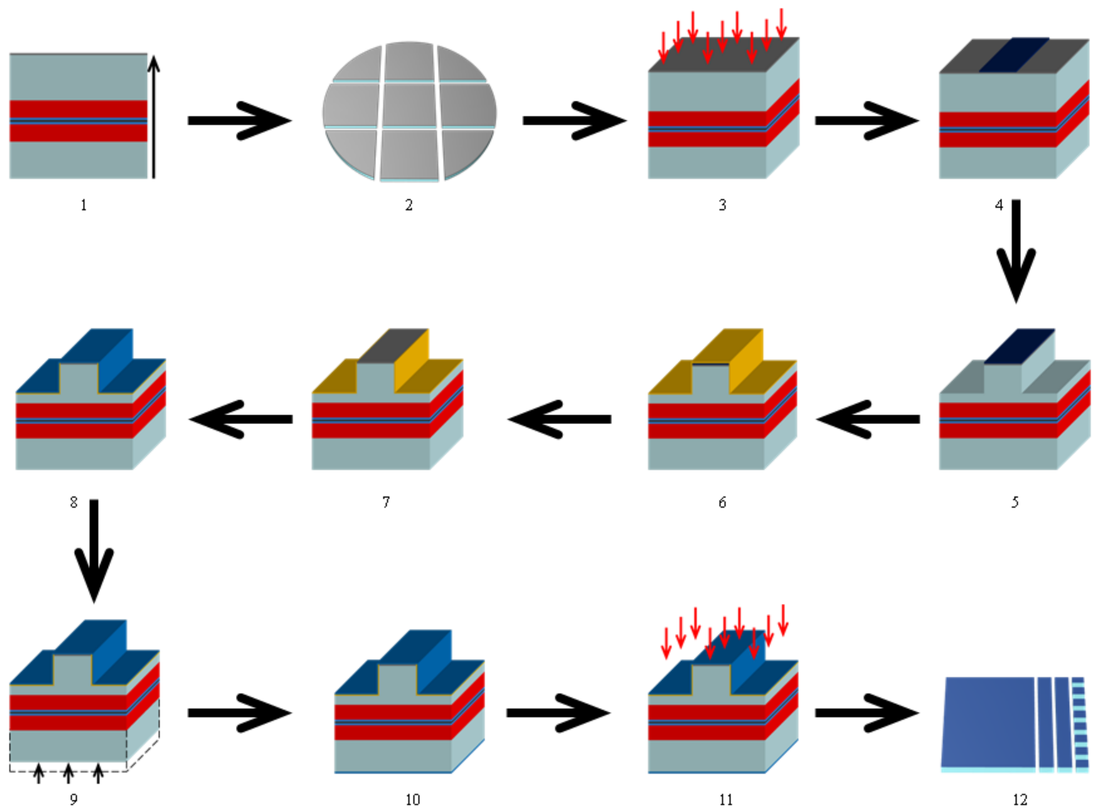

Section 1.2 “Motivation”. A reference was added in paragraph 4 page 2.

- “High-Power Diode Lasers: Fundamentals, Technology, Applications”, *R. Diehl, (Springer, Germany, 2000).*

Section 4.3 “Laser Design and Numerical Modelling”. A reference was added in paragraph 1 page 69.

- “Semiconductor Optoelectronics: Physics and Technology”, *J. Singh, (McGraw-Hill, Singapore, 1995).*

Captions to Fig. 4.9 was changed to include “Room temperature”.

- *Fig. 4.9 Room temperature photoluminescence spectra of thin-waveguide and broad-waveguide laser structures (p-doped InGaAs and InP selectively etched off).*

Captions to Fig. 5.9 was changed to include “over the range of 0-3000 mA”.

- *Fig. 5.9 Averaged measured maximum output power over the range of 0-3000 mA from different device length and different structures. (Lines are guide to the eye).*

Figure 6.7 was updated. The values of dL/dI changed to account for 1% injection current duty cycle.